# Study of Polymer Topology Effects on Cyclic Poly(ethylene glycol) and Pluronic surfactants in Solution and at Interfaces

*A Dissertation for the Degree of Doctor of Philosophy*

**Tomohisa Watanabe**

**Hokkaido University**

**March, 2025**

**Acknowledgements**

The research presented hereby was performed under the guidance of Associate Professor Takuya Yamamoto, Division of Applied Chemistry, Faculty of Engineering, Hokkaido University. I am truly grateful for his supervision and deeply respect his unending passion and devotion towards research, which inspired myself to pursue a career as an independent academic. I also would like to express my gratitude to Associate Professor Shin-ichiro Sato, Professor Toshifumi Satoh, Associate Professor Kenji Tajima, Associate Professor Takuya Isono and Assistant Professor Feng Li for their kind support and guidance throughout my PhD course. Furthermore, the present work was realized through collaboration with other inspirational researchers. For this, I deeply thank Associate Professor Daichi Ida (Kyoto University), Assistant Professor Akiyuki Ryoki (Kyoto University) and Dr. Hiroki Iwase (CROSS) for their crucial comments and advice in conducting a challenging research outside of my field, which consequently resulted in the expansion my expertise and the development of a wide range of research interests.

Regarding my day-to-day life at the laboratory, I am thankful to the past and present members of both the Laboratory of Chemistry of Molecular Assemblies and Polymer Chemistry Laboratory. Special mentions go to the following people; Ryohei Sato, Yubo Wang, Satoru Chimura, Atsuo Utagawa, Onyinyechukwu-Justina Chioke, Moka

Takashima, Xueming Su, Rika Kudo, Tomoko Ono, Yoko Kinoshita, Yumi Kosobe, Yuna Kinoshita, Yuto Okuma, Akira Takatsuka, Masato Yamasaki, Tsuyoshi Nakai, Katsuyuki Namai, Kenta Komura, Ayaka Otsuka, Bincy Akkoli Pottammal, Yuki Maruyama, Mayu Kakizaki, Yuki Tanaka, Sota Arima, Jo Tazuke, Makoto Hikichi, Kotaro Okawa, Weeranuch Lang, Tianle Gao, Chaehun Lee, Minami Ebe, Ryota Suzuki, Satoru Takagi, Hashim Binti Hamidah, Taiki Nishimura, Yamato Ebii and Chun-Yao (Kenny) Ke.

Finally, I'd like to express my utmost gratitude to my family and partner. Without your unwavering support, none of this would have been realized. Thank you all.

March, 2025

Tomohisa Watanabe

## CONTENTS

# *Chapter 1*

## General Introduction

## 1.1. Polymer topology

Polymeric materials can be defined as molecules with large molecular weights (*i.e. macromolecules*) that are made up by linking a number of smaller chemical units called monomers. The properties of polymers vastly differ from small molecules due to the inherent "freedom" in its structure and morphology, created by connecting monomers of diverse chemical structure, or by controlling the amount and the ways of connection.[1] Especially for the latter, development of precision chemistry and polymerization techniques have opened up pathways to create polymers of diverse architecture or "topology",[2] leading to unconventional control over their physical properties.[3, 4] Systematic classification of non-linear polymer topologies have been summarized by Tezuka et al,[5] where typical examples include star-shaped,[6] comb-like,[7] randomly-branched,[8] cyclic[9] and multicyclic architectures (Figure 1-1).[10]

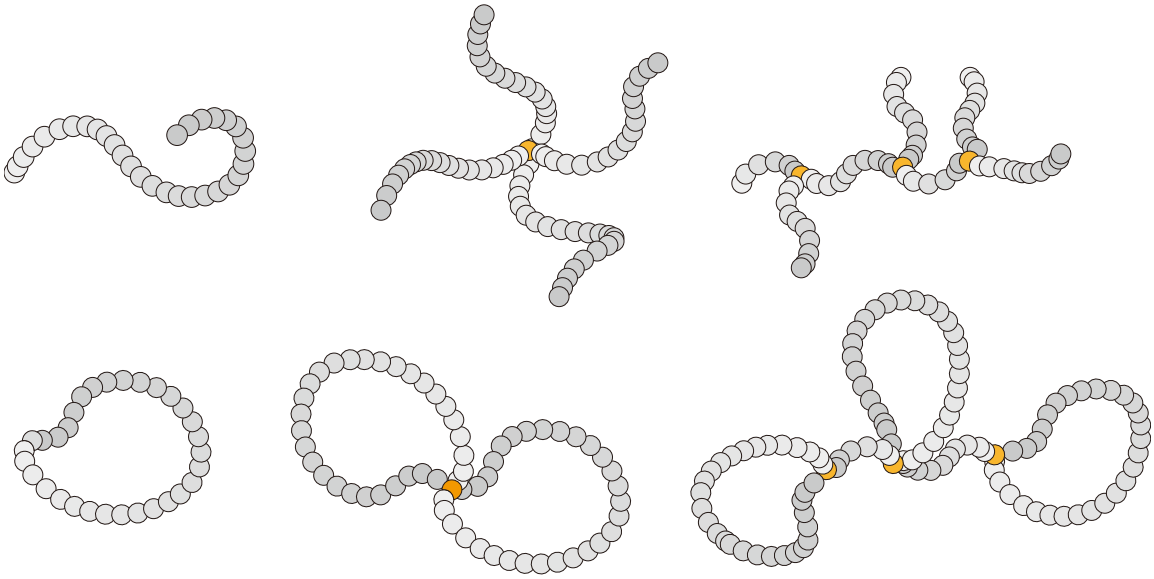

**Figure 1-1.** Examples of polymers of various architectures or topologies.

## 1.2. Cyclic polymers

Amongst the various topologies that have been realized for synthetic polymers to date, polymers that have a cyclic, or a ring -like architecture have especially gathered interest due to a number of unique properties that arise from lacking chain-ends. Before the first intentional synthesis of cyclic polymers, macromolecules that possessed a cyclic topology was discovered in nature, which laid the foundation for understanding the importance of cyclic architectures. In 1958, Jacob and Wollman hypothesized the existence of cyclic DNA elements,[11] a notion that was later confirmed in 1964 through electron microscopy of bacteriophage.[12] Circular DNA exhibits distinct advantages over linear DNA, such as enhanced chemical and thermal stability, making it a cornerstone of genetic stability in certain organisms. Cyclic peptides, another naturally occurring class of cyclic biomolecules, display remarkable stability against proteolytic degradation and thermal stress due to their unique topology. For instance, kalata B1, a cyclic peptide isolated from *Oldenlandia affinis*, was notable for its stability even in boiling water.[13] Similarly, cyclic lipids found in extremophiles such as archaea enable cellular stability under extreme temperatures and pH, underscoring the adaptive advantages of cyclic structures in nature.[14, 15]

The first synthetic cyclic polymers emerged as by-products of step-growth polymerization processes.[16, 17] It was not until the 1970s and 1980s that the development of targeted synthetic strategies enabled the systematic study of cyclic polymers. For instance, Rempp and colleagues successfully synthesized cyclic polystyrene (PS) using a bimolecular ring-closure technique involving an anionic polymerization of linear precursors followed by cyclization with a dihalogen coupling agent.[18] This breakthrough highlighted the potential of cyclic polymers for advanced materials research, despite challenges related to purity and scalability. Subsequently, a variety of effective synthetic methods have been developed to address these issues, with the two most popular and successful routes being ring-closure and ring-expansion strategies (Figure 1-2).[19] Ring-closure techniques hold advantages in that they are compatible with a variety of polymerization techniques and chemical backbones. However, they generally require highly dilute conditions, and are only suitable for cyclizing polymers of relatively low molecular weight.[20] On the other hand, ring-expansion techniques can produce cyclic polymers of much larger molecular weight of high purity.[21] Nevertheless, this strategy also possess drawbacks, such as challenges in their control over molecular weight and distributions, along with the limited applicability of polymerizations.[22]

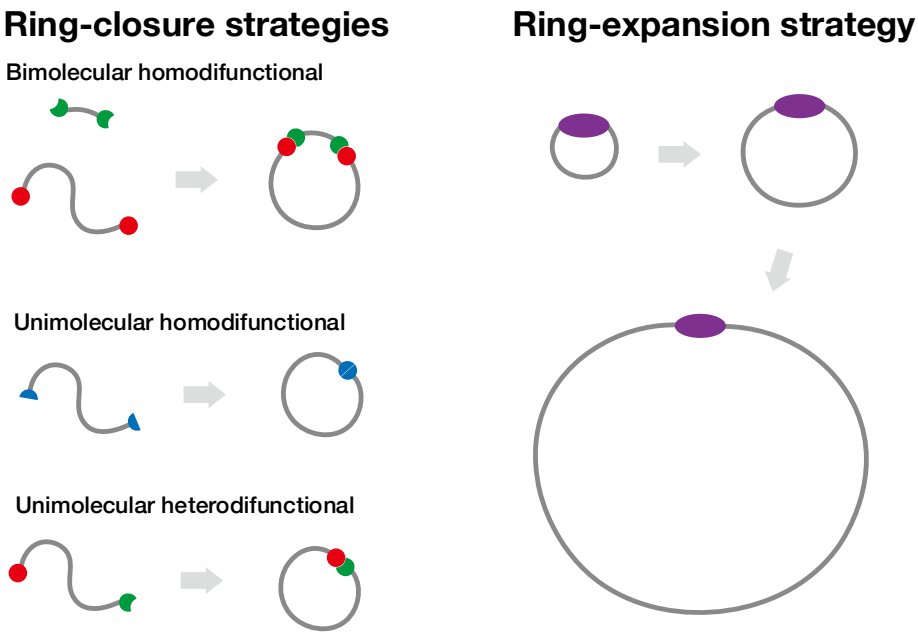


**Figure 1-2.** Major synthetic routes to produce cyclic polymers.

The motivation towards extensive research on cyclic polymers is primarily due to the fact that they exhibit distinctive physical properties from their linear counterparts. These properties stem from their unique topology, which eliminates chain ends and imposes structural constraints. One of the most notable properties is their reduced hydrodynamic volume compared to linear polymers of equivalent molecular weight.[23] Furthermore, it has been highlighted that cyclic polymers demonstrate increased glass transition temperatures ($T_g$) relative to linear analogs, attributed to the constrained molecular motion within the cyclic architecture.[24, 25] Crystallization studies revealed that cyclic polymers can form highly ordered domains in shorter time, due to reduced entanglement which allowed for a faster attainment of equilibrium state.[26] As such, the crystallized films of cyclic polycaprolactones were found to display enhanced stabilities, indicating the potential applications of cyclic polymers to improve the robustness of materials without altering their monomer chemical structure. In other studies, cyclic polymers exhibited unique rheological behavior; their dynamics are dominated by an amoeba-like motion rather than the reptation mechanism seen in linear polymers, attributed to the absence of chain ends.[27] In the presence of linear counterparts, cyclic polymers have also been found to exhibit complex phenomena such as threading, which was confirmed by the observation of multimode diffusion of cyclices in matrixes of linear

polymers.[28] The effect of threading was found to further have a dramatic effect on the intrinsic viscosities of polymers, where while cyclic polymers on their own displayed significantly reduced values (e.g. intrinsic viscosities ratio of 0.57–0.63 for cyclic polystyrenes compared to their linear counterparts),[29] mixtures of linear and cyclic polymers, have shown prominent increase, even when compared to values for pure linear polymers.[30]

Recently, the so-called topology effects of cyclic polymers have been demonstrated to be amplified in self-assembled structures, such as microphase separation in the bulk state and in micellar solution.[31, 32] For instance, cyclic diblock copolymers of polystyrene and polyethylene oxides have been found to achieve smaller domain spacing compared to their corresponding linear block copolymers, where a significant decrease was observed from 25 nm to 20 nm for cyclices.[33] The significance of using cyclic block copolymers was justified when the decreased domain size was unable to attain by using linear block copolymers with shortened chain length, due to insufficient driving force for phase separation. In solution, block copolymers spontaneously self-assemble to produce "micelles", a molecular aggregate that forms a colloidally stable structure by the partitioning of a solvophobic segment in the interior of the micelle, while the solvophilic segment faces outwards into solution.[34, 35] Similar to the case of microphase separation,

micelles formed by cyclic block copolymers were found to have reduced dimensions compared to their linear counterparts. For example, Grayson *et al* found the diameters of PEO–PCL block copolymer micelles having a cyclic topology to shrink to 15 nm, from 27 nm for micelles formed from their linear counterparts.[36] More interestingly, the stabilities of block copolymer micelles were found to be significantly improved through the cyclic topology. Therein, Tezuka and Yamamoto *et al* compared micelle stability against temperature changes using linear triblock copolymer, poly(butyl acrylate) (PBA)-PEO-PBA and their cyclized diblock copolymer (cyclic PBA-PEO).[37] Due to the pseudo-cyclic conformation that was imposed upon the linear block copolymers upon the formation of micelles, the dimensions and critical concentrations of micelles were found to be similar to that of cyclic species. However, a substantial increase in could point temperature of 50 ºC was observed for cyclic polymers, attributed to the elimination of inter-micelle agglomeration that was caused by the bridging of micelles, when linear polymers were used. Similar systems were shown to display enhanced stability against salting-out conditions, which were further demonstrated to be tunable by varying the mixtures of linear and cyclic species.[38] The drastic enhancement of properties and this facile tunability of functions through control over topology holds implications for their use in biomedical applications, such as micelle-based drug delivery systems.[39, 40] More

recently, Whitfield et al demonstrated an unique formation of stable hierarchical structures for cyclic polymers that were not attained for their linear counterparts.[41] In their work, despite linear analogues of poly(2-hydroxyethyl methacrylate) only producing gel-like precipitates, cyclices were found to form worm-like structures that was further employed to produce worm-like assemblies and higher-ordered networks of brush polymers, hinting towards the use of cyclic topology to pre-organize macromolecules to produce further complex structures.

## 1.3. Interfaces

Interfaces, defined as the boundaries between different phases or materials, exhibit unique physical, chemical, and thermodynamic properties that significantly differ from those of the bulk phase, where matter exists homogeneously in a single state. These distinct characteristics make interfaces essential in various scientific and technological contexts.[42, 43] Interfaces have several distinguishing features. First, they often display gradients in density, composition, and molecular orientation that are absent in the bulk phase. For example, the liquid-vapor interface shows a gradual transition in density as liquid transforms into vapor.[44] Molecules at interfaces experience asymmetric forces because they lack neighboring molecules on one side, leading to phenomena such as surface tension.[45, 46] Unlike the three-dimensional nature of bulk phases, interfaces are quasi-two-dimensional, which results in unique mechanical and optical properties. Additionally, interfaces are highly dynamic regions where processes such as adsorption, catalysis, and diffusion occur more readily due to reduced dimensional constraints.[47]

Interfaces are critical in many applications across different fields (Figure 1-3).[48] In material science, they determine the properties of composites, coatings, and thin films.[49] For instance, the mechanical strength of metals is significantly influenced by the behavior of grain boundaries, which can be understood as internal interfaces.[50] In

catalysis, reactions often occur at the interface of a heterogeneous catalyst and the reactants, where the unique environment enhances reactivity and selectivity.[47] Biological membranes, which are lipid bilayer interfaces, are essential for cellular transport and communication.[51] Interfaces are particularly important in nanotechnology due to the high surface-to-volume ratio at the nanoscale, which amplifies the effects typically observed at interfaces. This dominance of interface-related phenomena enables a wide range of applications. For example, the surface properties of nanoparticles, which are defined as a broad spectrum of materials that have at least one dimension in the range of 1–100 nm,[52] are critical in drug delivery,[53] imaging,[54] and catalysis.[55] Interface-driven forces also govern the self-organization and self-assembly (often used in interchangeable context) of nanostructures, such as micelles[56] and block copolymers.[35, 57] In energy systems, interfaces in thin-film solar cells,[58, 59] batteries,[60] and supercapacitors[61] significantly impact charge transport and energy conversion efficiency.

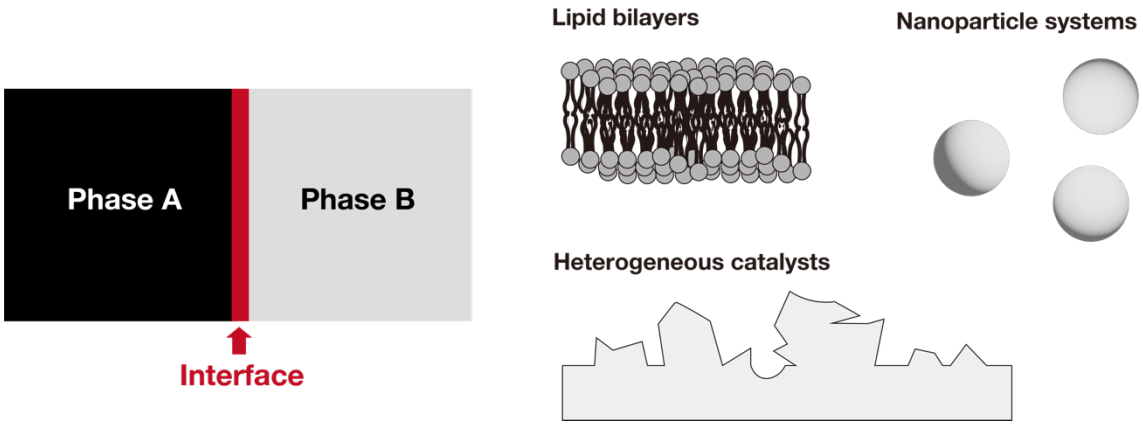


**Figure 1-3**. Schematic illustration of an interface (left) and examples of systems where interfaces are of importance (right)

## 1.4. Polymers at interfaces

As mentioned in section 1.3., interfaces occur in every system as long as there are two or more phases present. Control over interfaces are pivotal in determining properties and functions of materials. To this end, polymeric materials are often utilized to tune the properties of interfaces to the desired applications, where their versatile chemical and physical properties such as molecular structure and strong adsorption dynamics, make them effective surface modifiers.[62]

In regard to the various modes of polymers present at interfaces, physical adsorption is a key mechanism where polymers spontaneously adhere to surfaces, forming structures with trains (adsorbed segments), loops, and tails.[62] While the individual strength of physical adsorption itself may not large (in comparison with the energy of forming covalent bonds), the vast amount of interacting sites (monomers) result in a significantly higher adsorption energy of a polymer compared to that to small molecules, ensuring more robust and longer-lasting interfacial modifications.[63] Terminal grafting, another prominent approach, involves covalently attaching polymer chains to surfaces.[64] Polymer grafting can be further classified into "grafting-from," and "grafting-to," methods. While the former utilizes active species existing on the polymer surfaces to initiate the polymerization of monomers from the surface toward the bulk phase, the latter covalently couples presynthesized polymer chains that possess terminal/side chain

reactive groups to the surface.[65] In addition to the chemical structure of adsorbed polymers, variations in chain length and density, plays a crucial role in tuning their interfacial properties. For instance, dense grafted polymers, provide enhanced steric stabilization and significantly reduce friction, thus making them invaluable in applications like superlubrication,[66] antifouling[67, 68] and biocompatible coatings.[69]

Polymers grafted onto interfaces are often called “polymer brushes”, and has become an indispensable part of nanotechnology. In systems that exhibit a large amount of nanometer-scale interfaces, such as nanoparticle dispersions, the importance of tuning of interfacial properties become increasingly larger. Nanoparticles often suffer from limited colloidal stability, and require appropriate modification of the surface. Endowment of colloidal stability through the effects of steric hindrance that are provided from polymer brushes are a practical method to achieve this.[70] For instance, gold nanoparticles have been readily modified with water soluble poly(ethylene glycol) chains through their terminal attachment via an Au–S bond formation.[71] In fact, surface modifications of various interfaces using PEG, i.e. PEGylation, are considered a *golden standard* in achieving hydrophilicity, biocompatibility,[72] resistance to protein adsorption,[73] stealth properties,[74] and other various biologically relevant properties.[75-78]

Until recently, the topologies of polymer brushes have been limited to linear polymers. However, in 2016, the group of Benetti et al, reported the effect of cyclic polymer brushes on the surface of titanium oxide surfaces.[79] In this seminal work, cyclic poly(2-ethyl-2-oxazoline) (PEOXA) adsorbates with $M_w$ 5 and 10 kDa was found to result in almost twice the grafting density due to their reduced dimensions in solution, when compared with their corresponding linear polymer brushes. Furthermore, the increased density was demonstrated to result in a improved resistance towards protein adsorptions, in addition to an emergence of a super-lubricating character upon shearing against each other, arising from the lack of chain entanglements of cyclic polymer brushes. This was further applied for the colloidal stabilization of $Fe_3O_4$ nanoparticles, thereby achieving redispersion of thermally aggregated particles and prevented non-specific interaction with proteins, both of which could not be realized when using their linear counterparts.[80] This paved the way for several studies employing cyclic polymer brushes at interfaces to improve their respective properties such as stability in organic solvents.[81-83]

In 2020, our own group reported colloidal stabilization of gold nanoparticles using cyclic PEG (Figure 1-4).[84] However, the mode of interaction between cyclic PEG and gold nanoparticles were through covalent bond formation, but rather, through physical

interaction, i.e., physisorption of the polymer and the nanoparticle surface. Interestingly, the stabilizing effect of cyclic PEG achieved colloidal dispersion of gold nanoparticles under various environments, such as freezing, lyophilization, PBS buffer solutions, and in heated solutions. Especially under heating conditions, c-PEGs were found to offer stability which surpassed that of conventional PEGylation ligands, namely linear PEG with thiol terminal moieties.[84] The non-specific adsorption mechanism which was expected for cyclic PEG allowed for their subsequent application towards stabilization of silver nanoparticles,[85] further hinting towards a completely novel mode of PEGylation which offers the establishment of both versatility and high performance. However, the present understanding of this unique physisorption of cyclic PEG, along with key information on their complex structure with gold nanoparticles, is completely lacking and requires vigorous investigation in anticipation of their eventual application.

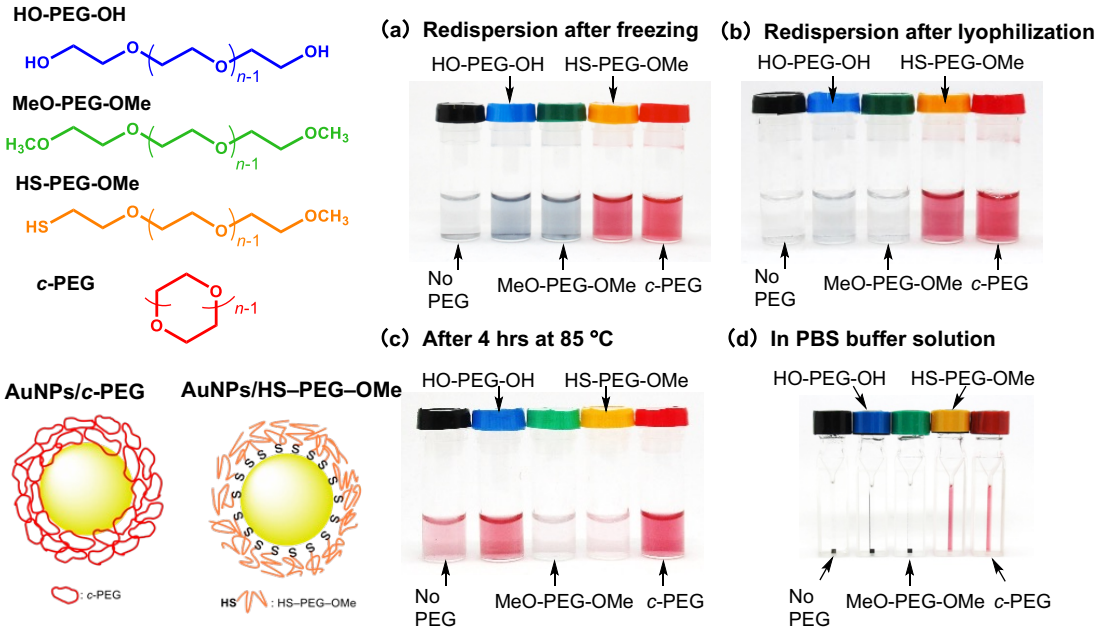


**Figure 1-4.** PEGylation of gold nanoparticles through the physisorption of cyclic poly(ethylene glycol) (*c*-PEG), compared with other non-adsorbing linear PEGs (HO–PEG–OH, MeO–PEG–OMe) and chemisorbed thiol PEG (HS–PEG–OMe). (Adopted from ref. 84.)

## 1.5. Objective and the outline of this dissertation

Having discussed the above aspects, the aim of this study is to discover novel properties of cyclic polymers, especially at various interfaces, which is expected to amplify the topology effects of cyclic polymers, in anticipation for their potential applications in material design. Taking in mind the already generally well-developed understanding of hydrophobic cyclic polymers along with our previous report on the unique physisorption properties of cyclic PEG onto nanoparticles, investigation on the

effect of cyclic topology was carried out for homopolymers and block copolymers that possess PEG backbones, and their physical properties in aqueous media.

In chapter two, the interfacial adsorption properties of cyclic and linear polymers for PEG and triblock copolymers comprised of PEG and poly(propylene glycol) (PPG) blocks, commercially available as Pluronic surfactants, were compared at the air–water interface through surface tension measurements. An evident increase in interfacial activity was observed for cyclic polymers, with differing impact depending on the molecular weight, block composition, and block sequence. The results were further quantitatively discussed through the calculation of surface occupational area of a single molecule ($A$), where cyclices were found to occupy reduced $A$. Consequently, this led to a denser adsorbed layer at the interface, resulting in their enhanced surface activity.

In chapter three, the topology effects of cyclic Pluronics were further investigated on their self-assembly properties. Micellar systems can be regarded to possess multiple interfaces of large area, at the boundary of hydrophobic/hydrophilic blocks and hydrophilic blocks/solvent. In light of previous effects of topology found on the stability of PEO–PBA flower-like micelles, systematic investigations on various linear and cyclic Pluronic surfactants were carried out on their critical micellization temperature and at their phase separation temepratures. A reduced critical micellization temperature, along

with block sequent-dependent change in phase separation temperature was observed for cyclices, revealing a complex relationship of the block composition of the linear polymers to affect the direction and magnitude of the effects of cyclic topology on their aggregation in solution. Thermodynamic analyses of micellization phenomena was further conducted to discuss the consequence of topology, where cyclization was indicated to effectively shield the hydrophobic blocks from contact with the surrounding water, thus resulting in an reduced enthalpy of micellization. The effects of cyclization on the phase separation temperatures, on the other hand, proved to be more complex, especially between block copolymers and homopolymers. While the restriction of chain mobility at the micellar corona induced through the formation of loops, was suggested to decrease micellar stability of cyclic Pluronic surfactants, cyclic PEG homopolymers were found to display increased phase separation temperatures, which were attributed to their topological excluded-volume effect, resulting in an apparent resistance towards chain collapse and subsequent desolvation.

In chapter four, a structural study of cyclic PEG and cyclic PEG adsorbed gold nanoparticle complexes were investigated using small-angle scattering methods. First, the conformations and chain dimensions of cyclic PEG in dilute solution were elucidated through small-angle X-ray scattering (SAXS), in comparison with their corresponding

linear counterparts. The molecular weight dependency, along with solvent dependency on the dimensions and conformations of cyclic PEG are discussed in relation to the topological excluded-volume effect. Next, the complex structures of cyclic PEG adsorbed gold nanoparticles were investigated using small-angle neutron scattering (SANS). In the aim to isolate scattering from purely the cyclic PEG–gold nanoparticle complexes, the excess unadsorbed cyclic PEG in the system was removed via subsequent ultrafiltration and solvent exchange. This preparation method, along with the distinct interaction of neutron beams with various elements allowed for the simultaneous observation of the gold core and the adsorbed cyclic PEG corona *in situ* for the first time.

Furthermore, a contrast-matching technique using an appropriate mixture of $D_2O$ and $H_2O$ to match the scattering contrast of gold was employed, realizing the isolation of scattering signals of the adsorbed cyclic PEG corona. A model-dependent and independent fitting was conducted, through which a quantitative evaluation of the amount of adsorbed cyclic PEG and the adsorbed layer thickness was achieved. Comparison with gold nanoparticles complexed with linear thiol-PEG molecules, revealed the generally sparce, thin surface adsorption of cyclic PEGs, which is surprising based on the high stabilizing effect they impart on gold nanoparticles. However, this structural elucidation

of complexes can be taken as a significant step towards the establishment and implementation of a novel, efficient PEGylation method through the use of cyclic PEG.

In the final section, chapter five, a general conclusion is made on the topology effect that was observed for cyclic polymers at various interfaces. At the air–water interface, a unique densification of cyclic amphiphiles was realized, due to the confinement of polymer chains induced by its topology. At critical micellization conditions, the cyclic topology was found to effectively shield the hydrophobic blocks, while the formation of loops at micellar–solvent interfaces destabilized the system at critical points of phase separation. Finally, the structural characteristics of cyclic PEG in solution and their surface adsorbed gold nanoparticle complexes were elucidated in solution using SAXS and SANS, which revealed the distinct characteristics of cyclic topology at the nanoparticle surface. In contrast to the significant progresses in the precise synthetic technologies of cyclic polymers, the fundamental understanding of their properties, especially in non-conventional and complex environments (such as in water, confinements and at interfaces, etc.) is still in its infancy. This is partly because of the lack of clear goals, and no guarantee of the discovery of a favorable property through their investigation. However, The present studies have shown the cyclic topology to clearly have consequences on various physical properties exhibited by amphiphilic cyclic

polymers at various interfaces, which opens up pathways to exploit these properties for their potential applications and implementation in the development of novel, functional materials.

## 1.6. References

(1) Sato, T.; Kanaya, T.; Ito, K.; Watanabe, H.; Tanaka, K.; Shimomura, T.; Inoue, T. *Structures and physical properties of polymers*; Kodansha, 2013.

(2) Polymeropoulos, G.; Zapsas, G.; Ntetsikas, K.; Bilalis, P.; Gnanou, Y.; Hadjichristidis, N. 50th Anniversary Perspective: Polymers with Complex Architectures. *Macromolecules* **2017**, *50* (4), 1253-1290. DOI: 10.1021/acs.macromol.6b02569.

(3) Tezuka, Y. Topological polymer chemistry: Classification and construction of nonlinear polymer architectures. *Macromolecular Symposia* **2003**, *192*, 217-226.

(4) *Topological Polymer Chemistry: Progress of Cyclic Polymers in Syntheses, Properties and Functions*; Tezuka Y. Ed.,World Scientific, 2013.

(5) Tezuka, Y.; Oike, H. Topological polymer chemistry. *Progress in Polymer Science* **2002**, *27* (6), 1069-1122. DOI: 10.1016/s0079-6700(02)00009-6.

(6) Hadjichristidis, N.; Iatrou, H.; Pitsikalis, M.; Mays, J. Macromolecular architectures by living and controlled/living polymerizations. *Prog. Polym. Sci.* **2006**, *31* (12), 1068-1132. DOI: 10.1016/j.progpolymsci.2006.07.002.

(7) Shi, H.; Zhao, Y.; Dong, X.; Zhou, Y.; Wang, D. Frustrated crystallisation and hierarchical self-assembly behaviour of comb-like polymers. *Chem. Soc. Rev.* **2013**, *42* (5), 2075-2099. DOI: 10.1039/c2cs35350d.

(8) Konkolewicz, D.; Gray-Weale, A.; Perrier, S. The structure of randomly branched polymers synthesized by living radical methods. *Polm. Chem.* **2010**, *1* (7), 1067-1077. DOI: 10.1039/c0py00064g.

(9) Semlyen, J. A. Cyclic Polymers. 2nd ed.; Kluwer Academic Publishers: New York, 2002.

(10) Tezuka, Y. Topological Polymer Chemistry Designing Complex Macromolecular Graph Constructions. *Acc. Chem. Res.* **2017**, *50* (11), 2661-2672. DOI: 10.1021/acs.accounts.7b00338.

(11) Jacob, F.; Wollman, E. L. Genetic and physical determinations of chromosomal segments in Escherichia coli. *Symp. Soc. Exp. Biol.* **1958**, *12*, 75–92.

(12) Freifelder, D.; Sinsheimer, R.; Kleinschmidt, A. Electron Microscopy of Single-stranded DNA - Circularity of DNA of Bacteriophage Phix174. *Science* **1964**, *146* (364), 254–255.

(13) Saether, O.; Craik, D.; Campbell, I.; Sletten, K.; Juul, J.; Norman, D. Elucidation of the Primary and 3-dimensional Structure of the Uterotonic Polypeptide Kalata B1. *Biochemistry* **1995**, *34* (13), 4147-4158.

(14) Sprott, G. Structures of Archaebacterial Membrane-lipids. *J. Bioenerg. Biomembr.* **1992**, *24* (6), 555-566.

(15) Sprott, G.; Meloche, M.; Richards, J. Proportions of Diether, Macrocyclic Diether, and Tetraether Lipids in Methanococcus-jannaschii Grown at Different Temperatures. *J. Bacter.* **1991**, *173* (12), 3907-3910.

(16) Carothers, W.; Arvin, J.; Dorough, G. Studies on polymerization and ring formation. V. Glycol esters of oxalic acid. *J. Amer. Chem. Soc.* **1930**, *52*, 3292-3300.

(17) Carothers, W.; Van Natta, F. Studies on polymerization and ring formation. III. Glycol esters of carbonic acid. *J. Amer. Chem. Soc.* **1930**, *52*, 314-326.

(18) Hild, G.; Kohler, A.; Rempp, P. Synthesis of Ring-shaped Macromolecules. *Eur. Polym. J.* **1980**, *16* (6), 525-527.

(19) Lienard, R.; De Winter, J.; Coulembier, O. Cyclic polymers: Advances in their synthesis, properties, and biomedical applications. *J. Poly. Sci.* **2020**, *58* (11), 1481-1502. DOI: 10.1002/pol.20200236.

(20) Haque, F. M.; Grayson, S. M. The synthesis, properties and potential applications of cyclic polymers. *Nat. Chem.* **2020**, 433-444. DOI: 10.1038/s41557-020-0440-5.

(21) Bielawski, C. W.; Benitez, D.; Grubbs, R. H. An "endless" route to cyclic polymers. *Science* **2002**, *297* (5589), 2041-2044.

(22) Brown, H.; Waymouth, R. Zwitterionic Ring-Opening Polymerization for the Synthesis of High Molecular Weight Cyclic Polymers. *Acc. Chem. Res.* **2013**, *46* (11), 2585-2596. DOI: 10.1021/ar400072z.

(23) Kricheldorf, H. R. Cyclic Polymers: Synthetic Strategies and Physical Properties. *J. Polym. Sci., Part A: Polym. Chem.* **2010**, *48* (2), 251-284. DOI: 10.1002/pola.23755.

(24) Xu, X.; Zhou, N. C.; Zhu, J. A.; Tu, Y. F.; Zhang, Z. B.; Cheng, Z. P.; Zhu, X. L. The First Example of Main-Chain Cyclic Azobenzene Polymers. *Macromol. Rapid Commun.* **2010**, *31* (20), 1791-1797. DOI: 10.1002/marc.201000218.

(25) Kammiyada, H.; Ouchi, M.; Sawamoto, M. A Study on Physical Properties of Cyclic Poly(vinyl ether)s Synthesized via Ring-Expansion Cationic Polymerization. *Macromolecules* **2017**, *50* (3), 841-848, Article. DOI: 10.1021/acs.macromol.6b02704.

(26) Kelly, G.; Haque, F.; Grayson, S.; Albert, J. Suppression of Melt-Induced Dewetting in Cyclic Poly(ε-caprolactone) Thin Films. *Macromolecules* **2017**, *50* (24), 9852-9856. DOI: 10.1021/acs.macromol.7b02200.

(27) McLeish, T. Polymers without beginning or end. *Science* **2002**, *297* (5589), 2005-2006.

(28) Habuchi, S.; Satoh, N.; Yamamoto, T.; Tezuka, Y.; Vacha, M. Multimode Diffusion of Ring Polymer Molecules Revealed by a Single-Molecule Study. *Angew. Chem., Int. Ed.* **2010**, *49* (8), 1418-1421. DOI: 10.1002/anie.200904394.

(29) Jeong, Y.; Jin, Y.; Chang, T.; Uhlik, F.; Roovers, J. Intrinsic Viscosity of Cyclic Polystyrene. *Macromolecules* **2017**, *50* (19), 7770-7776. DOI: 10.1021/acs.macromol.7b01511.

(30) Roovers, J. Viscoelastic Properties of Polybutadiene Rings. *Macromolecules* **1988**, *21* (5), 1517-1521, Article. DOI: 10.1021/ma00183a049.

(31) Yamamoto, T.; Tezuka, Y. Cyclic polymers revealing topology effects upon self-assemblies, dynamics and responses. *Soft Matter* **2015**, *11* (38), 7458-7468. DOI: 10.1039/c5sm01557j.

(32) Yamamoto, T. Topology effects of cyclic polymers: Controlling the topology for innovative functionalities. *React. Funct. Polym.* **2018**, *132*, 43-50. DOI: 10.1016/j.reactfunctpolym.2018.08.021.

(33) Poelma, J. E.; Ono, K.; Miyajima, D.; Aida, T.; Satoh, K.; Hawker, C. J. Cyclic block copolymers for controlling feature sizes in block copolymer lithography. **2012**, *6*, 10845-10854.

(34) Karayianni, M.; Pispas, S. Block copolymer solution self-assembly: Recent advances, emerging trends, and applications. *J. Polym. Sci.* **2021**, *59* (17), 1874-1898. DOI: 10.1002/pol.20210430.

(35) Mai, Y.; Eisenberg, A. Self-assembly of block copolymers. *Chem. Soc. Rev.* **2012**, *41* (18), 5969-5985. DOI: 10.1039/c2cs35115c.

(36) Zhang, B.; Zhang, H.; Li, Y.; Hoskins, J. N.; Grayson, S. M. Exploring the Effect of Amphiphilic Polymer Architecture: Synthesis, Characterization, and Self-Assembly of Both Cyclic and Linear Poly(ethylene gylcol)-b-polycaprolactone. *ACS Macro Lett.* **2013**, *2* (10), 845-848. DOI: 10.1021/mz4003936.

(37) Honda, S.; Yamamoto, T.; Tezuka, Y. Topology-directed control on thermal stability: Micelles formed from linear and cyclized amphiphilic block copolymers. *J. Am. Chem. Soc.* **2010**, *132* (30), 10251-10253. DOI: 10.1021/ja104691j.

(38) Honda, S.; Yamamoto, T.; Tezuka, Y. Tuneable enhancement of the salt and thermal stability of polymeric micelles by cyclized amphiphiles. *Nat. Commun.* **2013**, *4*, 1574. DOI: 10.1038/ncomms2585.

(39) Movassaghian, S.; Merkel, O.; Torchilin, V. Applications of polymer micelles for imaging and drug delivery. *Wiley Interdiscip. Rev.: Nanomed. Nanobiotechnology* **2015**, *7* (5), 691-707. DOI: 10.1002/wnan.1332.

(40) Tyrrell, Z.; Shen, Y.; Radosz, M. Fabrication of micellar nanoparticles for drug delivery through the self-assembly of block copolymers. *Prog. Polym. Sci.* **2010**, *35* (9), 1128-1143. DOI: 10.1016/j.progpolymsci.2010.06.003.

(41) Chen, C.; Singh, M.; Wunderlich, K.; Harvey, S.; Whitfield, C.; Zhou, Z.; Wagner, M.; Landfester, K.; Lieberwirth, I.; Fytas, G.; et al. Polymer cyclization for the emergence of hierarchical nanostructures. *Nat. Commun.* **2021**, *12* (1). DOI: 10.1038/s41467-021-24222-5.

(42) Israelachvili, J. N. *Intermolecular and surface forces third edition*; Elsevier, 2011. DOI: 10.1016/C2009-0-21560-1

(43) Adamson, A. W.; Gust, A. P. *Physical Chemistry of Surfaces 6th edition*; John Wiley & Sons, 1997.

(44) Alsnielsen, J. The Liquid Vapor Interface. *Z. Phys. B Con. Mat.* **1985**, *61* (4), 411-414.

(45) Navascues, G. Liquid Surfaces - Theory of Surface-tension. *Rep. Prog. Phys.* **1979**, *42* (7), 1131.

(46) Fathi-Azarbayjani, A.; Jouyban, A.; Chan, S. Impact of Surface Tension in Pharmaceutical Sciences. *J. Pharm. Pham. Sci.* **2009**, *12* (2), 218-228.

(47) Gao, W.; Hood, Z.; Chi, M. Interfaces in Heterogeneous Catalysts: Advancing Mechanistic Understanding through Atomic-Scale Measurements. *Acc. Chem. Res.* **2017**, *50* (4), 787-795. DOI: 10.1021/acs.accounts.6b00596.

(48) Kumar, G.; Rego, R.; Rao, H.; Nadar, N.; Kabiri, S.; Dilipkumar, P.; Kurkuri, M. Understanding the interfacial science of nature-inspired materials for versatile applications. *Surf. Interfaces* **2024**, *47*. DOI: 10.1016/j.surfin.2024.104181.

(49) *Interface Science and Composites*, Park S.-J.; Seo, M.-K. ed., Elsevier, 2011.

(50) Shaat, M.; Fathy, A.; Wagih, A. Correlation between grain boundary evolution and mechanical properties of ultrafine-grained metals. *Mec. Mat.* **2020**, *143*. DOI: 10.1016/j.mechmat.2020.103321.

(51) Redondo-Morata, L.; Losada-Pérez, P.; Giannotti, M. Lipid bilayers: Phase behavior and nanomechanics. *Curr. Top Membr.*, **2020**, *86*, 1-55.

(52) Baig, N.; Kammakakam, I.; Falath, W. Nanomaterials: a review of synthesis methods, properties, recent progress, and challenges. *Mater. Adv.* **2021**, *2* (6), 1821-1871. DOI: 10.1039/d0ma00807a.

(53) Mitchell, M. J.; Billingsley, M. M.; Haley, R. M.; Wechsler, M. E.; Peppas, N. A.; Langer, R. Engineering precision nanoparticles for drug delivery. *Nat. Rev. Drug Discov.* **2021**, *20* (2), 101-124. DOI: 10.1038/s41573-020-0090-8.

(54) Harish, V.; Tewari, D.; Gaur, M.; Yadav, A.; Swaroop, S.; Bechelany, M.; Barhoum, A. Review on Nanoparticles and Nanostructured Materials: Bioimaging, Biosensing, Drug Delivery, Tissue Engineering, Antimicrobial, and Agro-Food Applications. *Nanomaterials* **2022**, *12* (3). DOI: 10.3390/nano12030457.

(55) Astruc, D. Introduction: Nanoparticles in Catalysis. *Chem. Rev.* **2020**, *120* (2), 461-463. DOI: 10.1021/acs.chemrev.8b00696.

(56) Svenson, S. Controlling surfactant self-assembly. *Curr. Opin. Colloid Interface Sci.* **2004**, *9* (3-4), 201-212. DOI: 10.1016/j.cocis.2004.06.008.

(57) Lu, Y.; Lin, J.; Wang, L.; Zhang, L.; Cai, C. Self-Assembly of Copolymer Micelles: Higher-Level Assembly for Constructing Hierarchical Structure. *Chem. Rev.* **2020**, *120* (9), 4111-4140. DOI: 10.1021/acs.chemrev.9b00774.

(58) Wolff, C.; Caprioglio, P.; Stolterfoht, M.; Neher, D. Nonradiative Recombination in Perovskite Solar Cells: The Role of Interfaces. *Adv. Mater.* **2019**, *31* (52). DOI: 10.1002/adma.201902762.

(59) Shao, S.; Loi, M. The Role of the Interfaces in Perovskite Solar Cells. *Adv. Mater. Int.* **2020**, *7* (1). DOI: 10.1002/admi.201901469.

(60) Xiao, Y.; Wang, Y.; Bo, S.; Kim, J.; Miara, L.; Ceder, G. Understanding interface stability in solid-state batteries. *Nat. Rev. Mater.* **2020**, *5* (2), 105-126. DOI: 10.1038/s41578-019-0157-5.

(61) Mahimai, B.; Li, E.; Pang, J.; Zhang, J.; Zhang, J. Interface engineering in conducting polymers-based supercapacitor. *J. Energy Storage* **2024**, *96*. DOI: 10.1016/j.est.2024.112598.

(62) Monteux, C. Adsorption of soluble polymers at liquid interfaces and in foams. *C. R. Phys.* **2014**, *15* (8-9), 775-785. DOI: 10.1016/j.crhy.2014.10.002.

(63) Hoeve, C. Theory of Polymer Adsorption at Interfaces. *J. Polym. Sci. C Polym. Symp.* **1971**, (34), 1-10.

(64) Kato, K.; Uchida, E.; Kang, E.; Uyama, Y.; Ikada, Y. Polymer surface with graft chains. *Prog. Polym. Sci.* **2003**, *28* (2), 209-259.

(65) Zhao, B.; Brittain, W. Polymer brushes: surface-immobilized macromolecules. *Prog. Polym. Sci.* **2000**, *25* (5), 677-710.

(66) Klein, J.; Kamiyama, Y.; Yoshizawa, H.; Israelachvili, J.; Fredrickson, G.; Pincus, P.; Fetters, L. Lubrication Forces Between Surfaces Bearing Polymer Brushes. Macromolecules 1993, 26 (21), 5552-5560. (67) Maan, A.; Hofman, A.; de Vos, W.;

Kamperman, M. Recent Developments and Practical Feasibility of Polymer-Based Antifouling Coatings. *Adv. Funct. Mater.* **2020**, *30* (32). DOI: 10.1002/adfm.202000936.

(68) Yang, W.; Neoh, K.; Kang, E.; Teo, S.; Rittschof, D. Polymer brush coatings for combating marine biofouling. *Prog. Polym. Sci.* **2014**, *39* (5), 1017-1042. DOI: 10.1016/j.progpolymsci.2014.02.002.

(69) Xu, Z.; Wang, S.; Li, Y.; Wang, M.; Shi, P.; Huang, X. Covalent Functionalization of Graphene Oxide with Biocompatible Poly(ethylene glycol) for Delivery of Paclitaxel. *ACS Appl. Mater. Interfaces* **2014**, *6* (19), 17268-17276. DOI: 10.1021/am505308f.

(70) Ling, D.; Hackett, M.; Hyeon, T. Surface ligands in synthesis, modification, assembly and biomedical applications of nanoparticles. *Nano Today* **2014**, *9* (4), 457-477. DOI: 10.1016/j.nantod.2014.06.005.

(71) Capek, I. Polymer decorated gold nanoparticles in nanomedicine conjugates. *Adv. Colloid Interface Sci.* **2017**, *249*, 386-399. DOI: 10.1016/j.cis.2017.01.007.

(72) Sanità, G.; Carrese, B.; Lamberti, A. Nanoparticle Surface Functionalization: How to Improve Biocompatibility and Cellular Internalization. *Front. mol. biosci.* **2020**, *7*. DOI: 10.3389/fmolb.2020.587012.

(73) Hucknall, A.; Rangarajan, S.; Chilkoti, A. In Pursuit of Zero: Polymer Brushes that Resist the Adsorption of Proteins. *Adv. Mater.* **2009**, *21* (23), 2441-2446. DOI: 10.1002/adma.200900383.

(74) Fam, S. Y.; Chee, C. F.; Yong, C. Y.; Ho, K. L.; Mariatulqabtiah, A. R.; Tan, W. S. Stealth Coating of Nanoparticles in Drug-Delivery Systems. *Nanomaterials* **2020**, *10* (4). DOI: 10.3390/nano10040787.

(75) Harris, J.; Chess, R. Effect of pegylation on pharmaceuticals. *Nat. Rev. Drug Discov.* **2003**, *2* (3), 214-221. DOI: 10.1038/nrd1033.

(76) Turecek, P.; Bossard, M.; Schoetens, F.; Ivens, I. PEGylation of Biopharmaceuticals: A Review of Chemistry and Nonclinical Safety Information of Approved Drugs. *J. Pharm. Sci.* **2016**, *105* (2), 460-475. DOI: 10.1016/j.xphs.2015.11.015.

(77) Jain, A.; Jain, S. PEGylation: An approach for drug delivery. A review. *Crit. Rev. Ther. Drug Carr. Syst.* **2008**, *25* (5), 403-447.

(78) Kolate, A.; Baradia, D.; Patil, S.; Vhora, I.; Kore, G.; Misra, A. PEG - A versatile conjugating ligand for drugs and drug delivery systems. *J. Control. Release* **2014**, *192*, 67-81. DOI: 10.1016/j.jconrel.2014.06.046.

(79) Morgese, G.; Trachsel, L.; Romio, M.; Divandari, M.; Ramakrishna, S. N.; Benetti, E. M. Topological Polymer Chemistry Enters Surface Science: Linear versus Cyclic

Polymer Brushes. *Angew. Chem., Int. Ed.* **2016**, *55* (50), 15583-15588. DOI: 10.1002/anie.201607309.

(80) Morgese, G.; Shaghasemi, B. S.; Causin, V.; Zenobi-Wong, M.; Ramakrishna, S. N.; Reimhult, E.; Benetti, E. M. Next-Generation Polymer Shells for Inorganic Nanoparticles are Highly Compact, Ultra-Dense, and Long-Lasting Cyclic Brushes. *Angew. Chem., Int. Ed.* **2017**, *56* (16), 4507-4511. DOI: 10.1002/anie.201700196.

(81) Romio, M.; Trachsel, L.; Morgese, G.; Ramakrishna, S. N.; Spencer, N. D.; Benetti, E. M. Topological Polymer Chemistry Enters Materials Science: Expanding the Applicability of Cyclic Polymers. *ACS Macro Lett.* **2020**, *9* (7), 1024-1033. DOI: 10.1021/acsmacrolett.0c00358.

(82) Aboudzadeh, M.; Iturrospe, A.; Arbe, A.; Grzelczak, M.; Barroso-Bujans, F. Cyclic Polyethylene Glycol as Nanoparticle Surface Ligand. *ACS Macro Lett.* **2020**, *9* (11), 1604-1610. DOI: 10.1021/acsmacrolett.0c00730.

(83) Aboudzadeh, M.; Kruse, J.; Iglesias, M.; Cangialosi, D.; Alegria, A.; Grzelczak, M.; Barroso-Bujans, F. Gold nanoparticles endowed with low-temperature colloidal stability by cyclic polyethylene glycol in ethanol. *Soft Matter* **2021**, *17* (33), 7792-7801. DOI: 10.1039/d1sm00720c.

(84) Wang, Y.; Quinsaat, J. E. Q.; Ono, T.; Maeki, M.; Tokeshi, M.; Isono, T.; Tajima, K.; Satoh, T.; Sato, S.; Miura, Y.; et al. Enhanced dispersion stability of gold nanoparticles by the physisorption of cyclic poly(ethylene glycol). *Nat. Commun.* **2020**, *11*, 6089.

(85) Oziri, O. J.; Wang, Y. B.; Watanabe, T.; Uno, S.; Maeki, M.; Tokeshi, M.; Isono, T.; Tajima, K.; Satoh, T.; Sato, S. I.; et al. PEGylation of silver nanoparticles by physisorption of cyclic poly(ethylene glycol) for enhanced dispersion stability, antimicrobial activity, and cytotoxicity. *Nanoscale Adv.* **2022**, *4* (2), 532-545. DOI: 10.1039/d1na00720c.

# *Chapter 2*

## Cyclization of PEG and Pluronic Surfactants and the Effect of the Topology on Their Activity at the Air–Water Interface

## 2.1. INTRODUCTION

With the development of synthetic technology, fabrication of precisely-defined polymers with non-linear architecture and examination of their physical and chemical properties from the point of view of the "topology" have been performed.[1, 2] In particular, cyclic polymers exhibit unique characteristics derived from the lack of chain ends, such as smaller viscosity, higher glass transition temperature, and smaller hydrodynamic volume than their linear counterparts with the same chemical composition and molecular weight.[3-6] As in the case of DNA[7] and archaea,[8] cyclic macromolecules also exist in nature, and exhibit unique functions based on the topology. The archaea acquire heat resistance because the cell membrane is partly composed of cyclic lipid molecules and can live in extreme environments such as submarine volcanoes and hot springs. Inspired by this, cyclic amphiphilic PBA–PEG block copolymers was synthesized by cyclization of linear amphiphilic PBA–PEG–PBA prepolymers, where PBA and PEG are poly(*n*-butyl acrylate) and poly(ethylene glycol), respectively, to compare the properties of linear and cyclic polymer micelles.[9, 10] The cloud point ($T_c$) measurement revealed that the cyclic polymer micelles were more resistant to heat and salinity. This is because the chain ends stimulates agglomeration due to the bridging between micelles with an increase in temperature, whereas dehydration was the main cause for the precipitation of the cyclic

polymer micelles.[11] In another example, a cyclized PEG homopolymer was found to have an extraordinary stabilizing effect on aqueous dispersions of gold nanoparticles compared to its linear counterpart.[12] Thus, the drastic improvement in the physical properties can be achieved by the topology without changing the chemical composition or molecular weight, suggesting that the topological approach is feasible in improving material properties.

In the meantime, amphiphilic block copolymers or surfactants having a very wide variety of chemical structures, compositions, and molecular weights have been developed and widely applied in both daily life and industrial scenes. For this reason, there is an important need for non-toxic surfactants capable of exhibiting higher functions with a small amount. For this purpose, triblock copolymers composed of PEG and poly(propylene glycol) (PPG) of various molecular weights and PEG/PPG ratios are typical nonionic surfactants, commercially available under the name of Pluronic.[13] The properties of Pluronic surfactants are expressed by the combination of a single alphabetical letter and numbers. The letter represents the physical appearance: "L" for liquid, "P" for paste, and "F" for flake. The letter "R" indicates a reverse type, which has a hydrophobic–hydrophilic–hydrophobic (BAB) sequence. The first one or two numbers multiplied by 300 represent the molecular weight of the PPG segments, and the last

number multiplied by 10 represents the weight fraction in percent of the PEG segments. For example, L35 represents a liquid having a PPG segment with a molecular weight of 950 g/mol and a PEG composition of 50 wt%. The surface activity of Pluronic surfactants and their molecular conformation at the air–water interface has been extensively studied, revealing the influences of the hydrophobic PPG block length, hydrophilic PEG block length, and total molecular weight.[14-18] Since Pluronic surfactants exhibit interfacial properties that vary greatly depending on the molecular weight and PEG/PPG ratio, optimal properties can be met to specific requirements in industrial applications. Importantly, Pluronic surfactants are biocompatible, and the higher the total molecular weight or the PEG composition the surfactants have, the lower the toxicity is.[13]

Despite the extensive uses of Pluronic surfactants, there is only one report on the effect of cyclization. Booth and coworkers succeeded in cyclizing an ABA type.[19] Thus, the synthesis of cyclic $PEG_{104}$–$PPG_{34}$ was achieved by acetalization of $PEG_{52}$–$PPG_{34}$–$PEG_{52}$ using $CH_2Cl_2$ and KOH. Although the critical micelle concentration (CMC) and particle size distribution of the micelles from the linear and cyclic surfactants were investigated, no drastic difference due to the cyclic topology was observed. Moreover, no interfacial activity has been studied. On the other hand, cyclization of a BAB-type Pluronic surfactant has never been reported up to date.

Here, the author focused on synthesis and investigation into the topology effects of a wide variety of cyclized Pluronic surfactants on their interfacial activity. Some of the most commonly used types of Pluronic surfactants such as L35, L64, P123, F68, 10R5, and 17R4 were cyclized by etherification or acetification along with a PEG homopolymer (Figure 2-1, Schemes 2-1 and 2-2). Methylation of the chain ends was also performed to investigate the effect of the hydroxy groups. The surface tension ($\gamma$) and molecular occupational area ($A$) were determined for the series of linear and cyclized surfactants. The cyclized surfactants showed significantly enhanced surface activity contrasting to its linear counterparts depending on the molecular weight and PEG/PPG ratio that could not be dismissed by merely the elimination of the chain-end hydroxy groups. Based on the results, effects of the topology on the surface activity properties of the surfactants are comprehensively deliberated.

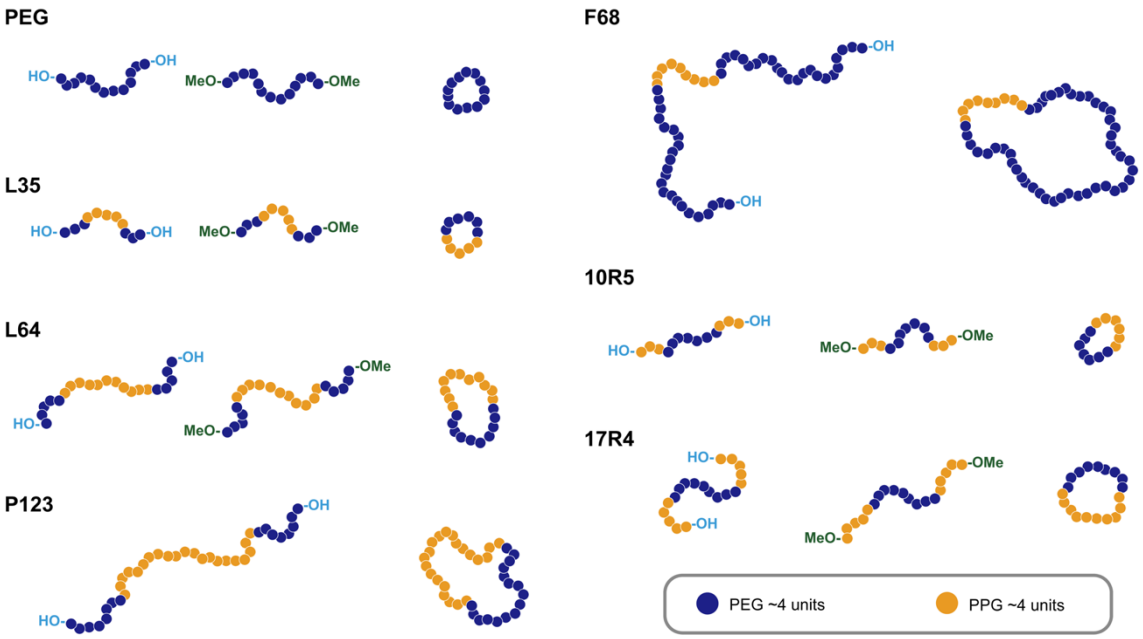


**Figure 2-1.** Schematic representations of PEG homopolymers, ABA-, and BAB-type Pluronic surfactants of various topology and chain-end groups. Approximate molecular weight and PEG/PPG ratios are represented in accordance with the SEC and NMR result.

**Scheme 2-1. Cyclization of (a) PEG homopolymer, (b) ABA-, and (c) BAB-type Pluronic Surfactants.**

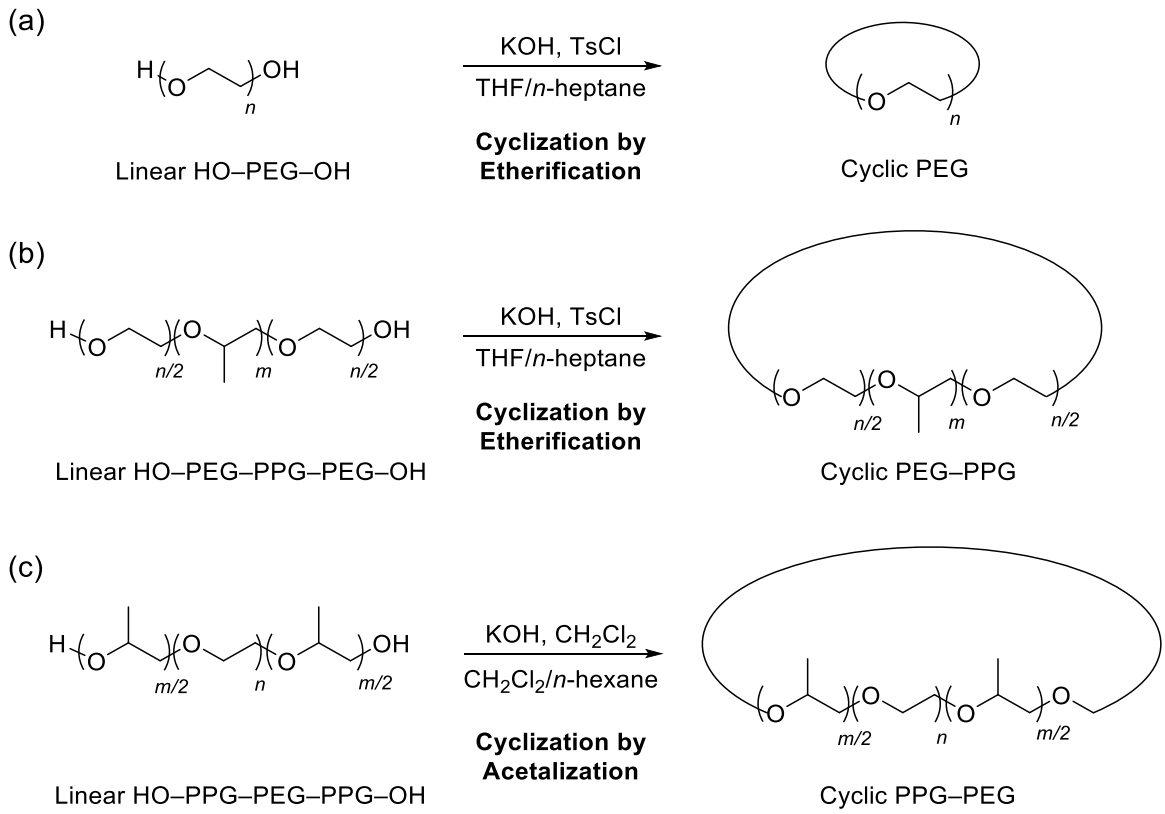

**Scheme 2-2. Dimethylation of (a) PEG homopolymer, (b) ABA-, and (c) BAB-type Pluronic Surfactants.**

(a)

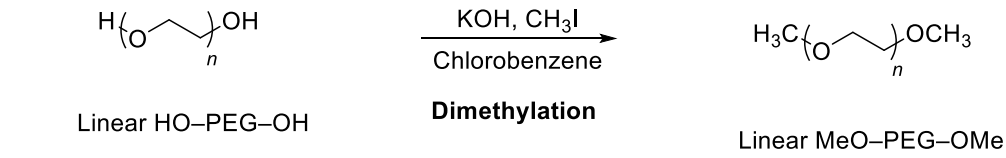


Linear HO–PEG–OH

Linear MeO–PEG–OMe

(b)

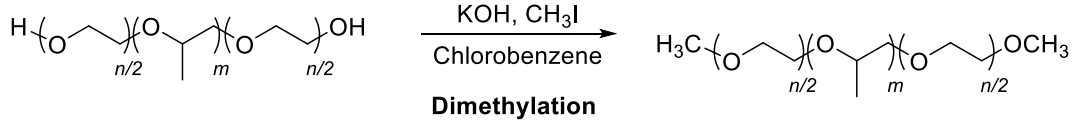


Linear HO–PEG–PPG–PEG–OH

Linear MeO–PEG–PPG–PEG–OMe

(c)

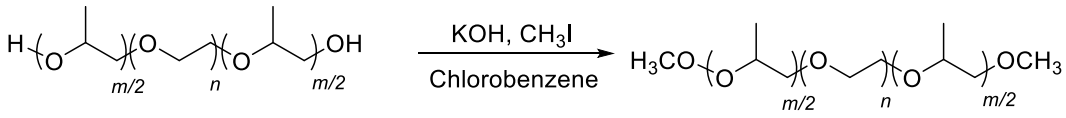


Linear HO–PPG–PEG–PPG–OH

Linear MeO–PPG–PEG–PPG–OMe

## 2.2. EXPERIMENTAL SECTION

### 2.2.1. Materials.

4-Toluenesulfonyl chloride (TsCl) (>98.0%, Junsei Chemical Co., Ltd.), iodomethane (>99.5%, Kanto Chemical Co., Inc.), sodium chloride (NaCl) (>99.0%, Kanto Chemical Co., Inc.), potassium hydroxide (KOH) (>85.5%, Kanto Chemical Co., Inc.), sodium sulfate ($Na_2SO_4$) (>99.0%, Kanto Chemical Co., Inc.), *n*-heptane (>99.0%, Kanto Chemical Co., Inc.), chlorobenzene (>99.0% Nacalai Tesque, Inc.), methanol (MeOH) (>99.5%, Kanto Chemical Co., Inc.), dichloromethane ($CH_2Cl_2$) (>99.0%, Kanto Chemical Co., Inc.) for work up, and chloroform ($CHCl_3$) (>99.0%, Kanto Chemical Co., Inc.) were used as received. Tetrahydrofuran (THF), dehydrated stabilizer free (>99.5%, Kanto Chemical Co., Inc.) and dehydrated $CH_2Cl_2$ (>99.5%, Kanto Chemical Co., Inc.) for reactions were purified by a solvent purification system (MBRAUN MB-SPS-Compact). Pluronic L35 (PEG–PPG–PEG), average $M_n$ ~1,900, PEG composition ~50 wt% (Sigma–Aldrich), Pluronic L64 (PEG–PPG–PEG), $M_n$ ~2,900, PEG composition ~40 wt% (Sigma–Aldrich), Pluronic P123 (PEG–PPG–PEG), $M_n$ ~5,800, PEG composition ~30 wt% (Sigma–Aldrich), Pluronic F68, $M_n$ ~8,400, PEG composition ~80 wt% (Sigma–Aldrich), Pluronic 10R5 (PPG–PEG–PPG), average $M_n$ ~2,000, PEG composition ~50 wt% (Sigma–Aldrich), and Pluronic 17R4 (PPG–PEG–

PPG), average $M_n$ ~2,700, PEG composition ~40 wt% (Sigma–Aldrich) were purified by recycling preparative SEC.

### 2.2.2. NMR.

$^1H$ (400 MHz) and $^{13}C$ NMR (100 MHz) were measured in $CDCl_3$ using a JEOL JNM-ESC400 instrument at ambient temperature.

### 2.2.3. Size exclusion chromatography (SEC).

Size exclusion chromatography (SEC) was measured using a JASCO PU-980 Plus pump with two Shodex KF-804L (8.0 mm × 300 mm) columns and a Shodex KF-G guard column equipped in a JASCO CO-2065 Plus column oven set at 40 °C. A JASCO RI-2031 Plus differential refractometer was used for detection. THF was used as a solvent, and the flow rate was set at 1.0 mL/min. Polystyrene (PS) standard samples were used for calibration, and the molecular weights were estimated by the following equation: $M_{n,SEC}$ (Pluronic or PEG) = $M_{n,SEC}$ (PS) × 0.798.[20]

### 2.2.4. Preparative SEC.

A Japan Analytical Industry LC-908 recycling preparative HPLC system (Hitachi L-7110 pump and JAI RI detector RI-5) was used. JAIGEL-2H and 3H columns and a

pre-column were connected in series. $CHCl_3$ was used as the solvent, and the flow rate was set at 3.5 mL/min.

### 2.2.5. Synthesis of cyclic Pluronic surfactants

**Synthesis of cyclic Pluronic L35 (*c*-L35).**

Pluronic L35 (***l*-L35(OH)**, 5.2 g, 2.7 mmol) and TsCl (0.67 g, 3.5 mmol) were dissolved in THF (50 mL) and slowly added at a rate of 10 μL/min over 96 h to a stirring suspension of KOH (4.3 g) in THF/*n*-heptane (75/25 v/v) (150 mL) in a 500 mL three neck flask at 40 °C under $N_2$. The reaction mixture was stirred for another 24 h at 40 °C. The resulting suspension was filtered and concentrated under reduced pressure. The residue was redissolved in $CH_2Cl_2$ and washed with brine three times. The combined organic phase was dried over $Na_2SO_4$ and concentrated under reduced pressure, and the residue was passed through a silica gel column using $CHCl_3$/MeOH (90/10 v/v) as an eluent. The crude product was fractionated by recycling preparative SEC. The obtained oil was dissolved in a small amount of $CH_2Cl_2$, and *n*-heptane was added to the solution until it became cloudy. The solvent mixture was partially evaporated under reduced pressure, where most of $CH_2Cl_2$ was removed. From the resulting suspension, the clear supernatant, mostly *n*-heptane, was collected and evaporated to dryness to give a colorless oil containing concentrated ***c*-L35**. This step was conducted several times to isolate ***c*-L35** (365 mg, 7.0%, $M_{n,SEC}$ = 1,480, $M_{p,SEC}$ = 1,570, $M_w/M_n$ = 1.16) as a colorless liquid. $^1$H NMR (400 MHz, $CDCl_3$): $\delta$ (ppm) 0.96–1.32 (m, –OCH(C*H*$_3$)C*H*$_2$O–), 3.28–3.75 (m, –OC*H*$_2$C*H*$_2$O–, –OC*H*(CH$_3$)C*H*$_2$O–). $^{13}$C NMR (400 MHz, $CDCl_3$): $\delta$ (ppm) 17.58 (–

OCH($C$H$_3$)CH$_2$O–), 68.73 (–OCH$_2$$C$H$_2$OCH(CH$_3$)CH$_2$O–), 70.68 (–O$C$H$_2$$C$H$_2$O–), 73.01–77.36 (–OCH(CH$_3$)$C$H$_2$O–, –O$C$H(CH$_3$)CH$_2$O–).

**Synthesis of cyclic Pluronic L64 (*c*-L64).**

Pluronic L64 (***l*-L64(OH)**, 2.5 g, 0.85 mmol) and TsCl (0.22 g, 1.1 mmol) were dissolved in THF (25 mL) and slowly added at a rate of 20 μL/min over 84 h to a stirring suspension of KOH (4.3 g) in THF/*n*-heptane (75/25 v/v) (150 mL) in a 200 mL two neck flask at 40 °C under $N_2$. The reaction mixture was stirred for another 24 h at 40 °C. The resulting suspension was filtered and concentrated under reduced pressure. The residue was redissolved in $CH_2Cl_2$ and washed with brine three times. The combined organic phase was dried over $Na_2SO_4$ and concentrated under reduced pressure, and the residue was passed through a silica gel column using $CHCl_3$/MeOH (90/10 v/v) as an eluent. The crude product was fractionated by recycling preparative SEC to isolate ***c*-L64** (293 mg, 11.7%, $M_{n,SEC}$ = 2,890, $M_{p,SEC}$ = 2,950, $M_w/M_n$ = 1.06) as a colorless liquid. $^1$H NMR (400 MHz, $CDCl_3$): $\delta$ (ppm) 0.90–1.35 (m, –OCH(C$H_3$)CH$_2$O–), 3.27–3.80 (m, –OC$H_2$C$H_2$O–, –OC$H$(CH$_3$)C$H_2$O–). $^{13}$C NMR (400 MHz, $CDCl_3$): $\delta$ (ppm) 17.47 (–OCH($C$H$_3$)CH$_2$O–), 68.65 (–OCH$_2$$C$H$_2$OCH(CH$_3$)CH$_2$O–), 70.69 (–O$C$H$_2$$C$H$_2$O–), 73.03–77.37 (–OCH(CH$_3$)$C$H$_2$O–, –O$C$H(CH$_3$)CH$_2$O–).

**Synthesis of cyclic Pluronic P123 (*c*-P123).**

Pluronic P123 (***l*-P123(OH)**, 4.5 g, 0.78 mmol) and TsCl (0.19 g, 1.0 mmol) were dissolved in THF (50 mL) and slowly added at a rate of 15 μL/min over 72 h to a stirring suspension of KOH (4.3 g) in THF/*n*-heptane (75/25 v/v) (150 mL) in a 500 mL three neck flask at 40 °C under $N_2$. The reaction mixture was stirred for another 24 h at 40 °C. The resulting suspension was filtered and concentrated under reduced pressure. The residue was redissolved in $CH_2Cl_2$ and washed with brine three times. The combined organic phase was dried over $Na_2SO_4$ and concentrated under reduced pressure, and the residue was passed through a silica gel column using $CHCl_3$/MeOH (90/10 v/v) as an eluent. The crude product was fractionated by recycling preparative SEC. The obtained oil was dissolved in a small amount of $CH_2Cl_2$, and *n*-heptane was added to the solution until it becomes cloudy. The solvent mixture was partially evaporated under reduced pressure, where most of $CH_2Cl_2$ was removed. From the resulting suspension, the clear supernatant, mostly *n*-heptane, was collected and evaporated to dryness to give a colorless oil containing concentrated ***c*-P123**. This step was conducted several times to isolate ***c*-P123** (190 mg, 4.2%, $M_{n,SEC}$ = 7,180, $M_{p,SEC}$ = 5,630, $M_w/M_n$ = 1.03) as a colorless liquid. $^1$H NMR (400 MHz, $CDCl_3$): $\delta$ (ppm) 0.94–1.37 (m, –OCH(C*H*$_3$)C*H*$_2$O–), 3.29–3.91 (m,

–OC$H_2$C$H_2$O–, –OC$H$($CH_3$)C$H_2$O–). $^{13}$C NMR (400 MHz, $CDCl_3$): $\delta$ (ppm) 17.47 (–OCH($CH_3$)$CH_2$O–), 68.52 (–OC$H_2$$CH_2$OCH($CH_3$)$CH_2$O–), 70.55 (–O$CH_2$$CH_2$O–), 72.95–77.37 (–OCH($CH_3$)$CH_2$O–, –O$CH$($CH_3$)$CH_2$O–).

**Synthesis of cyclic Pluronic F68 (*c*-F68).**

Pluronic F68 (***l*-F68(OH)**, 5.0 g, 0.60 mmol) and TsCl (0.15 g, 0.77 mmol) were dissolved in THF (50 mL) and slowly added at a rate of 20 μL/min over 66 h to a stirring suspension of KOH (4.3 g) in THF/*n*-heptane (75/25 v/v) (150 mL) in a 500 mL three neck flask at 40 °C under $N_2$. The reaction mixture was stirred for another 24 h at 40 °C. The resulting suspension was filtered and concentrated under reduced pressure. The residue was redissolved in $CH_2Cl_2$ and washed with brine three times. The combined organic phase was dried over $Na_2SO_4$ and concentrated under reduced pressure, and the residue was passed through a silica gel column using $CHCl_3$/MeOH (90/10 v/v) as an eluent. The crude product was fractionated by recycling preparative SEC to isolate ***c*-F68** (153 mg, 3.1%, $M_{n,SEC}$ = 7,830, $M_{p,SEC}$ = 6,790, $M_w/M_n$ = 1.04) as a white solid. $^1$H NMR (400 MHz, $CDCl_3$): $\delta$ (ppm) 0.95–1.37 (m, –OCH(C$H_3$)$CH_2$O–), 3.25–3.90 (m, –OC$H_2$C$H_2$O–, –OC$H$($CH_3$)C$H_2$O–). $^{13}$C NMR (400 MHz, $CDCl_3$): $\delta$ (ppm) 17.56 (–

OCH(*C*$H_3$)$CH_2O$–), 68.63 (–$OCH_2$*C*$H_2$OCH($CH_3$)$CH_2O$–), 70.47 (–O*C*$H_2$*C*$H_2O$–), 72.84–77.36 (–OCH($CH_3$)*C*$H_2O$–, –O*C*H($CH_3$)$CH_2O$–).

**Synthesis of cyclic Pluronic 10R5 (*c*-10R5).**

Pluronic 10R5 (***l*-10R5(OH)**, 5.0 g, 2.5 mmol) was dissolved in $CH_2Cl_2$/*n*-hexane (65/35 v/v) (25 mL) and slowly added at a rate of 10 μL/min over 65 h to a stirring suspension of KOH (7.0 g) in $CH_2Cl_2$/*n*-hexane (65/35 v/v) (150 mL) in a 500 mL three neck flask at 40 °C under $N_2$. The reaction mixture was stirred for another 24 h at 40 °C. The resulting suspension was filtered and concentrated under reduced pressure. The residue was redissolved in $CH_2Cl_2$ and washed with brine three times. The combined organic phase was dried over $Na_2SO_4$ and concentrated under reduced pressure, and the residue was passed through a silica gel column using $CHCl_3$/MeOH (90/10, v/v) as an eluent. The crude product was fractionated by recycling preparative SEC to isolate ***c*-10R5** (166 mg, 3.3%, $M_{n,SEC}$ = 1,500, $M_{p,SEC}$ = 1,450, $M_w/M_n$ = 1.08) as a colorless liquid. $^1$H NMR (400 MHz, $CDCl_3$): $\delta$ (ppm) 0.87–1.31 (m, –OCH(C*H*$_3$)$CH_2O$–), 3.24–3.91 (m, –OC*H*$_2$C*H*$_2$O–, –OC*H*($CH_3$)C*H*$_2$O–), 4.65–4.87 (m, –OC*H*$_2$O–). $^{13}$C NMR (400 MHz, $CDCl_3$): $\delta$ (ppm) 17.52 (–OCH(*C*$H_3$)$CH_2O$–), 70.62 (–O*C*$H_2$*C*$H_2O$–), 72.92–77.37 (–OCH($CH_3$)*C*$H_2O$–, –O*C*H($CH_3$)$CH_2O$–), 92.36 (–O*C*$H_2O$–).

**Synthesis of cyclic Pluronic 17R4 (*c*-17R4).**

Pluronic 17R4 (***l*-17R4(OH)**, 5.0 g, 1.9 mmol) was dissolved in $CH_2Cl_2$/*n*-hexane (65/35 v/v) (25 mL) and slowly added at a rate of 12.5 μL/min over 36 h to a stirring suspension of KOH (7.0 g) in $CH_2Cl_2$/*n*-hexane (65/35 v/v) (150 mL) in a 500 mL three neck flask at 40 °C under $N_2$. The reaction mixture was stirred for another 24 h at 40 °C. The resulting suspension was filtered and concentrated under reduced pressure. The residue was redissolved in $CH_2Cl_2$ and washed with brine three times. The combined organic phase was dried over $Na_2SO_4$ and concentrated under reduced pressure, and the residue was passed through a silica gel column using $CHCl_3$/MeOH (90/10, v/v) as an eluent. The crude product was fractionated by recycling preparative SEC. The obtained oil was dissolved in a small amount of $CH_2Cl_2$, and *n*-heptane was added to the solution until it becomes cloudy. The solvent mixture was partially evaporated under reduced pressure, where most of $CH_2Cl_2$ was removed. From the resulting suspension, the clear supernatant, mostly *n*-heptane, was collected and evaporated to dryness to give a colorless oil containing concentrated ***c*-17R4**. This step was conducted several times to isolate ***c*-17R4** (246 mg, 5.0%, $M_{n,SEC}$ = 2,780, $M_{p,SEC}$ = 2,690, $M_w/M_n$ = 1.07) as a colorless liquid. $^1$H NMR (400 MHz, $CDCl_3$): $\delta$ (ppm) 0.92–1.39 (m, –OCH(C*H*$_3$)C*H*$_2$O–), 3.22–3.95 (m,

–OC*H*$_2$C*H*$_2$O–, –OC*H*(CH$_3$)C*H*$_2$O–), 4.74–4.89 (m, –OC*H*$_2$O–). $^{13}$C NMR (400 MHz, $CDCl_3$): $\delta$ (ppm) 17.60 (–OCH(*C*H$_3$)CH$_2$O–), 70.69 (–O*C*H$_2$*C*H$_2$O–), 73.04–77.33 (–OCH(CH$_3$)*C*H$_2$O–, –O*C*H(CH$_3$)CH$_2$O–), 99.98 (–O*C*H$_2$O–).

### 2.2.6. Synthesis of dimethylated Pluronic surfactants

Dimethylation of Pluronic surfactants (L35, L64, 10R5, and 17R4) was performed following a similar method for the dimethylation of PEG.[21] Typically, a solution of ***l*-L64(OH)** (5.0 g, 1.7 mmol) in chlorobenzene (100 mL) was dropwise added at a rate of 40 μL/min into a solution of chlorobenzene (40 mL) containing KOH (5.0 g) and iodomethane (0.72 g, 5.1 mmol) for over 60 min under Ar. After the addition was completed, the mixture was stirred at room temperature for over 24 h. The resulting suspension was filtered, and the filtrate was concentrated under reduced pressure. The residue was dissolved in $CH_2Cl_2$ and washed with brine three times, dried over $Na_2SO_4$, and concentrated under reduced pressure. The residue was dissolved in $CHCl_3$ and passed through a silica gel column using $CHCl_3$/MeOH (90/10, v/v) as an eluent, and concentrated under reduced pressure to give ***l*-L64(OMe)** (3.85 g, 77 %) as a colorless liquid. The SEC and NMR data follow:

***l*-L35(OMe).** SEC: $M_{n,SEC}$ = 2,310, $M_{p,SEC}$ = 2,610, $M_w/M_n$ = 1.12. $^1$H NMR (400 MHz, $CDCl_3$): $\delta$ (ppm) 0.95–1.34 (m, –OCH(C*H*$_3$)C$H_2$O–), 3.26–3.81 (m, –OC*H*$_2$C*H*$_2$O–, –OC*H*(CH$_3$)C*H*$_2$O–), 3.36 (s, –OCH$_2$CH$_2$OC*H*$_3$). $^{13}$C NMR (400 MHz, $CDCl_3$): $\delta$ (ppm) 17.58 (–OCH(*C*H$_3$)CH$_2$O–), 59.15 (–OCH$_2$CH$_2$O*C*H$_3$), 68.74 (–OCH$_2$*C*H$_2$OCH(CH$_3$)CH$_2$O–), 70.70 (–O*C*H$_2$*C*H$_2$O–), 72.06 (–OCH$_2$*C*H$_2$OCH$_3$), 73.02–77.36 (–OCH(CH$_3$)

*C*$H_2$O–, –O*C*H($CH_3$)$CH_2$O–).

***l*-L64(OMe).** SEC: $M_{n,SEC}$ = 4,360, $M_{p,SEC}$ = 4,460, $M_w/M_n$ = 1.04. $^1$H NMR (400 MHz, $CDCl_3$): $\delta$ (ppm) 0.94–1.28 (m, –OCH(C*H*$_3$)$CH_2$O–), 3.26–3.99 (m, –OC*H*$_2$C*H*$_2$O–, –OC*H*($CH_3$)C*H*$_2$O–), 3.35 (s, –$OCH_2CH_2OCH_3$). $^{13}$C NMR (400 MHz, $CDCl_3$): $\delta$ (ppm) 17.57 (–OCH(*C*$H_3$)$CH_2$O–), 59.15 (–$OCH_2CH_2$–O*C*$H_3$), 68.70 (–$OCH_2CH_2OCH(CH_3)$ $CH_2$O–), 70.67 (–O*C*$H_2$*C*$H_2$O–), 72.04 (–$OCH_2CH_2OCH_3$), 72.98–77.36 (–OCH($CH_3$) *C*$H_2$O–, –O*C*H($CH_3$)$CH_2$O–).

***l*-10R5(OMe).** SEC: $M_{n,SEC}$ = 2,080, $M_{p,SEC}$ = 2,030, $M_w/M_n$ = 1.09. $^1$H NMR (400 MHz, $CDCl_3$): $\delta$ (ppm) 0.95–1.28 (m, –OCH(C*H*$_3$)$CH_2$O–), 3.10–3.93 (m, –OC*H*$_2$C*H*$_2$O–, –OC*H*($CH_3$)C*H*$_2$O–), 3.36 (s, –$OCH(CH_3)CH_2OCH_3$). $^{13}$C NMR (400 MHz, $CDCl_3$): $\delta$ (ppm) 17.56 (–OCH(*C*$H_3$)$CH_2$O–), 56.85 (–O*C*$H_3$), 70.66 (–O*C*$H_2$*C*$H_2$O–), 72.96–77.36 (–OCH($CH_3$)*C*$H_2$O–, –O*C*H($CH_3$)$CH_2$O–).

***l*-17R4(OMe).** SEC: $M_{n,SEC}$ = 3,470, $M_{p,SEC}$ = 3,550, $M_w/M_n$ = 1.06. $^1$H NMR (400 MHz, $CDCl_3$): $\delta$ (ppm) 0.96–1.24 (m, –OCH(C*H*$_3$)$CH_2$O–), 3.27–3.82 (m, –OC*H*$_2$C*H*$_2$O–, –OC*H*($CH_3$)C*H*$_2$O–), 3.37 (s, –OC*H*$_3$). $^{13}$C NMR (400 MHz, $CDCl_3$): $\delta$ (ppm) 17.47 (–

OCH(*C*H$_3$)CH$_2$O–), 56.74 (–O*C*H$_3$), 70.56 (–O*C*H$_2$*C*H$_2$O–), 72.84–77.36 (–OCH(CH$_3$)*C*H$_2$O–, –O*C*H(CH$_3$)CH$_2$O–).

### 2.2.7. Surface tension ($\gamma$) measurement.

$\gamma$ for an aqueous solution of PEG or a Pluronic surfactant of various concentrations at ambient temperature was measured through a pendant drop method using a Kyowa Interfacial Science Dropmaster Contact Angle Meter. A sample solution of the highest concentration for each polymer was prepared by the addition of Milli-Q water to the polymer and stirring overnight until total dissolution. Other concentrations were prepared by diluting this sample. All samples were prepared and stirred for at least 12 h prior to the measurement. Each sample solution was equilibrated for at least 30 min after drop formation on the tip of a syringe needle, in order to ensure surfactant arrangement at the interface. $\gamma$ was monitored at intervals and recorded after the value became stable. Image analysis was conducted through the Young–Laplace method, and the average of 10 measurements for each sample at each concentration was used. For dynamic surface tension measurements of PEG solution, the monitored $\gamma$ values at intervals were plotted against elapsed time until a stable plateau was observed.

## 2.3. RESULTS AND DISCUSSION

### 2.3.1. Synthesis of cyclic PEG and Pluronic Surfactants

Cyclization of a PEG homopolymer and ABA-type Pluronic surfactants having hydroxyl end groups was performed by the Williamson ether synthesis following a previous method (Schemes 2-1a and 2-1b).[21] The reaction was carried out under an inert gas atmosphere at 40 °C by slowly dropping a THF solution of a prepolymer and TsCl at a rate of 20 μL/min into a THF/*n*-heptane suspension of KOH. The mixture was stirred for a total of 3 to 4 d, and the obtained crude product was fractionated by preparative SEC. For the PEG homopolymer, L35 and P123, pure cyclized products were extracted with *n*-heptane using the difference in solubility between the linear and cyclic polymers. The SEC traces after the cyclization reaction shifted to a lower molecular weight while maintaining unimodality (Figures 2-2b, S2-1d, S2-2c, S2-3c, and S2-4c). In the case of L64, $M_{p,SEC}$ before and after cyclization was 4,460 and 2,950 Da with polydispersity index of 1.05 and 1.06, respectively (Table 2-1). Furthermore, the $^{13}C$ NMR spectrum of the products confirmed the complete disappearance of the signal from the carbon atoms adjacent to the hydroxyl groups (Figure 2-2a, "a", 61.5 ppm) shown in Figure 2-2c as well as in Figures S2-1b, S2-2a, S2-3a and S2-4a. The PEG composition estimated from the

$^{1}$H NMR spectra (Figure 2-2d, S2-2b, S2-3b and S2-4b) was nearly unchanged for all the ABA-type Pluronic surfactants. These data suggest successful cyclization.

**Table 2-1.** Properties of linear and cyclic PEG and Pluronic surfactants.

| Abbreviation | Structure[a] | $M_{n,SEC}$[b] (Da) | $M_{p,SEC}$[b] (Da) | $M_w/M_n$ | $M_p$ ratio[c] | PEG composition (wt%) | $\gamma$ (mN/m) | | | $A$[d] (Å$^2$) |
|---|---|---|---|---|---|---|---|---|---|---|
| | | | | | | | 1.0 g/L | 3.0 g/L | 10 g/L | |
| ***l*-PEG(OH)** | *linear* HO–$PEG_{53}$–OH | 2,360 | 2,300 | 1.06 | - | 100 | 60.0 | 58.5 | 57.1 | 410 |
| ***l*-PEG(OMe)** | *linear* MeO–$PEG_{53}$–OMe | 2,390 | 2,480 | 1.06 | 1.1 | 100 | 60.3 | 59.6 | 57.0 | 380 |
| ***c*-PEG** | *cyclic* $PEG_{53}$ | 1,820 | 1,960 | 1.08 | 0.85 | 100 | 48.8 | 45.5 | 40.7 | 100 |
| ***l*-L35(OH)** | *linear* HO–$PEG_{13}$–$PPG_{18}$–$PEG_{13}$–OH | 2,200 | 2,400 | 1.13 | - | 51 | 49.7 | 46.1 | 39.9 | 180 |
| ***l*-L35(OMe)** | *linear* MeO–$PEG_{13}$–$PPG_{18}$–$PEG_{13}$–OMe | 2,310 | 2,610 | 1.12 | 1.1 | 51 | 47.2 | 45.1 | 40.4 | -[e] |
| ***c*-L35** | *cyclic* $PEG_{26}$–$PPG_{18}$ | 1,480 | 1,570 | 1.16 | 0.65 | 52 | 45.3 | 43.2 | 38.2 | 160 |
| ***l*-L64(OH)** | *linear* HO–$PEG_{20}$–$PPG_{45}$–$PEG_{20}$–OH | 4,440 | 4,460 | 1.05 | - | 40 | 41.4 | 42.1 | 40.8 | 460 |
| ***l*-L64(OMe)** | *linear* MeO–$PEG_{20}$–$PPG_{45}$–$PEG_{20}$–OMe | 4,360 | 4,460 | 1.04 | 1.0 | 44 | 43.5 | 41.7 | 40.8 | 500 |
| ***c*-L64** | *cyclic* $PEG_{40}$–$PPG_{45}$ | 2,890 | 2,950 | 1.06 | 0.66 | 41 | 40.8 | 39.8 | 38.6 | 390 |
| ***l*-P123(OH)** | *linear* HO–$PEG_{32}$–$PPG_{105}$–$PEG_{32}$–OH | 8,930 | 7,580 | 1.03 | - | 32 | 35.1 | 34.4 | 32.7 | 320 |
| ***c*-P123** | *cyclic* $PEG_{64}$–$PPG_{105}$ | 7,180 | 5,630 | 1.03 | 0.74 | 34 | 35.9 | 32.6 | 32.2 | 290 |
| ***l*-F68(OH)** | *linear* HO$PEG_{94}$–$PPG_{34}$–$PEG_{94}$–OH | 10,260 | 9,030 | 1.05 | - | 80 | 47.6 | 45.9 | 43.4 | 280 |
| ***c*-F68** | *cyclic* $PEG_{188}$–$PPG_{34}$ | 7,830 | 6,790 | 1.04 | 0.75 | 81 | 44.2 | 41.4 | 38.9 | 190 |
| ***l*-10R5(OH)** | *linear* HO–$PPG_{10}$–$PEG_{28}$–$PPG_{10}$–OH | 2,360 | 2,540 | 1.09 | - | 52 | 53.4 | 51.4 | 48.5 | 350 |
| ***l*-10R5(OMe)** | *linear* MeO–$PPG_{10}$–$PEG_{28}$–$PPG_{10}$–OMe | 2,080 | 2,030 | 1.09 | 0.80 | 53 | 47.9 | 46.7 | 45.8 | 390 |
| ***c*-10R5** | *cyclic* $PPG_{20}$–$PEG_{28}$ | 1,500 | 1,450 | 1.08 | 0.57 | 55 | 44.6 | 43.1 | 42.7 | 290 |
| ***l*-17R4(OH)** | *linear* HO–$PPG_{19}$–$PEG_{36}$–$PPG_{19}$–OH | 3,790 | 3,870 | 1.04 | - | 42 | 44.8 | 43.5 | 42.0 | 350 |
| ***l*-17R4(OMe)** | *linear* MeO–$PPG_{19}$–$PEG_{36}$–$PPG_{19}$–OMe | 3,470 | 3,550 | 1.06 | 0.92 | 43 | 44.3 | 43.5 | 42.8 | 420 |
| ***c*-17R4** | *cyclic* $PPG_{38}$–$PEG_{36}$ | 2,780 | 2,690 | 1.07 | 0.70 | 42 | 41.5 | 39.5 | 35.1 | 200 |

[a]Calculated from $M_{n,SEC}$ values and NMR peak ratios of the PEG to PPG segments of the linear polymers with hydroxyl end groups. The $DP_n$ of each segment for the cyclized and dimethylated products are regarded unchanged to their prepolymers.

[b]Determined by SEC in THF using polystyrene standards. The molecular weights of the Pluronic surfactants were estimated by the equation $M_{n,SEC}$ (Pluronic) = $M_{n,SEC}$(PS) × 0.798.[20]

[c]$M_{p,SEC}$ value of a cyclized or dimethylated Pluronic surfactant divided by that of the corresponding linear prepolymer with hydroxy end groups.

[d]Calculated from the slope of the linear fit of $\gamma$ vs. log $c$ plot at concentrations above the completion of surfactant depletion.

[e]Error of linear regression for ***l*-L35(OMe)** was large, and thus, $A$ cannot be determined.

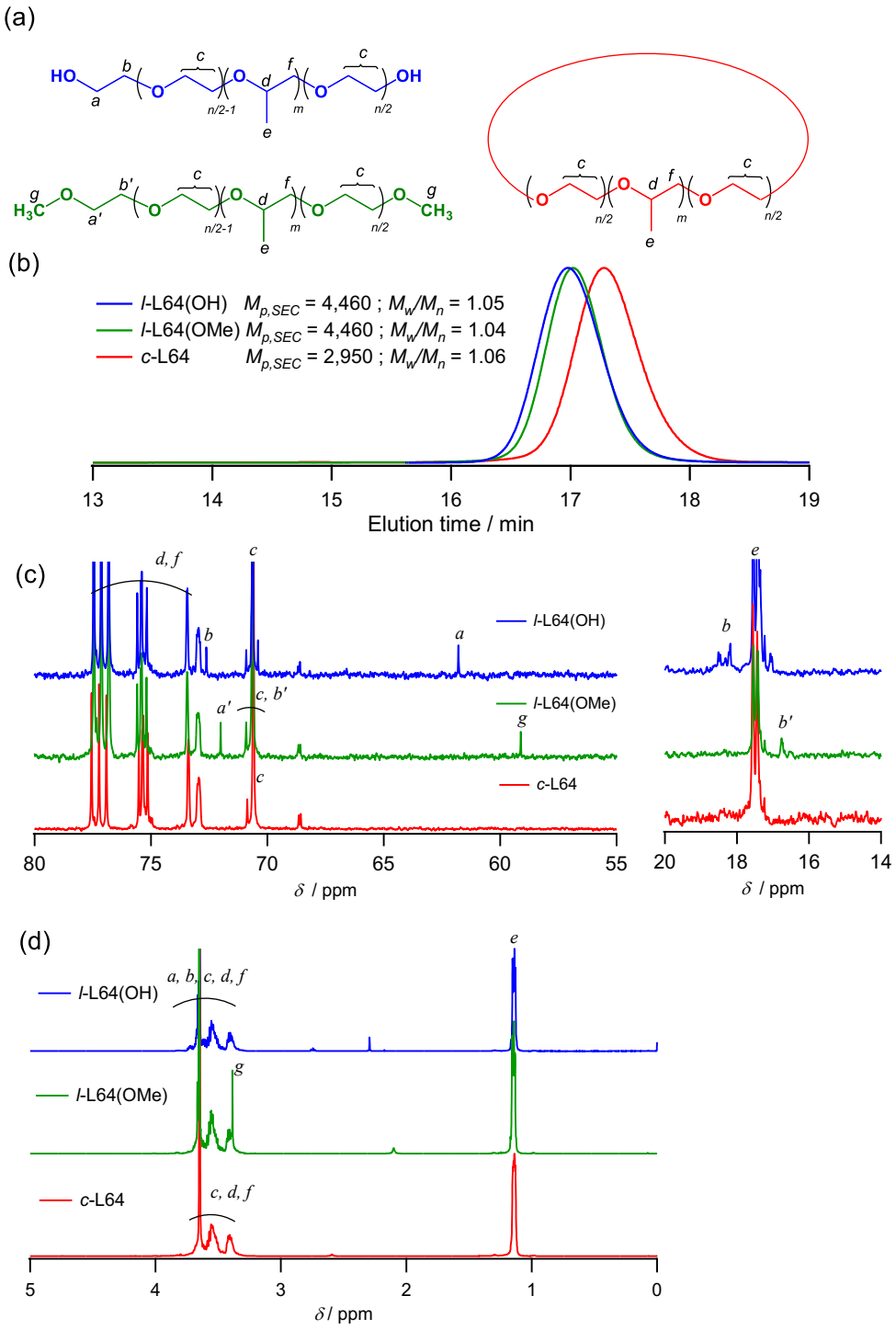


**Figure 2-2.** (a) Chemical structures, (b) SEC traces, (c) $^{13}$C NMR spectra, (d) $^{1}$H NMR spectra of ***l*-L64(OH)**, ***l*-L64(OMe)**, and ***c*-L64**.

Likewise, the cyclization of the BAB-type Pluronic was initially performed by the etherification procedure. However, the reaction did not proceed likely because of the secondary alcohol at one of the chain ends, where the BAB-type Pluronic surfactants have asymmetric PPG segments with a primary alcohol at a chain end and a secondary alcohol at the other (Figure 2-3a). For that reason, cyclization by acetification was applied (Scheme 2-1c).[19] Thus, 5.0 g of a BAB-type Pluronic surfactant was dissolved in 25 mL of $CH_2Cl_2$/*n*-hexane (65/35 v/v), and the solution was slowly added to into KOH (7.0 g) dispersed in a mixture of $CH_2Cl_2$/*n*-hexane (65/35 v/v) at a rate of 12.5 μL/min. The mixture was stirred at 30 °C for 40 h or more. After filtration of the reaction mixture, the crude product was isolated by silica gel column chromatography and preparative recycle SEC to give a cyclized surfactant. Similar to the case of the ABA-types, a decrease in $M_{p,SEC}$ was observed (Figures 2-3b and S2-5c). In the case of 17R4, $M_{p,SEC}$ shifted from 3,870 to 2,690 with a retention of a narrow PDI (Table 2-1). $^{13}C$ NMR shows the complete disappearance of the signals arising from the chain ends ("a" at 67.4 ppm and "h" at 65.5 ppm) and the emergence of a signal at 100.0 ppm (signal "k") from the acetal carbon in Figure 2-3c, while signals of the acetal group also clearly appeared at 4.74–4.89 ppm in $^1H$ NMR (Figure 2-3d). These suggest that the cyclic product was successfully formed through an acetal linkage.

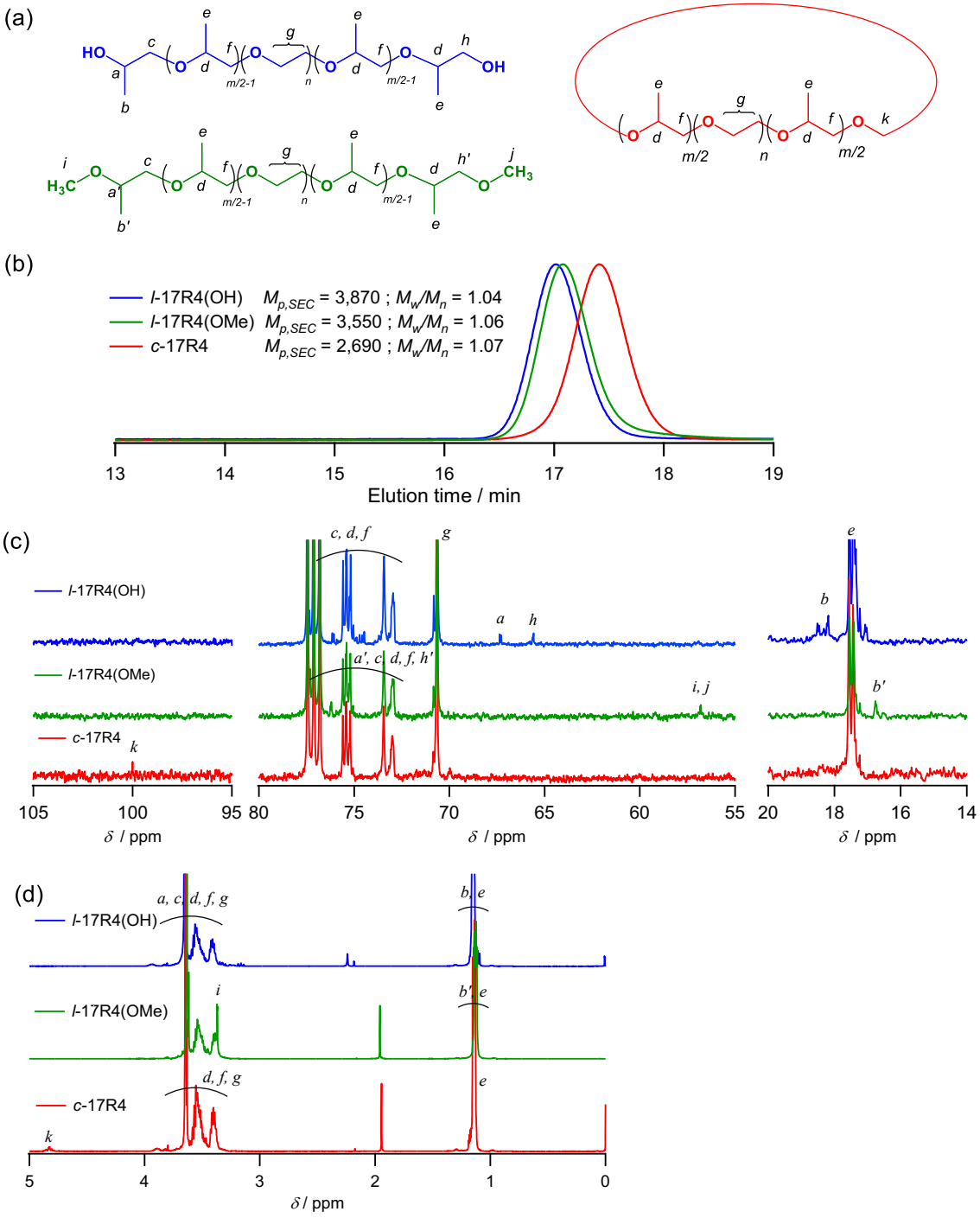


**Figure 2-3.** (a) Chemical structure, (b) SEC traces, (c) $^{13}$C NMR spectra, (d) $^{1}$H NMR spectra of ***l*-17R4(OH)**, ***l*-17R4(OMe)**, and ***c*-17R4**.

Concerning the very low isolated yields (3.1%–11.7%) of the cyclic polymers, the purity was prioritized over the yield, resulting in major loss during the isolation. SEC traces of the crude products (Figure S2-6) indicate the actual proportion of the cyclic polymers formed was much higher than the yield. For example, an analysis was carried out through the peak deconvolution of the SEC trace of crude cyclic PEG (***c*-PEG**) in Figure S2-7, and the proportion of ***c*-PEG** within the crude was determined to be 56%.

### 2.3.2. Synthesis of Dimethylated Pluronic Surfactants

Methylation of the chain ends of both ABA and BAB-type Pluronic surfactants was performed in a similar method described for that of PEG homopolymers (Scheme 2-2).[21] A Pluronic surfactant solution in chlorobenzene was dropwise added to a suspension of KOH and iodomethane in chlorobenzene under an inert gas atmosphere at ambient temperature. The mixture was stirred for an additional 24 h, and the obtained product was purified through filtration and silica gel column chromatography. Overall, SEC traces of the dimethylated polymers displayed similar $M_{n,SEC}$ and $M_{p,SEC}$ values to those of the respective prepolymers. In the case of ***l*-L64(OMe)**, $^{13}C$ NMR clearly indicate a down-field shift of a signal for carbon atom "a" from 61.8 to 72.0 ppm, while an emergence of a signal at 59.2 ppm was observed for the carbon atom "g" of the chain-end methoxy

groups (Figure 2-2c). From the $^{1}$H NMR spectra, the signal of methoxy groups was observed as a sharp peak at 3.35 ppm. In the case of ***l*-17R4(OMe)**, complete disappearance of signals "a" and "h" (67.4 and 65.5 ppm, respectively) and an emergence of a peak at 56.7 ppm was observed in the $^{13}$C NMR spectra, attributed to the carbon atoms "i" and "j" of the chain-end methoxy groups (Figure 2-3c). A signal from the methoxy groups was also observed in the $^{1}$H NMR spectra at 3.37 ppm. Consistent data was obtained for ***l*-L35(OMe)** (Figure S2-2) and ***l*-10R5(OMe)** (Figure S2-5), suggesting successful dimethylation of both ABA and BAB-type Pluronic surfactants.

The decrease in $M_{p,SEC}$ upon cyclization can be rationally explained by the reduced hydrodynamic volume of the cyclic species compared to their linear counterparts. The $M_p$ ratio in Table 2-1 indicates the $M_{p,SEC}$ values of the cyclized or dimethylated Pluronic surfactants divided by that of the linear prepolymers with hydroxy end groups. The reduction was more pronounced for polymers that possess a smaller molecular weight within the same block sequence. In the meantime, the SEC traces of the dimethylated linear species remained mostly unchanged for the PEG homopolymer and ABA-type surfactants ($M_p$ ratio = 1.0–1.1), while a shift toward a lower molecular weight was observed upon dimethylation of the BAB-type surfactants with $M_p$ ratio of 0.80 for ***l*-10R5(OMe)** and 0.92 for ***l*-17R4(OMe)**. This suggests that the chain-end hydroxy groups

attached to the hydrophobic PPG segments in the BAB-types strongly influence the hydrodynamic volume while the effect of the hydroxy end groups on the hydrophilic PEG segments in the ABA-types was limited.

### 2.3.3. Surface Tension ($\gamma$)

Surface tension ($\gamma$) was measured to evaluate the surface activity of the synthesized cyclic Pluronic surfactants, along with the linear prepolymers and dimethylated counterparts, by the hanging drop method using a contact angle meter and analyzed by the Young–Laplace method. In order to clarify the effects of the topology and chain ends, $\gamma$ for the hydroxy- and methoxy-terminated linear and cyclic PEG homopolymers, namely ***l*-PEG(OH)**, ***l*-PEG(OMe)**, and ***c*-PEG**, respectively, was first measured. When the different topologies are compared at a given concentration, the $\gamma$ values for ***c*-PEG** was significantly reduced comparing to its linear counterparts. For example, at a polymer concentration of 10 g/L, $\gamma$ for ***l*-PEG(OH)** and ***l*-PEG(OMe)** were 57.1 and 57.0 mN/m, respectively, while that for ***c*-PEG** was 40.7 mN/m (Table 2-1 and Figure 2-4a).

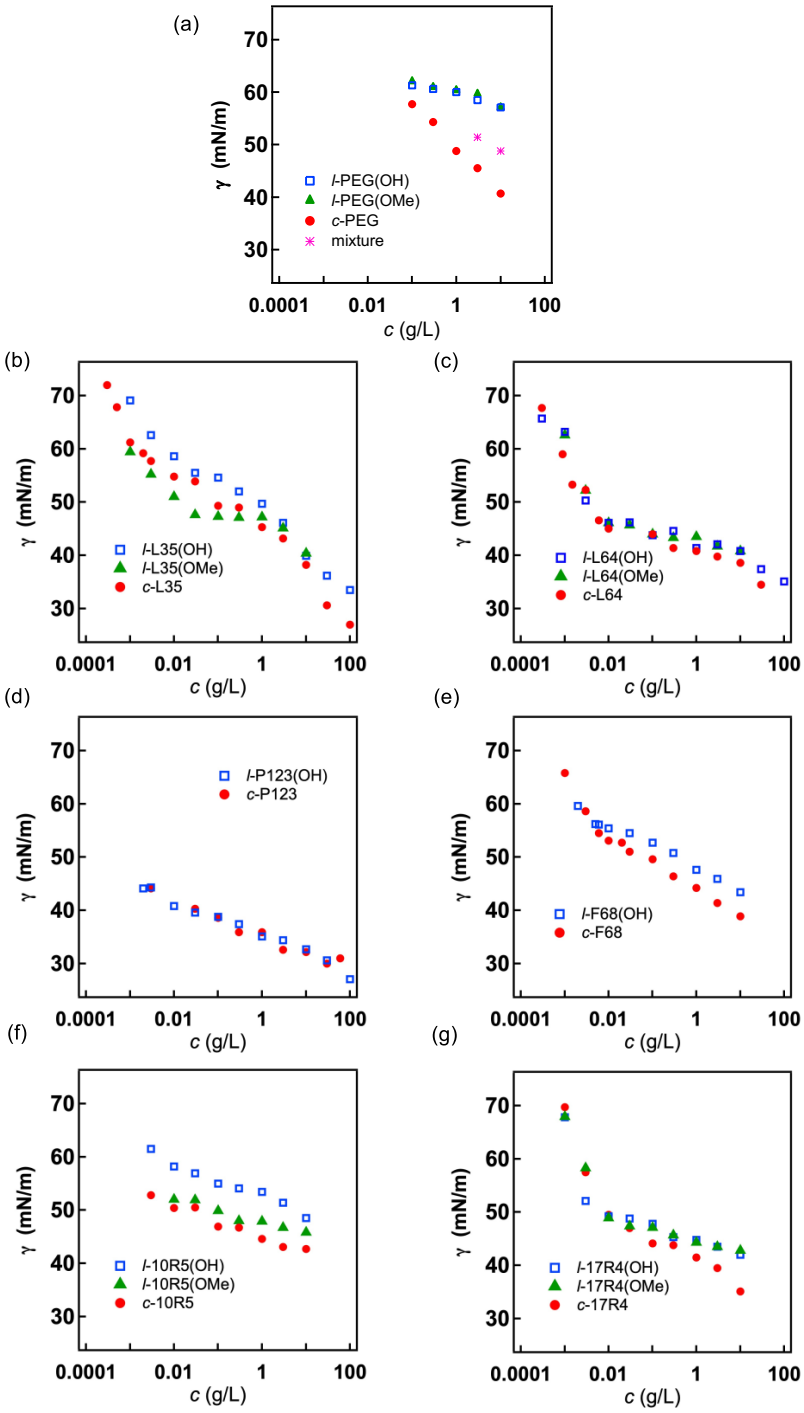


**Figure 2-4.** Plots of the surface tension ($\gamma$) versus the concentration ($c$) for hydroxy- and methoxy-terminated linear and cyclic (a) PEG homopolymers, (b) L35, (c) L64, (d) P123, (e) F68, (f) 10R5, and (g) 17R4. In the plot for the PEG homopolymers, "mixture" indicates a one-to-one mixture of ***l*-PEG(OH)** and ***c*-PEG**.

Considering that $\gamma$ for pure water is 72 mN/m at 25 °C,[22] the cyclic topology in PEG drastically improved the surface activity. This deviation is possibly due to the large difference in the density of molecules arranged at the surface of water between linear and cyclic PEG, which is expected to be related to the occupational area ($A$) of a single molecule. Cyclic polymers including PEG are known to have a smaller hydrodynamic volume[23, 24] and therefore considered to possess a smaller $A$ to their linear counterparts. Thus, $A$ was calculated for each PEG using the following Gibbs adsorption isotherm equations at concentrations where contribution of polymer depletion was clearly unobserved:[25, 26]

$$\Gamma = -\frac{1}{2.303RT}\frac{d\gamma}{d\log c} \quad (1)$$

$$A = \frac{1}{\Gamma N} \quad (2)$$

, where $\Gamma$ is the surface excess concentration, $R$ is the gas constant, $T$ is the absolute temperature, $c$ is the polymer concentration, and $N$ is the Avogadro number. Calculated values indeed confer significantly reduced $A$ for ***c*-PEG** (100 Å$^2$) compared to its linear counterparts (***l*-PEG(OH)**, 410 Å$^2$; ***l*-PEG(OMe)**, 380 Å$^2$). Interestingly, the linear-to-cyclic ratio of $A$ for present PEG ($A_{\mathrm{linear}}/A_{\mathrm{cyclic}} \sim 4$) was much more prominent to the reported ratio of the squared effective hydrodynamic radius of poly(ethylene oxide) ($R_{\mathrm{h,linear}}^2/R_{\mathrm{h,cyclic}}^2 = 1.9 \pm 0.1$).[27] Thus, ***c*-PEG** strongly adsorbed to the air–water to form

a dense PEG layer with small $A$ compared to $R_h^2$ in the bulk solution state. This likely led to the higher surface activity and decrease in $\gamma$. Moreover, the elimination of the chain-end hydroxy groups of linear PEG did not produce significant difference in $\gamma$ or $A$, and therefore the drastic improvement of surface activity for ***c*-PEG** was indeed the consequence of its cyclic topology.

To consider the possibility of topology-dependent selective or preferential adsorption to the air-water interface, $\gamma$ measurements for aqueous solutions of a one-to-one mixture of ***l*-PEG(OH)** and ***c*-PEG** were carried out, revealing $\gamma$ for the mixture solutions was in between the values obtained for the single-component solutions of ***l*-PEG(OH)** and ***c*-PEG**. For example, in a 10 mg/mL mixture solution, the polymer concentration was 5 mg/mL for both ***l*-PEG(OH)** and ***c*-PEG**. Should selective adsorption of ***c*-PEG** take place, the $\gamma$ value would be close to that of the pure ***c*-PEG** solution at 5 mg/mL. Since this was not observed, the adsorption of ***l*-PEG(OH)** and ***c*-PEG** was likely statistical.

The $\gamma$ values of hydroxy- and methoxy-terminated linear and cyclic L35, L64, P123, and F68, which are ABA-type Pluronic surfactants, were also measured at various concentrations (Figures 2-4 b–g). The surface tension curves of L35 (PEG composition ~50 wt%), L64 (PEG composition ~40 wt%), and F68 (PEG composition ~80 wt%) show

that surface activity is improved by cyclization, and it was found that the higher the PEG composition the surfactant had, the larger the decrease in $\gamma$ upon cyclization appeared in conjunction with the case of ***c*-PEG** (Table 2-1). For P123 having a PEG composition of only ~30 wt%, the $\gamma$ plots of the linear and cyclic were almost identical (Figure 2-4d), while an evident decrease in $\gamma$ values for ***c*-F68** (PEG composition ~80 wt%) was observed compared to ***l*-F68(OH)** (Figure 2-4e). The phenomenon that the change in $\gamma$ associated with cyclization increases in proportion to the length of hydrophilic segment has also been reported by Imura and coworkers.[28] Focusing on the interface, it is conceivable that PPG, the middle hydrophobic segment, is fixed to the interface, and the PEG segments spread in water (Figure 2-5). Again, the hydrodynamic volume of the solvated PEG segments becomes smaller by cyclization, while less solvated PPG segments are less affected by cyclization. Thus, the larger the PEG composition the surfactant had, the larger the effect of cyclization was. For 10R5 (PEG composition ~50 wt%) and 17R4 (PEG composition ~40 wt%), which are BAB-type, the decrease in $\gamma$ due to cyclization was also observed. In these cases, both chain ends are expected to be located at the air–water interface. Although L35 and 10R5 have relatively similar PEG/PPG ratios, $A$ of L35 decreased from 180 Å$^2$ (***l*-L35(OH)**) to 160 Å$^2$ (***c*-L35**), while that of 10R5 intensely shrank from 350 Å$^2$ (***l*-10R5(OH)**) to 290 Å$^2$ (***c*-10R5**) shown in

Table 2-1. Unlike the PEG homopolymers, the PPG segments in both linear and cyclic Pluronic surfactants were strongly attracted to the air–water interface, resulting in the smaller but still significant difference in *A* arising from the topology.

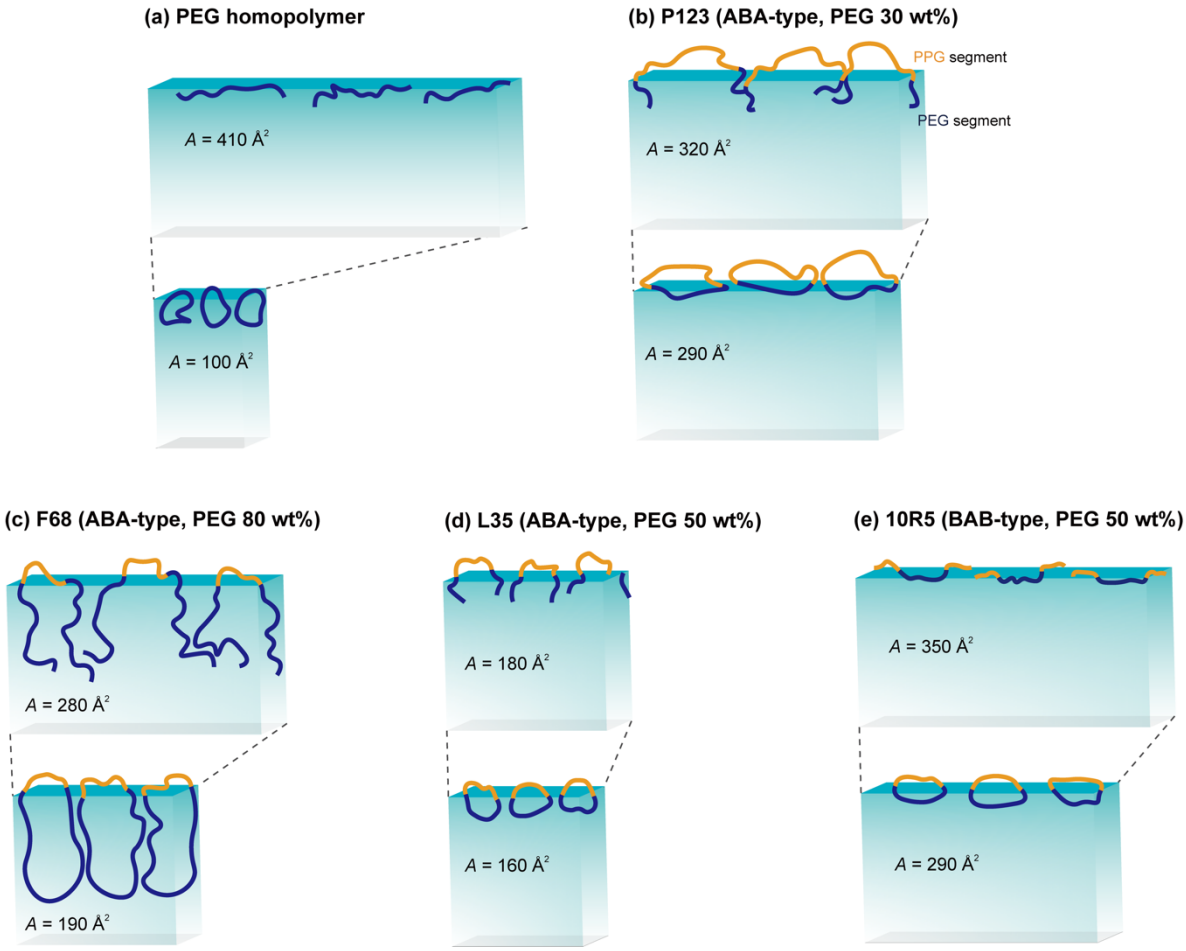


**Figure 2-5.** Schematic representations of the conformation and occupation area ($A$) of (a) PEG homopolymer, (b) P123, (c) F68, (d) L35, and (e) 10R5 located at the air–water interface. Linear surfactants are shown above and cyclic surfactants below. The higher the PEG composition the surfactant had, the larger the decrease in $\gamma$ upon cyclization appeared. In the case of the PEG homopolymer, $A$ decreased from 410 Å$^2$ (***l*-PEG(OH)**) to 100 Å$^2$ (***c*-PEG**)

Estimation of $A$ from $\gamma$ measurements for Pluronic surfactants contains ambiguity since $\gamma$ at dilute regions are profoundly affected by various factors still in dispute. For instance, a change in the slope for L64, F68, and 17R4 occur at dilute concentrations significantly below its CMC. In the case of L64, the slope clearly shifts at around 0.01 g/L. This phenomenon has previously been observed and attributed to the formation of unimer micelles or structural change of surfactants at the interface.[14, 15, 29] However, theoretical and experimental studies using neutron reflectivity measurements indicated that the effect of copolymer depletion below the concentration, which is due to adsorption of the copolymer to the air−water interface or container surfaces, causes in this change in the slope.[25, 26] Therefore, in this study, the concentration region below reported CMC values, but above the concentration where polymer depletion clearly completed was used to calculate $A$ using equations (1) and (2).

Furthermore, possible contribution on the enhanced surface activity due to the elimination of hydrophilic chain-end groups was contemplated for several Pluronic polymers (L35, L64, 10R5, and 17R4) through methylation of the chain ends. Akin to the results for the PEG homopolymers, elimination of chain-end hydroxyl groups via methylation did not induce a significant effect on surface tension for L64 and 17R4, while dimethylation of the polymers with smaller molecular weights (L35 and 10R5) displayed

significantly reduced $\gamma$. Interestingly, these methoxy-terminated linear species displayed the largest $A$ within the same series of the Pluronic surfactants. From model calculations, the PPG segments of Pluronic surfactants are expected to be positioned at the air–water interface with little penetration into the water, while the PEG segments are extended into the water phase.[26] Methylation of the chain ends may induce the migration of the PEG segments towards the air–water interface for the ABA-type surfactants, and a stronger fixture of the PPG segments at the interface for the BAB-type surfactants, both due to an increase in hydrophobicity, thus resulting in larger $A$. Moreover, the elimination of the chain-end hydroxy groups enhanced surface activity for Pluronic surfactants of smaller molecular weights such as L35 and 10R5 (Figures 2-1, 2-4b, and 2-4f). On the other hand, the chain-end effect on surfactants with larger molecular weight such as L64 and 17R4 were minimal because of the smaller contribution from the chain ends (Figures 2-1, 2-4c, and 2-4g). Therefore, while the chain-end modification would only prove to be an effective strategy for improvement of the interfacial activity for relatively small surfactants, the present topology-based approach through cyclization is not restricted by the molecular weight.

## 2.4. CONCLUSIONS

Cyclized Pluronic surfactants having various molecular weights and segment ratios were synthesized by etherification or acetalization, and the surface activity was studied. The surface activity of the cyclized PEG homopolymer enhanced with a drastic decrease in $A$ at the air–water interface from 410 Å$^2$ (***l*-PEG(OH)**) to 100 Å$^2$ (***c*-PEG**). Similarly, the surface activity of cyclic Pluronic surfactants was improved through the decrease in $A$. Moreover, the degree of a decrease in $\gamma$ positively correlated with the PEG composition. While the influence of the chain ends on the interfacial property was limited to surfactants with relatively small molecular weights, the cyclization was found to be effective for all the surfactants studied.

The present work describes further topology effects of PEG and Pluronic surfactants. Considering that PEG and Pluronic surfactants are ones of the most commonly used commercial products coupled with the fact that cyclization does not involve a chemical transformation in the main chain, the utilization of the polymer topology for the improvement of the surfactant properties would find various applications and provide new insights into polymer chemistry of aqueous solutions.

## 2.5. REFERENCES

(1) Tomalia, D. A.; Frechet, J. M. J. Discovery of dendrimers and dendritic polymers: A brief historical perspective. *J. Polym. Sci., Part A: Polym. Chem.* **2002**, *40* (16), 2719-2728. DOI: 10.1002/pola.10301.

(2) *Topological Polymer Chemistry: Progress of Cyclic Polymers in Syntheses, Properties and Functions*; World Scientific, 2013.

(3) Tezuka, Y. Topological Polymer Chemistry Designing Complex Macromolecular Graph Constructions. *Acc. Chem. Res.* **2017**, *50* (11), 2661-2672. DOI: 10.1021/acs.accounts.7b00338.

(4) Edwards, J. P.; Wolf, W. J.; Grubbs, R. H. The synthesis of cyclic polymers by olefin metathesis: Achievements and challenges. *J. Polym. Sci., Part A: Polym. Chem.* **2019**, *57* (3), 228-242. DOI: 10.1002/pola.29253.

(5) Haque, F. M.; Grayson, S. M. The synthesis, properties and potential applications of cyclic polymers. *Nat. Chem.* **2020**. DOI: 10.1038/s41557-020-0440-5.

(6) Semlyen, J. A. Cyclic Polymers. 2nd ed.; Kluwer Academic Publishers: New York, 2002.

(7) Seeman, N. C. DNA in a material world. *Nature* **2003**, *421* (6921), 427-431. DOI: 10.1038/nature01406.

(8) Kates, M. Membrane lipids of archaea. In *The Biochemistry of Archaea (Archaebacteria)*, Kates, M., Kushner, D. J., Matheson, A. T. Eds.; Elsevier, 1993; pp 261-295.

(9) Honda, S.; Yamamoto, T.; Tezuka, Y. Topology-directed control on thermal stability: Micelles formed from linear and cyclized amphiphilic block copolymers. *J. Am. Chem. Soc.* **2010**, *132* (30), 10251-10253. DOI: 10.1021/ja104691j.

(10) Honda, S.; Yamamoto, T.; Tezuka, Y. Tuneable enhancement of the salt and thermal stability of polymeric micelles by cyclized amphiphiles. *Nat. Commun.* **2013**, *4*, 1574. DOI: 10.1038/ncomms2585.

(11) Wada, H.; Kitazawa, Y.; Kuroki, S.; Tezuka, Y.; Yamamoto, T. NMR Relaxometry for the Thermal Stability and Phase Transition Mechanism of Flower-like Micelles from Linear and Cyclic Amphiphilic Block Copolymers. *Langmuir* **2015**, *31* (32), 8739-8744. DOI: 10.1021/acs.langmuir.5b01902.

(12) Wang, Y.; Quinsaat, J. E. Q.; Ono, T.; Maeki, M.; Tokeshi, M.; Isono, T.; Tajima, K.; Satoh, T.; Sato, S.; Miura, Y.; et al. Enhanced dispersion stability of gold nanoparticlesby the physisorption of cyclic poly(ethylene glycol). *Nat. Commun.* **2020**, *11*, 6089.

(13) Schmolka, I. R. ARTIFICIAL SKIN .1. PREPARATION AND PROPERTIES OF PLURONIC F-127 GELS FOR TREATMENT OF BURNS. *J. Biomed. Mater. Res.* **1972**, *6* (6), 571-582. DOI: 10.1002/jbm.820060609.

(14) Prasad, K. N.; Luong, T. T.; Florence, A. T.; Paris, J.; Vaution, C.; Seiller, M.; Puisieux, F. SURFACE-ACTIVITY AND ASSOCIATION OF ABA POLYOXYETHYLENE-POLYOXYPROPYLENE BLOCK COPOLYMERS IN AQUEOUS-SOLUTION. *J. Colloid Interface Sci.* **1979**, *69* (2), 225-232. DOI: 10.1016/0021-9797(79)90151-6.

(15) Alexandridis, P.; Athanassiou, V.; Fukuda, S.; Hatton, T. A. SURFACE-ACTIVITY OF POLY(ETHYLENE OXIDE)-BLOCK-POLY(PROPYLENE OXIDE)-BLOCK-POLY(ETHYLENE OXIDE) COPOLYMERS. *Langmuir* **1994**, *10* (8), 2604-2612, Article. DOI: 10.1021/la00020a019.

(16) Yu, G.-E.; Deng, Y.; Dalton, S.; Wang, Q.-G.; Attwood, D.; Price, C.; Booth, C. MICELLIZATION AND GELATION OF TRIBLOCK COPOLY(OXYETHYLENE OXYPROPYLENE OXYETHYLENE), F127. *J. Chem. Soc. Faraday Trans.* **1992**, *88* (17), 2537-2544. DOI: 10.1039/ft9928802537.

(17) Yang, Z.; Pickard, S.; Deng, N. J.; Barlow, R. J.; Attwood, D.; Booth, C. Effect of block structure on the micellization and gelation of aqueous solutions of copolymers of

ethylene oxide and butylene oxide. *Macromolecules* **1994**, *27* (9), 2371-2379. DOI: 10.1021/ma00087a002.

(18) Varade, D.; Sharma, R.; Aswal, V. K.; Goyal, P. S.; Bahadur, P. Effect of hydrotropes on the solution behavior of PEO/PPO/PEO block copolymer L62 in aqueous solutions. *Eur. Polym. J.* **2004**, *40* (11), 2457-2464, Article. DOI: 10.1016/j.eurpolymj.2004.06.022.

(19) Yu, G.-E.; Garrett, C. A.; Mai, S. M.; Altinok, H.; Attwood, D.; Price, C.; Booth, C. Effect of cyclization on the association behavior of block copolymers in aqueous solution. Comparison of oxyethylene/oxypropylene block copolymers cyclo-P34E104 and E52P34E52. *Langmuir* **1998**, *14* (9), 2278-2285.

(20) *Polymer Handbook*; Wiley-Interscience, 2003.

(21) Cooke, J.; Viras, K.; Yu, G.-E.; Sun, T.; Yonemitsu, T.; Ryan, A. J.; Price, C.; Booth, C. Large cyclic poly(oxyethylene)s: Chain folding in the crystalline state studied by Raman spectroscopy, X-ray scattering, and differential scanning calorimetry. *Macromolecules* **1998**, *31* (9), 3030-3039. DOI: 10.1021/ma9717909.

(22) Vargaftik, N. B.; Volkov, B. N.; Voljak, L. D. INTERNATIONAL TABLES OF THE SURFACE-TENSION OF WATER. *J. Phys. Chem. Ref. Data* **1983**, *12* (3), 817-820. DOI: 10.1063/1.555688.

(23) Kricheldorf, H. R.; Schwarz, G. Cyclic polymers by kinetically controlled step-growth polymerization. *Macromol. Rapid Commun.* **2003**, *24* (5-6), 359-381. DOI: 10.1002/marc.200390063.

(24) Yamamoto, T.; Tezuka, Y. Cyclic polymers revealing topology effects upon self-assemblies, dynamics and responses. *Soft Matter* **2015**, *11* (38), 7458-7468. DOI: 10.1039/c5sm01557j.

(25) Li, P. X.; Li, Z. X.; Shen, H. H.; Thomas, R. K.; Penfold, J.; Lu, J. R. Application of the Gibbs Equation to the Adsorption of Nonionic Surfactants and Polymers at the Air-Water Interface: Comparison with Surface Excesses Determined Directly using Neutron Reflectivity. *Langmuir* **2013**, *29* (30), 9324-9334, Article. DOI: 10.1021/la4018344.

(26) Linse, P.; Hatton, T. A. Mean-field lattice calculations of ethylene oxide and propylene oxide containing homopolymers and triblock copolymers at the air/water interface. *Langmuir* **1997**, *13* (15), 4066-4078, Article. DOI: 10.1021/la9620871.

(27) Griffiths, P. C.; Stilbs, P.; Yu, G. E.; Booth, C. Role of Molecular Architecture in Polymer Diffusion - a Pgse-nmr Study of Linear and Cyclic Poly(Ethylene Oxide). *J. Phys. Chem.* **1995**, *99* (45), 16752-16756, Article. DOI: 10.1021/j100045a041.

(28) Hirose, Y.; Taira, T.; Sakai, K.; Sakai, H.; Endo, A.; Imura, T. Structures and Surface Properties of "Cyclic" Polyoxyethylene Alkyl Ethers: Unusual Behavior of Cyclic

Surfactants in Water. *Langmuir* **2016**, *32* (33), 8374-8382. DOI: 10.1021/acs.langmuir.6b01553.

(29) Saito, Y. Pluronic Surfactants. *Nihon Yukagakkaishi* **2000**, *49*, 1071-1080.

## 2.6. SUPPORTING INFORMATION

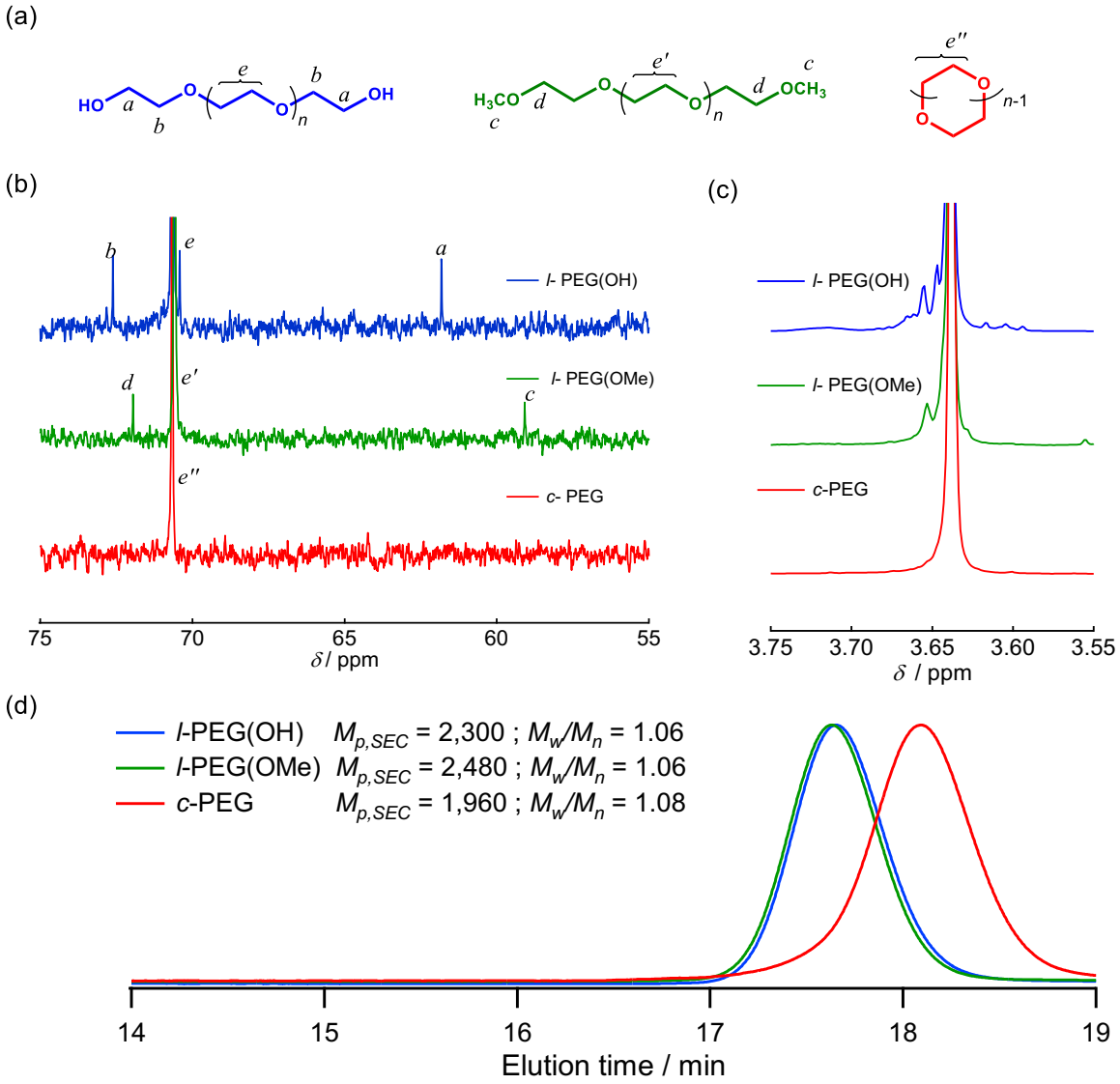


**Figure S2-1.** (a) Chemical structure, (b) $^{13}C$ NMR spectra, (c) $^{1}H$ NMR spectra, and (d) SEC traces of ***l*-PEG(OH)**, ***l*-PEG(OMe)**, and ***c*-PEG**.

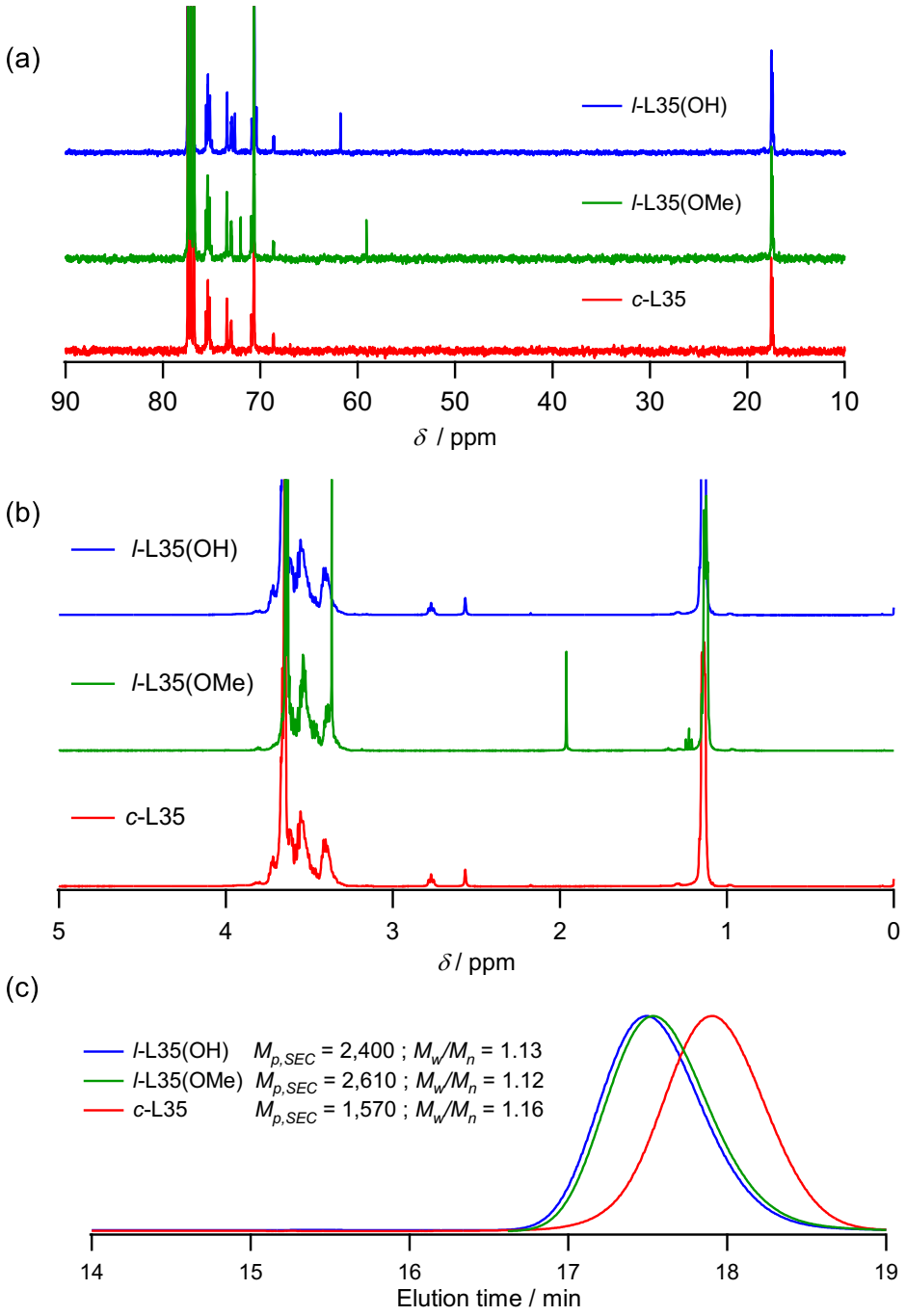


**Figure S2-2.** (a) $^{13}$C NMR spectra, (b) $^{1}$H NMR spectra, and (c) SEC traces of ***l*-L35(OH)**, ***l*-L35(OMe)**, and ***c*-L35**.

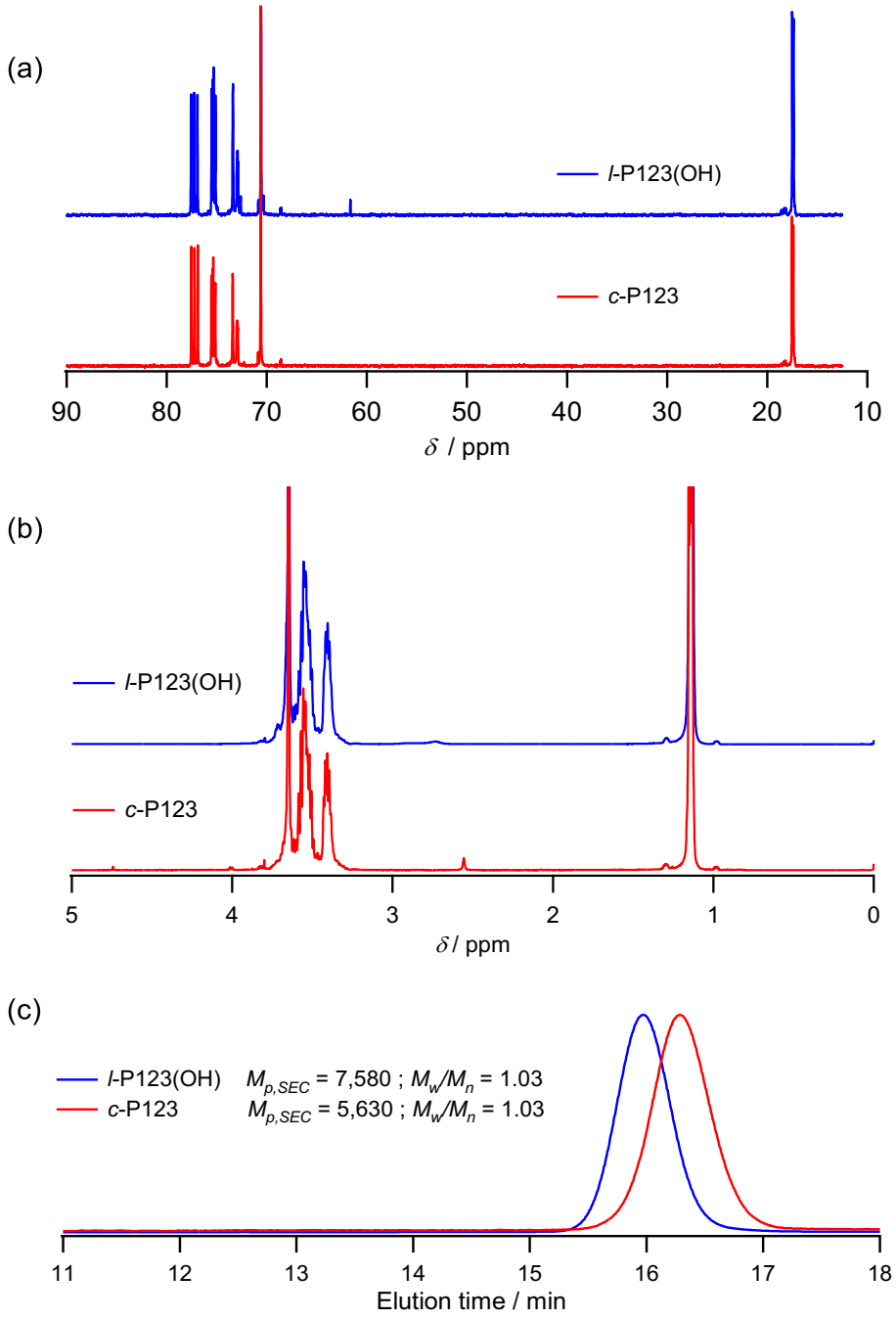


**Figure S2-3.** (a) $^{13}$C NMR spectra, (b) $^{1}$H NMR spectra, and (c) SEC traces of ***l*-P123(OH)** and ***c*-P123**.

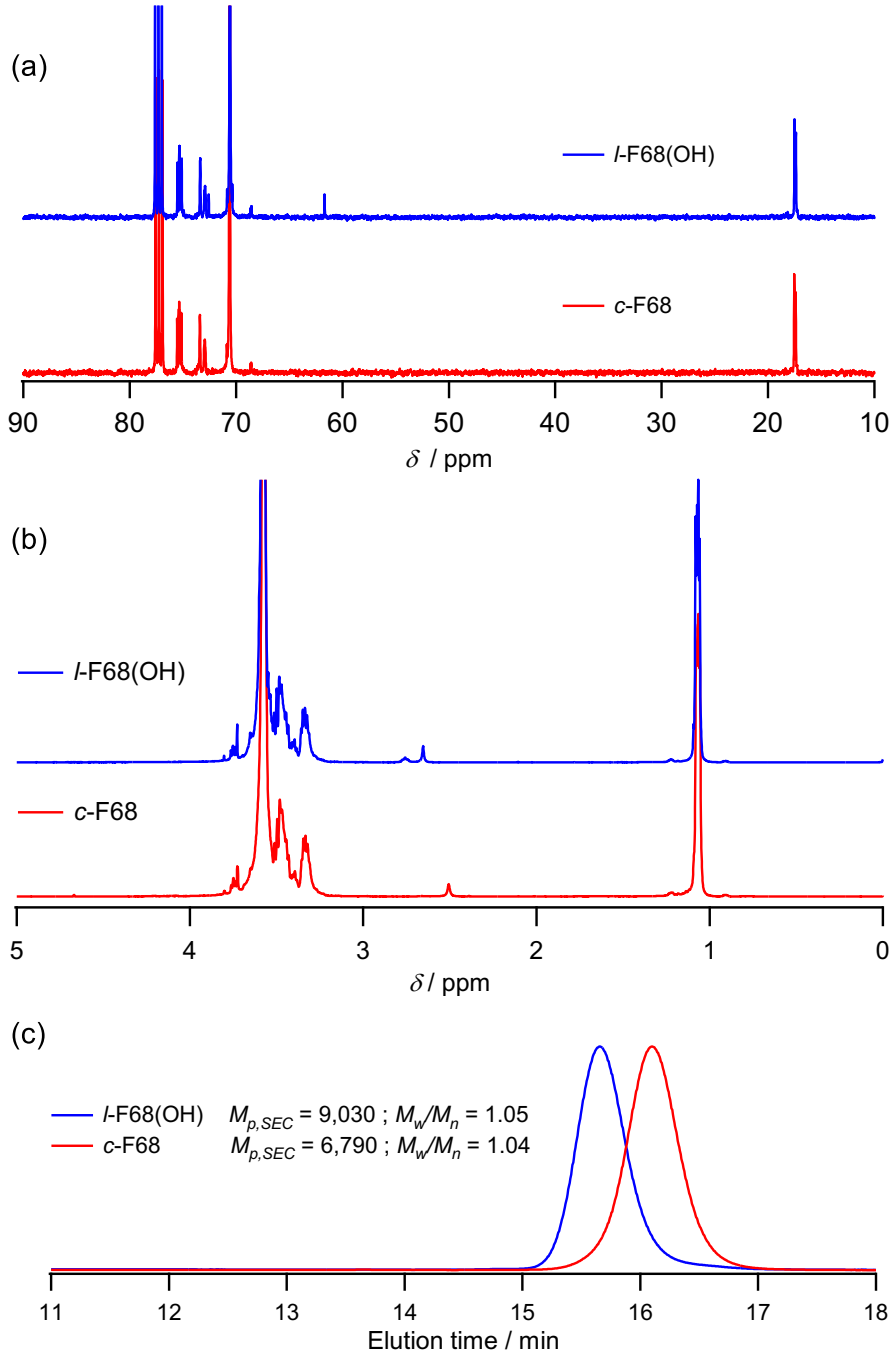


**Figure S2-4.** (a) $^{13}$C NMR spectra, (b) $^{1}$H NMR spectra, and (c) SEC traces of ***l*-F68(OH)** and ***c*-F68**.

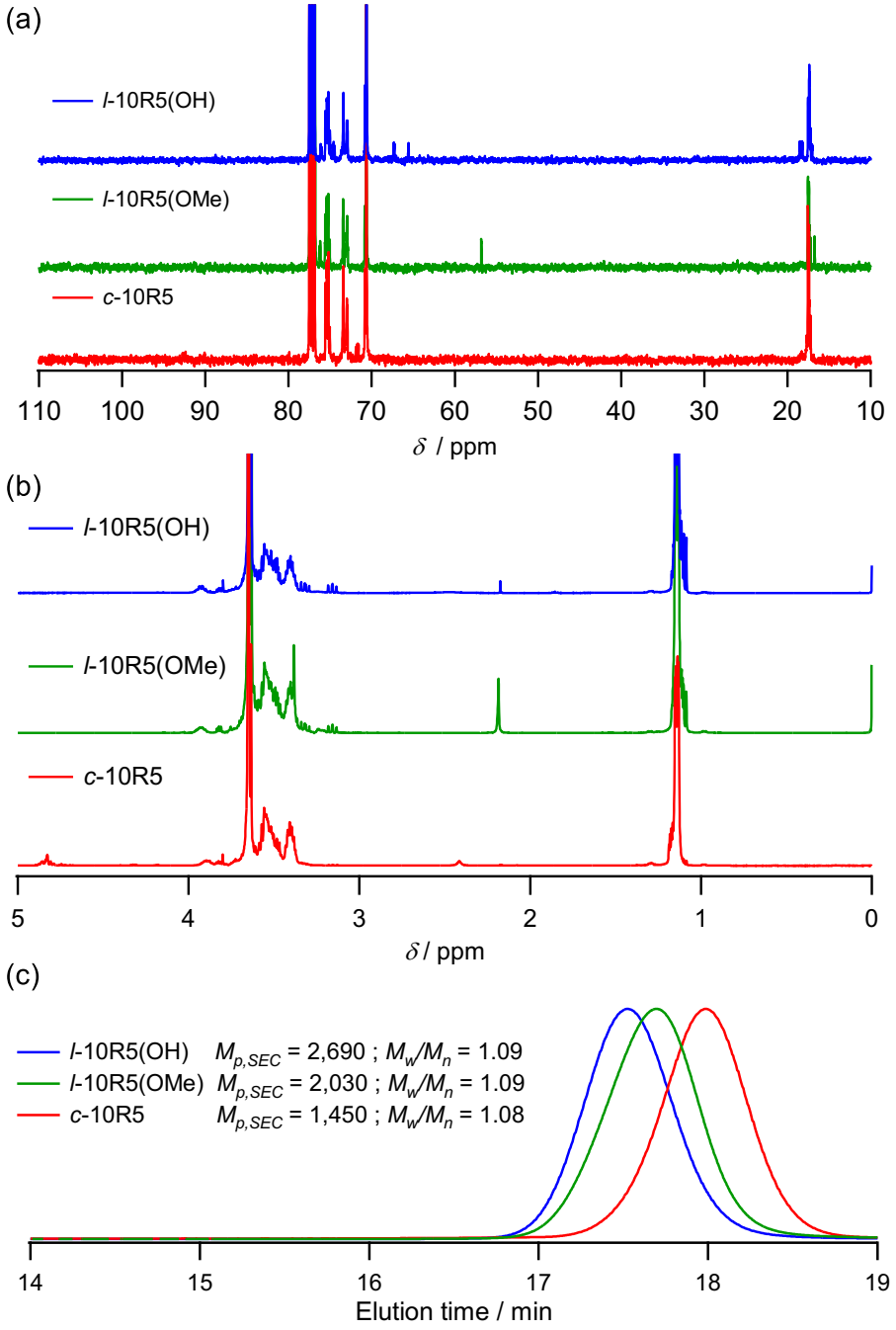


**Figure S2-5.** (a) $^{13}$C NMR spectra, (b) $^{1}$H NMR spectra, and (c) SEC traces of ***l*-10R5(OH)**, ***l*-10R5(OMe)**, and ***c*-10R5**.

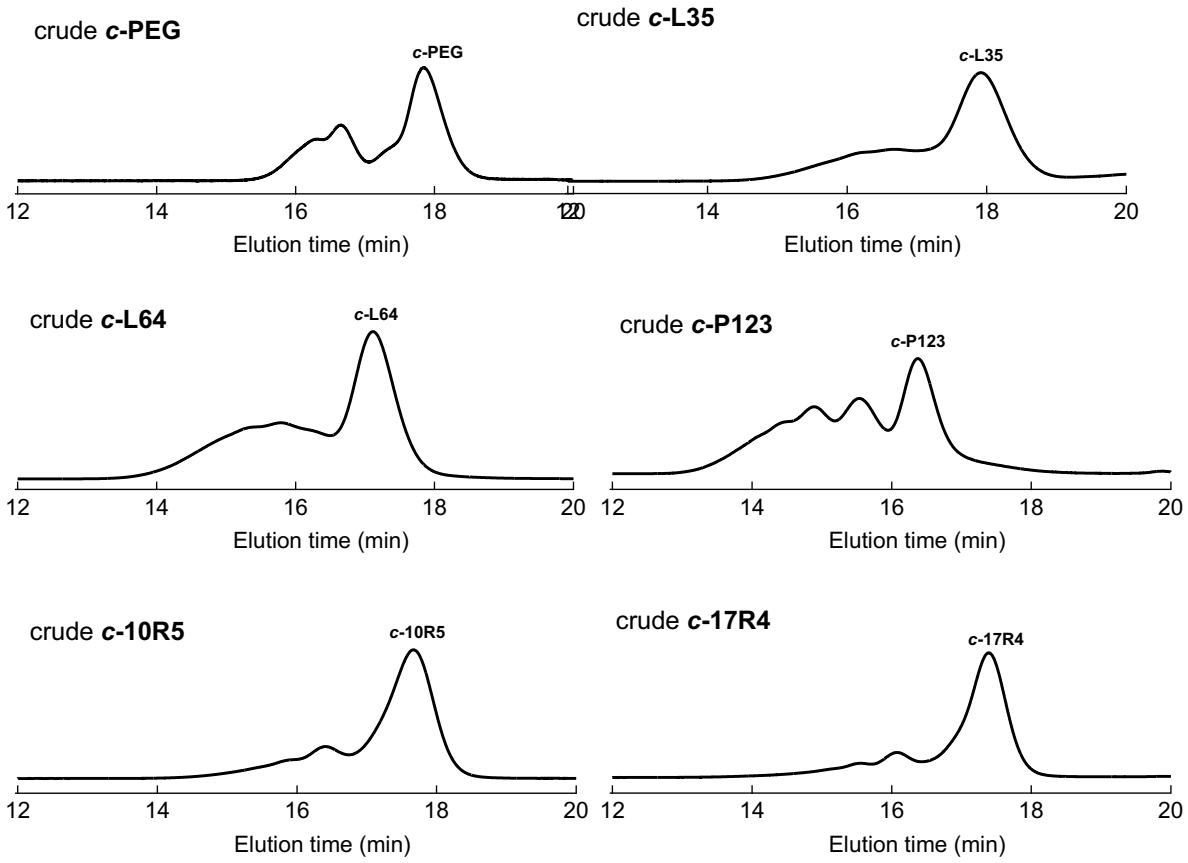


**Figure S2-6.** SEC traces of crude ***c*-PEG**, ***c*-L35**, ***c*-L64**, ***c*-P123**, ***c*-10R5**, and ***c*-17R4**.

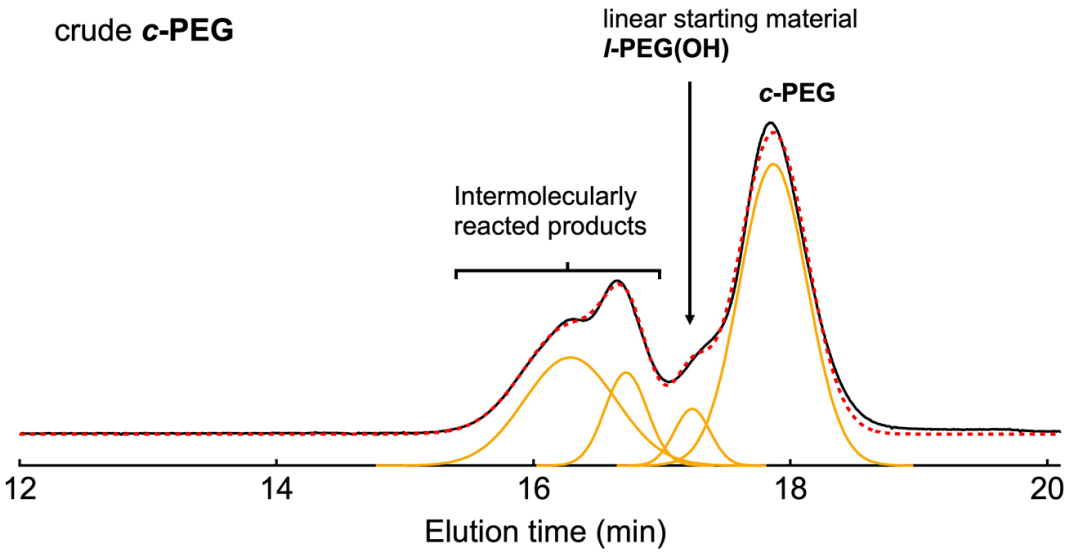


**Figure S2-7.** Deconvolution of the SEC trace of crude ***c*-PEG**. The black solid line represents the actual SEC trace, and the red dotted line denotes the overall fitted curve from the addition of four individual gaussian peaks shown in orange.

# *Chapter 3*

## Topology Effect of Cyclization on the Aggregation Properties of PEG and Pluronic Surfactants in Solution

## 3.1. INTRODUCTION

Investigation into the properties of polymers with non-linear architecture, namely, topological polymers, have revealed various unique structure–property relationships[1]. Amongst them, polymers having cyclic topology have especially been the subject of attention, resulting in extensive reviews[2-4] and application-oriented researches[5-9] emerging in recent years. Naturally, the effect of cyclic topology has been investigated beyond simple homopolymer systems to self-assembling amphiphilic block copolymer systems, where the thermodynamics and structural properties of self-assembly phenomena were found to be affected by the geometrical constraints induced from the ring topology.[10-17] In general, cyclic copolymer amphiphiles were found to assemble micelles with reduced dimensions compared to its corresponding linear counterparts of the same molecular weight.[11-13] Moreover, enhancement in thermal stability and salt stability were found for cyclic diblock copolymer micelles compared to its corresponding linear triblock species, resulting from inhibition of inter-micellar chain-bridging induced agglomeration.[14-16]

The effect of polymer topology is, in theory, not bound by its chemical structure. However, physical properties exhibited by realistic systems are a combination result, with contribution from a number of factors, thus complicating the elucidation of a “pure” topology effect. For this reason, well-studied systems and polymers with a wide understanding of relation between physical properties and polymer parameters such as

molecular weight, block ratio, and block architecture are attractive candidates for investigation into the effect of polymer topology. In this context, typical nonionic surfactants of symmetrical triblock copolymers containing hydrophilic poly(ethylene glycol) (PEG) and hydrophobic poly(propylene glycol) (PPG), commercially registered under trademark names of Pluronic or Poloxamers,[18] are ideal. Pluronic surfactants can be classified into two types based on their block architecture. Pluronic surfactants with PEO–PPO–PEO block architecture are widely known as ABA-type Pluronic, with the hydrophobic PPO block sandwiched between two hydrophilic PEO blocks. In contrast, surfactants with PPO–PEO–PPO architecture are known as "reverse" or BAB-type Pluronic copolymers, consisting of a middle hydrophilic PEO block with two terminal hydrophobic PPO blocks. In general, attention has been focused on property–structure relationships regarding parameters such as molecular weight and block ratios,[19-22] and less on the block architecture.[23, 24]

Until date, a number of methods have been employed to probe structural characteristics of the aggregation behaviour of Pluronic copolymers, the most popular of them being dynamic light scattering (DLS), UV–vis absorption/fluorescence spectroscopy, and viscosity measurements.[25] Through combination of various characterization methods as mentioned, a relatively complete analysis of micellization properties of Pluronic surfactants can be expected.

Physical properties of cyclized counterparts of a relatively large Pluronic copolymer $EO_{52}$–$PO_{34}$–$EO_{52}$, studied by Booth and coworkers, is one of the first reports on cyclic AB-type diblock copolymers, with results indicating a relatively weak effect of cyclization upon its micellization thermodynamics, with also some limited insight into its micellar structure.[26] More recently, the author reported the synthesis and interfacial properties for cyclized Pluronic surfactants of diverse chemical composition, revealing an enhancement in interfacial activity via cyclization to be a prevalent phenomenon. Interestingly, the degree of enhancement in interfacial activity upon cyclization was found to be influenced by the block ratios and architecture of polymer species.[27] It is, therefore, of importance to revisit the seminal work of Booth et al, and elucidate the effect of cyclic topology on Pluronic copolymers in relation to its other chemical parameters, using the wide range of techniques available today.

This work presents a comprehensive investigation into the effect of cyclic topology on the thermodynamic and structural properties of Pluronic L35, L64, 10R5 and 17R4 micellization phenomena. Through comparison of cyclic species against its corresponding linear counterparts for the four copolymer species, a detailed effect of cyclization was observed in micellization thermodynamic parameters and micelle structural parameters, including its thermal stability. The temperature-induced phase separation phenomena for PEG homopolymer in 0.5 M $K_2SO_4$ solutions were also probed as a reference point to discuss the effect of topology in various phases.

## 3.2. EXPERIMENTAL SECTION

### 3.2.1. Materials.

4-Toluenesulfonyl chloride (TsCl) (>98.0%, Junsei Chemical Co., Ltd.), iodomethane (>99.5%, Kanto Chemical Co., Inc.), sodium chloride (NaCl) (>99.0%, Kanto Chemical Co., Inc.), potassium hydroxide (KOH) (>85.5%, Kanto Chemical Co., Inc.), sodium sulfate ($Na_2SO_4$) (>99.0%, Kanto Chemical Co., Inc.), *n*-heptane (>99.0%, Kanto Chemical Co., Inc.), chlorobenzene (>99.0% Nacalai Tesque, Inc.), methanol (MeOH) (>99.5%, Kanto Chemical Co., Inc.), dichloromethane ($CH_2Cl_2$) (>99.0%, Kanto Chemical Co., Inc.) for the work up, and chloroform ($CHCl_3$) (>99.0%, Kanto Chemical Co., Inc.) were used as received. Tetrahydrofuran (THF), dehydrated stabilizer free (>99.5%, Kanto Chemical Co., Inc.) and dehydrated dichloromethane ($CH_2Cl_2$) (>99.5%, Kanto Chemical Co., Inc.) for the reaction were purified by a solvent purification system (MBRAUN MB-SPS-Compact). Silver behenate (>95.0%, Tokyo Chemical Industry Co., Inc.) was used as a calibrant for SAXS measurements. Pluronic L35 (PEG–PPG–PEG), average $M_n$ ~1900, PEG weight ratio 50 wt% (Sigma–Aldrich), Pluronic L64 (PEG–PPG–PEG), $M_n$ ~2900, PEG weight ratio 40 wt% (Sigma–Aldrich), Pluronic 10R5 (PPG–PEG–PPG), average $M_n$ ~1700, PEG weight ratio 50 wt% (Sigma–Aldrich), and Pluronic 17R4 (PPG–PEG–PPG), average $M_n$ ~2700, PEG weight ratio 40 wt% (Sigma–Aldrich) were purified by recycling preparative SEC. Polyethylene glycol ($M_n$ ~2000, 4600, 10000, 20000 Aldrich) having terminal hydroxy groups were purified

using preparative LCCC and reprecipitated in diethylether and lyophilized in benzene before use.

Pluronic L64 was further purified by a previously reported method,[25, 28] by vigorously stirring 1 g of the copolymer in 100 mL of distilled hexane at room temperature for 15 min, followed by removal of the separated hexane phase. This procedure was repeated three times after which the copolymer was dried under reduced pressure overnight to extract residual hexane.

### 3.2.2. Preparative SEC

A Japan Analytical Industry LC-908 recycling preparative HPLC system (Hitachi L-7110 pump and JAI RI detector RI-5) was used. JAIGEL-2H and 3H columns and a pre-column were connected in series. $CHCl_3$ was used as the solvent, and the flow rate was set at 3.5 mL/min.

### 3.2.3. Pluronic solution preparation

Copolymer solutions with different concentrations were prepared by weighing required amounts copolymer and dissolving in Milli-Q water, which were stirred at room temperature for over 12 hours. The samples were further kept inside a refrigerator in tightly closed glass vials for over 48 hours before being filtered through a 0.45 μm Millipore filter prior to measurement.

### 3.2.4. PEG solution preparation

PEG in 0.5 M $K_2SO_4$ aqueous solutions with different concentrations were prepared by weighing required amounts copolymer and dissolving in 0.5 M $K_2SO_4$ aqueous solutions, which were stirred at room temperature for over 12 hours. The samples were further kept inside a refrigerator in tightly closed glass vials for over 48 hours before being filtered through a 0.45 μm Millipore filter prior to measurement.

### 3.2.5. CMT by dye solubilization

Aqueous solutions of Pluronic surfactants in the presence of DPH were prepared through a dye solubilization technique.[29] First, Pluronic surfactants were dissolved in Milli-Q water and stirred at room temperature for over 12 h. 25 μL of DPH/methanol solution taken from a stock solution of 0.4 mM DPH in methanol was added to 2.5 mL of the copolymer aqueous solution. The final sample solution contained 1 % (v/v) methanol and 4.0 μM DPH, at four polymer concentrations ($c$) of 0.30, 1.0, 3.0, and 10 g/L. The sample solutions were left in the dark to equilibrate for at least 3 h prior to measurement. Each sample solution was heated at a rate of 0.1 °C $min^{-1}$, and absorption spectrum (340 – 400 nm) was measured in 2 ºC increments after an equilibration time of 10 min at each temperature.

### 3.2.6. Cloud point measurement

Transmission of the solution (%T) was measured at 595 nm on a JASCO V-670 UV-Visible spectrophotometer in deionized water using a micro quartz cell (M25-UV-2, GL Science Inc. Japan). Aqueous solutions of Pluronic surfactants and PEG were stirred at 60 rpm inside the spectrophotometer, and heated at a rate of 1 ºC $min^{-1}$. Transmission was measured in 1 ºC increments. The lowest temperature at which %T at 595 nm became 90 % or less was determined as the cloud point ($T_c$).

### 3.2.7. Dynamic light scattering (DLS)

DLS measurements were performed on a Malvern Zetasizer Nano spectrometer equipped with a Nd:YAG laser ($\lambda$ = 532 nm). The light scattering signal was obtained at a fixed angle of 173º. Particle diameter distribution changes of aqueous solutions of Pluronic surfactants (1.0 wt%) were measured at various temperatures after an equilibration time of 10 min.

## 3.3. RESULTS AND DISCUSSION

### 3.3.1. Solution preparation

Cyclic Pluronic surfactants L35, L64, 10R5 and 17R4 were synthesized and purified according to a reported method (chapter 2),[26, 27, 30] through intramolecular cyclization of a linear prepolymer. For PEG–PPG–PEG (ABA) type Pluronic L35 and L64, Williamson-ether synthesis was undertaken for the reaction of chain-end hydroxy groups, while for PPG–PEG–PPG (BAB) type Pluronic 10R5 and 17R4, an acetalization reaction was carried out instead, due to reduced reactivity of the secondary hydroxy chain-end groups. Chain-end methylated linear polymers were also prepared according to the reported method in chapter 2, in order to clarify the extent of effect of polymer topology from chemically induced changes due to elimination of chain-end hydroxy groups.

In the case of L64, the commercial product (linear prepolymer) is known to contain some amount of polymeric impurity of a more hydrophobic nature. This polymeric impurity is known to substantially affect its solution properties close to micellization conditions, with a number of methods reporting its removal.[25, 28] In our case, repeated washing of the prepolymer using hexane successfully purified the prepolymer, as confirmed through temperature-dependent transmission of the polymer solution (Figure 3-1). A previously observed spike in transmission around 40 ºC from the aggregation of impurities clearly disappeared for solutions prepared from purified L64. Cyclization and

methylation reaction were both carried out using the purified copolymer. No such anomalous behaviour was found for L35, 10R5 and 17R4 solutions, thus, the material was used for synthesis without further purification.

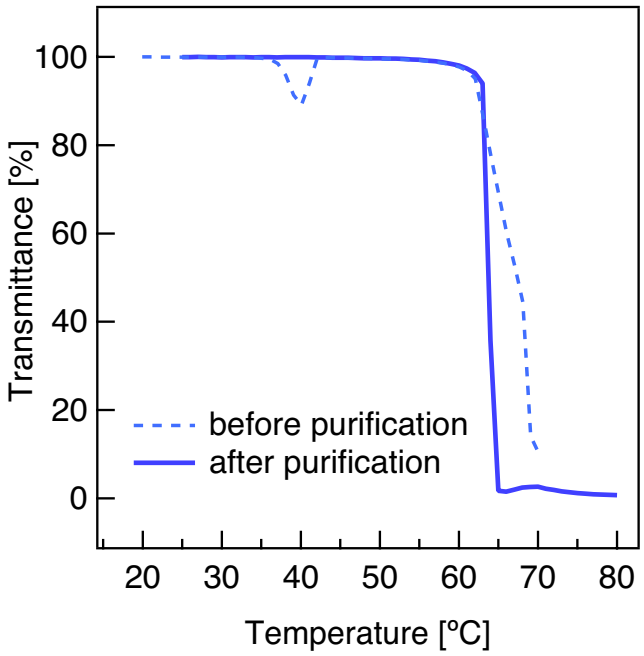


**Figure 3-1.** Temperature-dependent transmission changes at 595 nm for 1 wt% *l*-L64(OH) solution purified through hexane washing.

Aqueous copolymer solutions for linear Pluronic surfactants with either hydroxy chain-ends or methoxy chain-ends, along with its cyclic counterparts, were prepared by dissolving appropriate amounts of the copolymer in Milli-Q water. The copolymer solutions were stirred over 12 h at room temperature, after which were kept in a refrigerator for over 48 h for complete dissolution. Each solution was filtered immediately prior to each measurement to remove any macroscopic impurities.

Among the various types of Pluronic surfactants commercially available, Pluronic L35, L64, 10R5 and 17R4 were selected since their total molecular weight and block composition realize aggregation behaviour at mild conditions, deeming them suitable for biological applications. In addition, a copious amount of research has been conducted for L64, revealing detailed aspects of its aggregation behaviour.[25, 31-35] Thus, this polymer was considered a reasonable candidate to explore the topology effect of cyclization. BAB-type copolymers (10R5 and 17R4) on the other hand, has not received the same extensive attention as compared to L35 and L64 with relatively fewer reports on its physical properties.[36, 37] The relation between ABA-type and BAB-type Pluronics mainly lies in the difference of block architecture, in which the former is a hydrophilic–hydrophobic–hydrophilic triblock copolymer while the latter is a hydrophobic–hydrophilic–hydrophobic triblock copolymer. Despite almost identical molecular weight and hydrophilic/hydrophobic block ratios, the block architectural distinction between the two causes contrasting solution properties, mainly attributed to the entropic disparity required

upon conformational changes of the polymer under micellization conditions.[24] With the importance of block architecture in mind, the ABA-type or BAB-type triblock architecture is both converted into an AB-type diblock architecture upon cyclization, Therefore, comparison of the changes in solution properties between ABA-type and BAB-type Pluronic copolymers of similar compositions allows a clarified understanding of the effect of cyclization, in relation to the block sequence.

### 3.3.2. CMT by dye solubilization

In order to evaluate the thermal response behaviour of the synthesized cyclic Pluronic surfactants, critical micelle temperature (CMT) measurements through a hydrophobic dye solubilization technique, using 1,6-diphenyl-1,3,5-hexatriene (DPH) were performed.[29] The CMT values ($T_{CMT}$) were obtained from the intersection temperature value at which a change in the slope of absorption intensity of DPH ($\lambda_{max,\ DPH}$ = 356 nm) was observed, indicating the dye solubilization within the hydrophobic micelle interior (Figure 3-2).

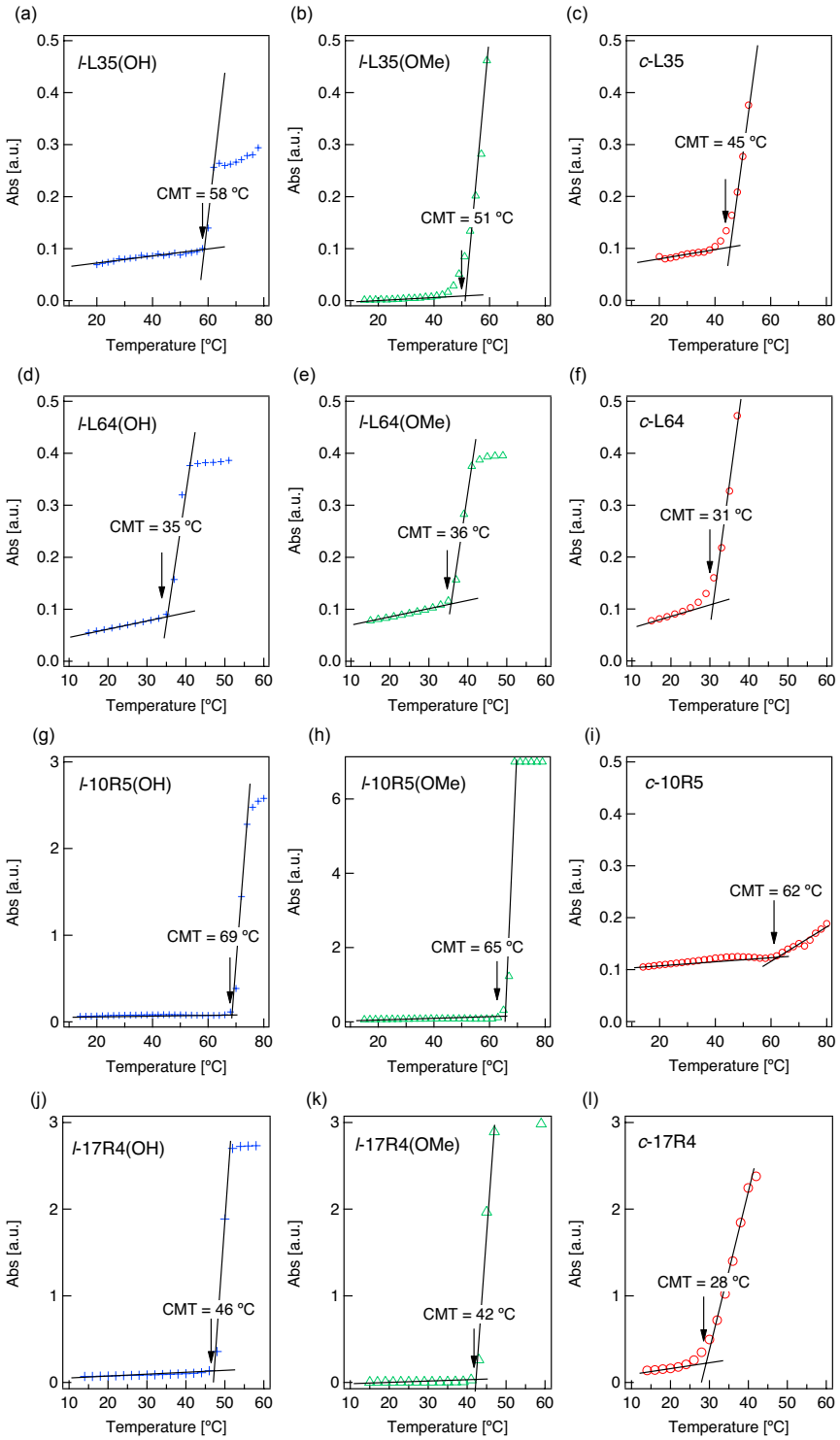


**Figure 3-2.** Temperature-dependent absorption intensity of DPH ($\lambda_{max,\ DPH}$ = 356 nm) for 10 g/L solutions of (a) ***l*-L35(OH)**, (b) ***l*-L35(OMe)** and (c) ***c*-L35**. Those of L64, 10R5, and 17R4 are also shown in (d)–(l). Critical micellization temperature ($T_{CMT}$) was determined as the intersection temperature where an increase in the slope of the absorption intensity was observed.

Furthermore, the enthalpy of micellization ($\Delta H_{mic}$) was calculated from the slope of the linear fit of the ln($c$) versus $1/T_{CMT}$ values obtained at four polymer molar concentrations ($c$) (Figure 3-3). Using the $\Delta H_{mic}$ values, $\Delta G_{mic}$ at $c$ = 1 wt% and at $T_{CMT}$ as well as $\Delta S_{mic}$ were calculated using the following equations:

$$\Delta H_{mic} = R[\, \partial \ln (c) / \partial (1/T_{CMT})] \quad (1)$$

$$\Delta G_{mic} = RT \ln (X) \quad (2)$$

$$\Delta S_{mic} = (\Delta H_{mic} - \Delta G_{mic}) / T \quad (3)$$

where $X$ is the copolymer concentration in mole fraction units at the micellization condition.

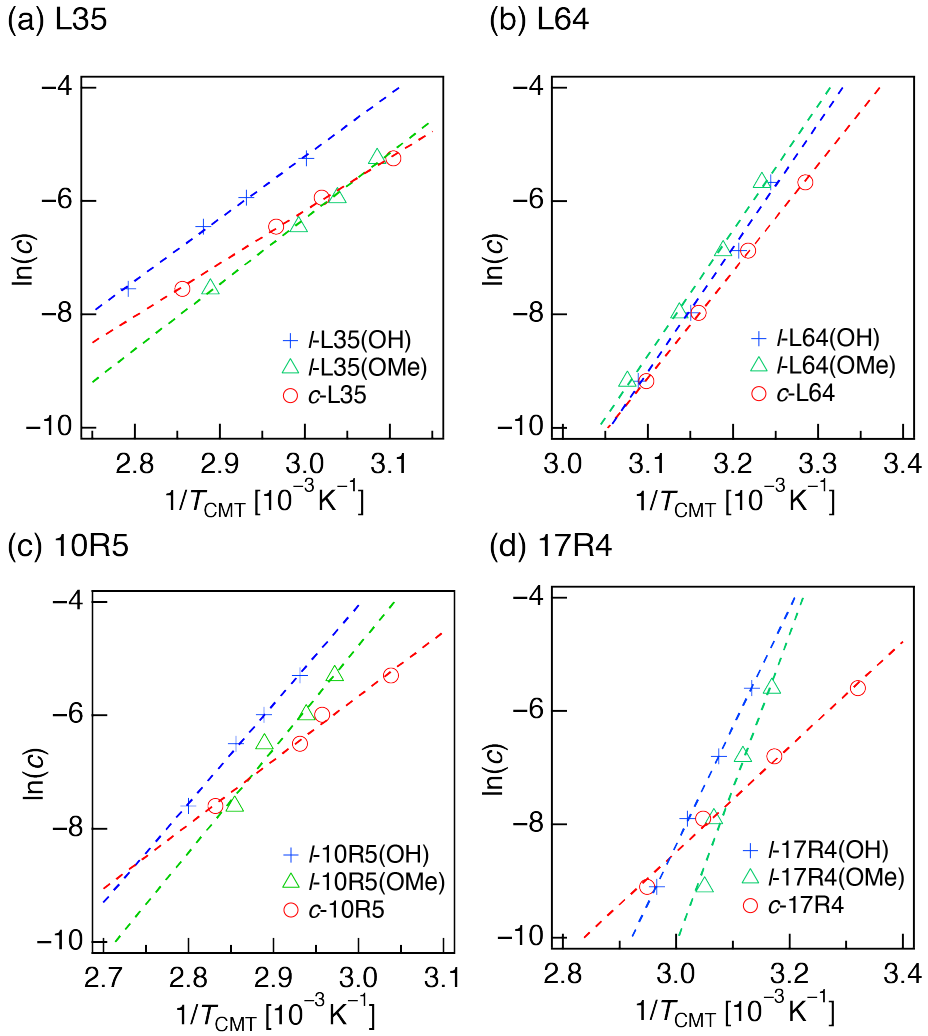


**Figure 3-3.** (a) ln($c$) vs. $1/T_{CMT}$ plot for aqueous solutions of linear hydroxy-terminated (blue), methoxy-terminated (green), and cyclized (red) L35, indicated as ***l*-L35(OH)**, ***l*-L35(OMe)** and ***c*-L35**, respectively. Those of **(b)** L64, **(c)** 10R5, and **(d)** 17R4 are also shown. Enthalpy of micellization ($\Delta H_{mic}$) was calculated from the slope of the linear fitting of the plots.

For 10 g/L ABA-type copolymer solutions, $T_{CMT}$ of ***l*-L35(OH)** was 58 °C, and that of ***c*-L35** decreased to 45 °C. The same trend was observed for L64, where cyclized species displayed comparably lower $T_{CMT}$ than its corresponding linear counterpart with hydroxy chain-end groups (***l*-L64(OH)**, 35 °C; ***c*-L64**, 31 °C in Table 3-1). Methylation of the chain ends also resulted in lowered $T_{CMT}$ for L35, but no significant effect was observed for L64 (***l*-L35(OMe)**, 51 °C; ***l*-L64(OMe)**, 36 °C in Table 3-1). The difference in the critical micellization condition between cyclized and linear ABA-type Pluronic was rather pronounced in comparison to the report by Booth and coworkers, where they were unable to define a clear effect of cyclization on their critical micellization concentrations for both PEG–PPG–PEG and PEG–polybutylene glycol–PEG triblock copolymers.[26, 38] A similar decrease in $T_{CMT}$ was observed for the BAB-type copolymers; from 69 to 62 °C for 10R5 and from 46 to 28 °C for 17R4 upon cyclization. $T_{CMT}$ of 10R5 and 17R4 also decreased upon methylation of the chain ends (***l*-10R5(OMe)**, 65 °C; ***l*-17R4(OMe)**, 42 °C in Table 1), suggesting the elimination of terminal hydroxy groups of PPG to also lower their $T_{CMT}$. In any case, the cyclized copolymers displayed the lowest $T_{CMT}$, indicating the effect of topology to be more significant compared to the consequence of the simple elimination of hydrophilic terminal moieties.

When $\Delta H_{mic}$ values were determined from the slope of the ln ($c$) versus 1 / $T_{CMT}$ plot, smaller values were found for the cyclic species, suggesting less enthalpic inhibition against micellization. According to the previous reports, smaller $\Delta H_{mic}$ values for cyclized

ABA-type amphiphiles arise from the reduced exposure of the hydrophobic B segment to water in the unimer state.[26, 38] Thus, the hydrophilic A segment in the cyclized form likely more effectively shielded the hydrophobic B segment from contact with water. Furthermore, when the ABA-type and BAB-type Pluronics were compared, a more significant effect upon $\Delta H_{mic}$ was observed for the latter. This was likely caused by the hydrophobic chain length to double upon cyclization for the BAB-type copolymers, where the $\Delta H_{mic}$ value per hydrophobic repeating unit is known to be smaller as the segment become longer due to the formation of tight coils, minimizing contact with water.[39]

Similarly, smaller values for the entropy of micellization ($\Delta S_{mic}$) were found for the cyclized species. This can also be attributed to the effect of the cyclic topology on the conformations in the unimer state, and its relation to the hydrophobic effect. The hydrophobic effect is an entropic driving force towards micellization, arising from the release of water molecules from the lowered entropic states due to contact with the hydrophobic segments of the amphiphiles in the unimeric state[40]. This entropically driven process is known to be responsible for the micellization of many amphiphilic molecules including Pluronic copolymers[24], and the positive $\Delta H_{mic}$ and $\Delta S_{mic}$ values obtained for the copolymers in this work also indicate micellization of the linear and cyclized Pluronic to be entropically driven. However, as mentioned above, cyclization of the copolymers leading to an efficient shielding of the hydrophobic PPG blocks from the surrounding

water environment is also expected to reduce the hydrophobic effect, thus, resulting in lowered $\Delta S_{mic}$. In addition, the presence of "dangling chains" in less structured micelles of the BAB-type Pluronic copolymers may contribute to the more drastic decrease in $\Delta S_{mic}$ upon cyclization (eg., ***l*-10R5(OH)**, 505 J/mol K; ***c*-10R5**, 365 J/mol K) compared to the ABA-type copolymers (eg., ***l*-L35(OH)**, 352 J/mol K; ***c*-L35**, 319 J/mol K)[17]. Monte Carlo simulations of the micellization of linear ABA- and BAB-type copolymers performed by Kim and Jo revealed the latter copolymers to possess larger $\Delta S_{mic}$ due to its less structured micelles and dangling chains[41, 42]. Therefore, since cyclization of both ABA- and BAB-type copolymers result in an AB-type diblock copolymer, the $\Delta S_{mic}$ differences can rationally be expected to be more prominent for the copolymers with the BAB-type block sequence.

Interestingly, while the ABA-type Pluronic copolymers displayed comparable $\Delta H_{mic}$ and $\Delta S_{mic}$ values for the linear methoxy-terminated species to that of the linear hydroxy-terminated species, an evident increase in both thermodynamic parameter values were found for 17R4, a copolymer with BAB-type sequence and relatively long PPG blocks. This was indicative of a more significant influence of the hydroxy groups for sufficiently long hydrophobic PPG segments on the micellization phenomena, compared to the hydroxy groups of the hydrophilic PEG segments or short PPG segments. The larger $\Delta S_{mic}$ values for the methylated species are hypothesized to result from the stronger hydrophobicity, and the larger $\Delta H_{mic}$ values may be possibly resulted from relatively

reduced hydrogen bonding interaction within the micelle core. Thus, the fraction of water known to be contained within the Pluronic micelle core[43, 44] may have decreased by methylation of the chain-ends due to its stronger hydrophobic nature, resulting in a larger number of hydrogen bonding severance and a larger enthalpic change upon micelle formation.

**Table 3-1.** Properties of Hydroxy- and Methoxy-Terminated Linear and Cyclized Pluronic Copolymers and Their Solutions' Thermodynamic Parameters

| ***Topology*-Pluronic(chain-end)** | **Composition** | $M_n$ **(g/mol)** | $T_{CMT}$ **at 10 g/L (°C)** | $\Delta H_{mic}$ **(kJ/mol)** [a] | $\Delta G_{mic}$ **(kJ/mol)** [b] | $\Delta S_{mic}$ **(J/(mol K))** [b] | $T_c$ **at 10 g/L (°C)** |
|---|---|---|---|---|---|---|---|
| ***l*-L35(OH)** | $(EG)_{11}$–$(PG)_{16}$–$(EG)_{11}$ | 1,900 | 58 | 91 ± 4 | –26.1 | 352 | 82 |
| ***l*-L35(OMe)** | | | 51 | 96 ± 5 | –25.4 | 374 | 81 |
| **c-L35** | | | 45 | 77 ± 3 | –25.2 | 319 | 64 |
| ***l*-L64(OH)** | $(EG)_{13}$–$(PG)_{30}$–$(EG)_{13}$ | 2,900 | 35 | 182 ± 10 | –24.6 | 670 | 64 |
| ***l*-L64(OMe)** | | | 36 | 183 ± 9 | –24.7 | 672 | 68 |
| ***c*-L64** | | | 31 | 156 ± 2 | –24.3 | 593 | 56 |
| ***l*-10R5(OH)** | $(PG)_8$–$(EG)_{22}$–$(PG)_8$ | 2,000 | 69 | 145 ± 6 | –26.9 | 505 | 72 |
| ***l*-10R5(OMe)** | | | 65 | 152 ± 20 | –26.5 | 530 | 66 |
| ***c*-10R5** | | | 62 | 94 ± 7 | –25.9 | 365 | 70 |
| ***l*-17R4(OH)** | $(PG)_{14}$–$(EG)_{24}$–$(PG)_{14}$ | 2,700 | 46 | 173 ± 3 | –26.4 | 625 | 49 |
| ***l*-17R4(OMe)** | | | 42 | 230 ± 30 | –26.1 | 804 | 44 |
| ***c*-17R4** | | | 28 | 77 ± 5 | –24.9 | 339 | 53 |

[a] Average molecular weights reported from the manufacturer were used for the calculation of thermodynamic parameters of micellization.

[b] Thermodynamic parameters obtained for 10 g/L solutions at $T_{CMT}$.

### 3.3.3. Cloud point measurement by temperature-dependent transmittance

The temperature-dependent transparency (%T) of Pluronic surfactant solution at 1 wt% was measured to determine the aggregation and phase separation behaviour (Figure 3-4). Here, the cloud point ($T_c$) was defined by the lowest temperature at which the transmittance of 595 nm became 90% or less. In order to separate the consequence of cyclization into the effect on the heat-induced dehydration and coil-globule transition through (i) the elimination of the strongly hydrophilic hydroxy end groups, and (ii) other structural effects such as conformational restriction of the unique ring topology, $T_c$ for linear chain-end methylated species were investigated alongside its linear counterparts with hydroxy end-groups and cyclic species. For the ABA-type Pluronic, a significant decrease in $T_c$ was observed for the cyclic species. For example, $T_c$ of ***c*-L35** and ***c*-L64** at 64 and 56 °C, respectively, were comparably lower than their linear hydroxy-terminated counterparts (***l*-L35(OH)**, 82 °C; ***l*-L64(OH)**, 64 °C in Table 3-1). In contrast, cyclization of the BAB-type copolymers resulted in comparable $T_c$ to their corresponding linear hydroxy-terminated species. For instance, $T_c$ of ***l*-10R5(OH)** and ***c*-10R5** were 72 and 70 °C, respectively, while that of ***l*-17R4(OH)** and ***c*-17R4** were 49 and 53 °C, respectively. Interestingly, the linear methoxy-terminated species (***l*-L35(OMe)**, 81 °C; ***l*-L64(OMe)**, 68 °C; ***l*-10R5(OMe)**, 66 °C; and ***l*-17R4(OMe)**, 44 °C) gave completely different $T_c$ values and tendency to that of cyclized species, where comparable or increased $T_c$ were obtained for the ABA-type copolymers in contrast to significant decreases in $T_c$ for the BAB-type copolymer solutions. The obtained results suggest a clear distinction in the topology effect of cyclization to that of chemical modification of the chain-ends on the clouding phenomena.

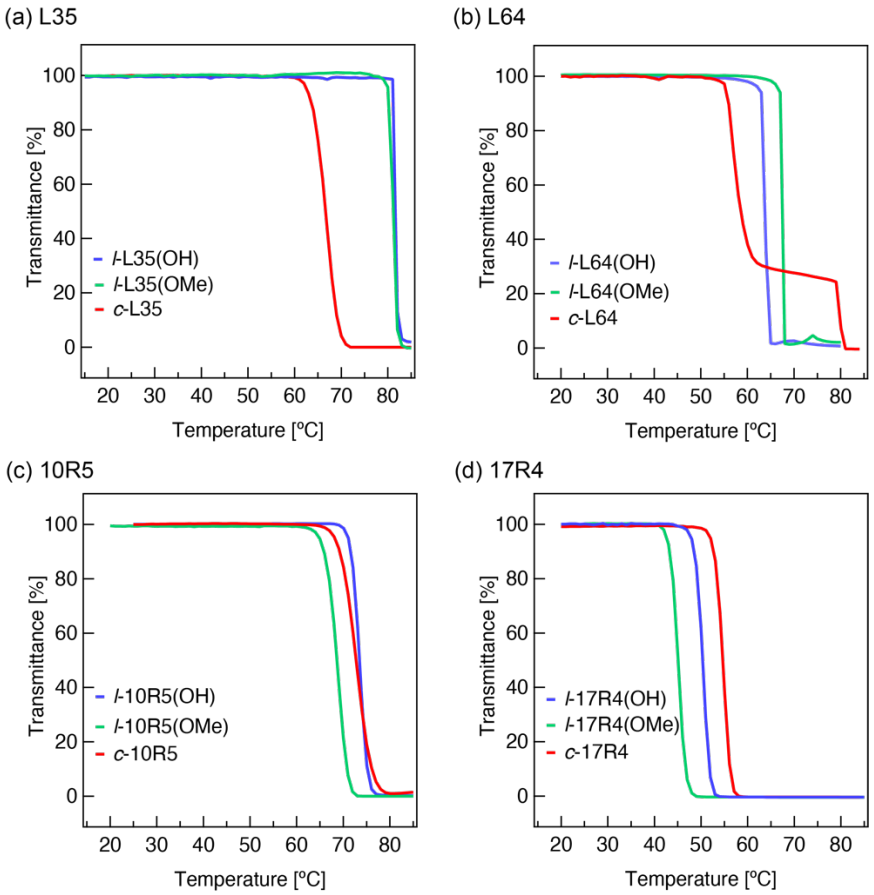


**Figure 3-4.** (a) Temperature-dependent transmittance (%T) at 595 nm for 10 g/L aqueous solutions of linear hydroxy-terminated (blue), methoxy-terminated (green), and cyclized (red) L35, indicated as *l*-L35(OH), *l*-L35(OMe) and *c*-L35, respectively. Those of (b) L64, (c) 10R5 and (d) 17R4 are also shown.

To rationally explain the differences in transmittance changes upon temperature elevation of the ABA-type Pluronic copolymer solutions, interpretation of clouding mechanism is required. First, both linear hydroxy- and methoxy-terminated species of L35 and L64 (***l*-L35(OH)**, ***l*-L35(OMe)**, ***l*-L64(OH)** and ***l*-L64(OMe)**), displayed similar %T profiles, where the transmittance drastically drops at the $T_c$. Clouding behavior of Pluronic copolymers to arise from phase transition induced through the dehydration and conformational change of the PEG segment is widely known[23, 45], and our results suggest methylation of the chain-ends not to affect this mechanism. The %T profiles of the cyclized species of the ABA-type copolymers solutions indicate a distinct aggregation upon temperature elevation; the transition of the cyclized species took place over a wider temperature range compared to their linear counterparts, especially for ***c*-L64** (Figure 4a, b). A similar phenomenon was reported on the phase transition of cyclic poly(*N*-isopropylacrylamide) (PNIPAM), explained to be caused by the disturbed packing of the polymer chains upon a coil-to-globule transformation due to the lack of chain ends[46, 47], suggesting an analogous behavior to be exhibited in our system.

BAB-type copolymers are rationally expected to form flower-like micelles in water, with a fraction of copolymer chains are expected to exist as or become “dangling chains” upon temperature elevation. The presence of “dangling chains” in these flower-like micelles is explained to act as inter-micellar bridging agents which cause macroscopic aggregation, where cyclization resulted in the elimination of this agglomeration mechanism[14, 15]. In the case of the present Pluronic copolymers, contribution from inhibition of the inter-micellar bridging was possibly observed for ***c*-17R4**, resulting in the slight increase of its $T_c$. On the other hand, the decreased $T_c$ value for the linear methoxy-terminated species can be interpretated as a consequence of reduced solvation of the hydrophobic segment of the polymer, resulting in enhanced micellar bridging agglomeration to precede before phase transition.

When the chain conformations and the freedom of each block in the micellar state are

taken into account, linear triblock ABA-, BAB-type and cyclic AB-type species are all expected to exhibit different characteristics (Figure 3-5). For example, the two PEG segments of linear ABA-type copolymers are only attached to the core–corona interface at one end of each block, in contrast to the looped PEG corona of linear BAB-type and cyclized species, with both PEG chain-ends attached to the core. This is expected to produce significant differences in the conformational freedom of the PEG blocks, which may influence the hydration and $T_c$. Thus, the significant decrease in $T_c$ upon cyclization observed only for the ABA-type copolymers can be explained to result in the fixture of the free block ends to the core–corona interface, restricting its conformation.

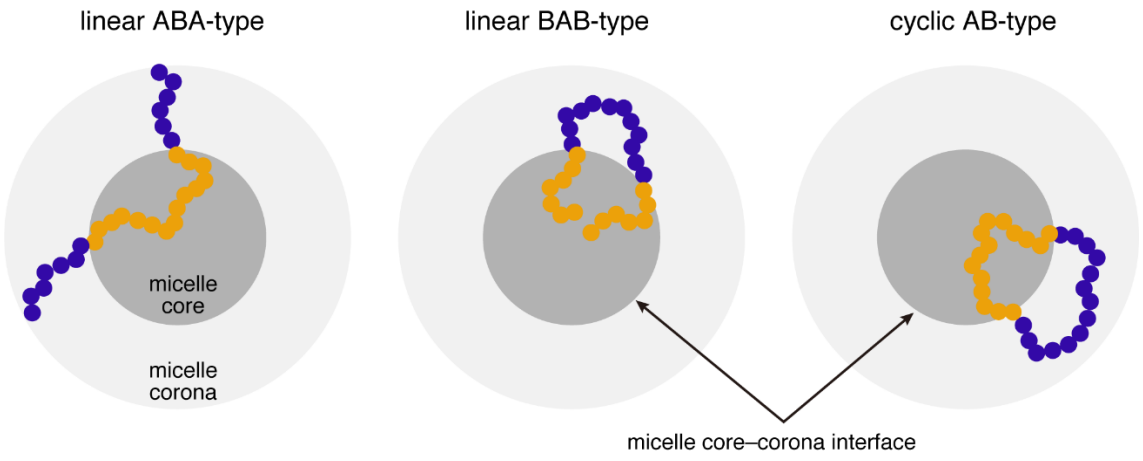


**Figure 3-5.** Schematic illustration of the expected conformations of linear ABA-type (left), linear BAB-type (center) and cyclized (right) copolymers in the micellar state. Cyclization results in the fixture of the PEG segment ends at the core–corona interface, and thus, is expected to affect the phase transition phenomena more prominently for the ABA-type copolymer.

The above results on cyclized Pluronics suggests loops, or cyclic topology to decrease the phase separation temperatures in general. To test whether that property is prevalent for other polymers, cloud point measurements on *c*-PEG solutions were conducted for various molecular weights and at a variety of concentrations. For PEG in aqueous solution, the critical temperature of phase separation lies above the boiling point of water. However, introduction of lyotropic salts have been found to lower the phase separation temperature,[48, 49] which is an evident indication of the worsening of solvent quality. Thus, the critical temperatures of phase separation for *l*-PEG and *c*-PEG in 0.5 M $K_2SO_4$ aqueous solutions were compared through cloud point measurements, where transmittance (%T) changes of the solution were monitored during temperature elevation. Plots of %T vs temperature for solutions of *l*-$PEG_{10k}$ and *c*-$PEG_{10k}$ at various concentrations are shown as an example in Figure 3-6, and %T changes for PEGs of other molecular weights are shown in Figure S3-1. The effects of PEG molecular weight and concentration onto the cloud point temperature ($T_{cp}$) are summarized in Figure 3-7.

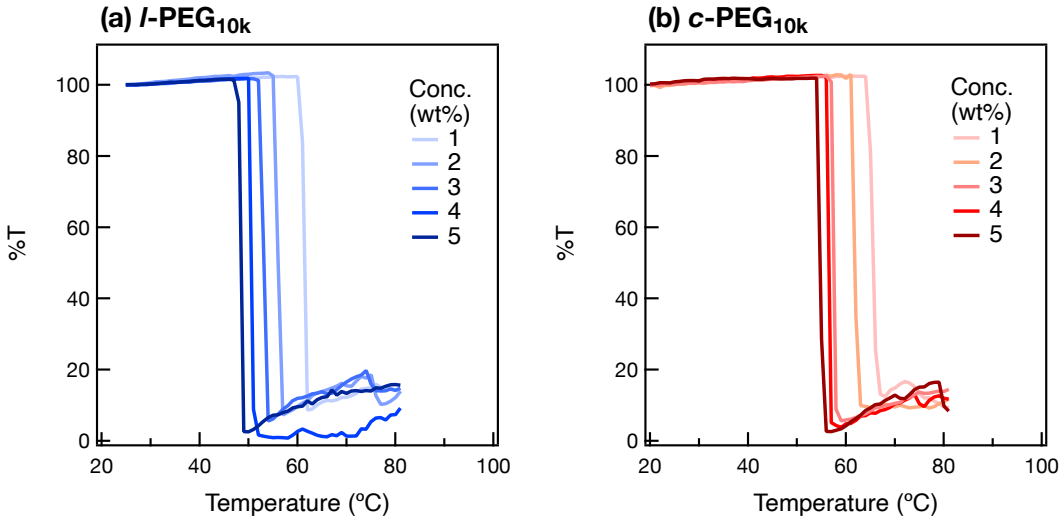


**Figure 3-6**. Transmittance (%T) changes upon temperature elevation for *l*-$PEG_{10k}$ and *c*-$PEG_{10k}$ in 0.50 M $K_2SO_4$ aqueous solution.

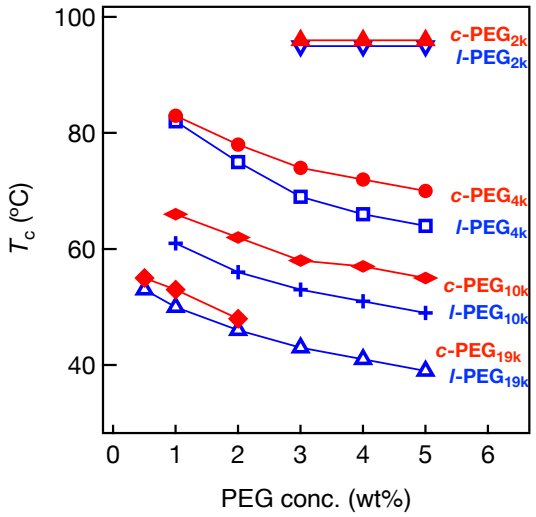


**Figure 3-7**. Relationship between cloud point temperature ($T_c$) and polymer concentration for *l*-PEG and *c*-PEG of various molecular weights.

From the abrupt drop in %T at the $T_{cp}$ in Figure 3-6 and S3-1, both *l*-PEG and *c*-PEG were found to display clear transition points at all concentrations measured in this study, regardless of their topology. These results were unlike the phase transition behaviour for linear and cyclic PNIPAMs, where cyclices displayed a relatively gradual change, which further broadened for samples of low concentration.[47] Upon comparison of the $T_{cp}$, *c*-$PEG_{10k}$ was found to display transition temperatures that were 5–6 ºC higher ($T_{cp}$ = 66, 62, 58, 57, 55 ºC for 1, 2, 3, 4 and 5 wt% solutions, respectively) to *l*-$PEG_{10k}$ at all their corresponding concentrations ($T_{cp}$ = 61, 56, 53, 51, 49 ºC for 1, 2, 3, 4 and 5 wt% solutions, respectively). Phase separation of PEG in aqueous solution is attributed to its dehydration, and even the smallest changes in chemical structure (such as terminal moiety) are known to influence the transition point.[50] Purely based on chemical structure, *c*-PEG which lacks two (terminal) hydroxy- groups of *l*-PEG, is anticipated to result in a lower $T_{cp}$ due to its increased hydrophobic nature. However, the opposite, i.e. increased $T_{cp}$ was observed for *c*-$PEG_{10k}$. This contradiction, suggests the topological excluded-volume effect to contribute to an apparent solubilization of *c*-PEGs, effectively negating its decreased hydrophilicity of its chemical structure. Furthermore, $T_{cp}$ were found to decrease upon increase in concentration for both *l*-PEG and *c*-PEG with the exception of $PEG_{2k}$, probably due to their relatively high solubility even under this salted-out condition. Focusing on molecular-weight dependency, PEGs of larger molecular weights tended to have decreased $T_{cp}$. Both trends in concentration and molecular weight dependency of $T_{cp}$ are in agreement with the behavior of linear PEGs reported in literature.[51, 52] Thus, the cyclic topology was found to shift the $T_{cp}$ to higher temperatures for LCST-type homopolymers, essentially resulting in the expansion of apparent solubility limit of cyclic polymers. The results for PEG homopolymers suggest the phase separation phenomena and the impact of cyclic topology to be distinct between PEG and Pluronics, where for PEG systems, a direct transition from solvated state to a two-phase system occurred. On the other

hand, the Pluronic system that involved transition from a micellar solution to a macro-phase separated state was possibly governed by a more complex effect of crowded loops and cyclices at the micelle–water interface.

### 3.3.4. Dynamic light scattering (DLS)

In light of the anomalous association behaviour observed for ***c*-L64**, a structural investigation into the micellar aggregate size was conducted for L64 using dynamic light scattering (DLS) (Figure 3-8). The number distribution profiles of hydrodynamic diameter ($D_h$) of 1 wt% solutions of ***l*-L64(OH)** and ***c*-L64** at various temperatures is shown in Figure 3-7. The number distribution profiles were selected to depict a more accurate aggregation behaviour of the copolymer systems, due to its susceptibility of heavy influence from just a minor presence of large particles. In consistency with the dye solubilization measurements, the $D_h$ of both linear and cyclic L64 around 2 nm indicate the copolymers to be dissolved in the unimer state under the CMT. An evident size increase can be observed at 40 ºC for ***l*-L64(OH)**, and at 35 ºC for ***c*-L64**, respectively. While both suggest micellization around these temperatures, the large apparent micelle size for ***c*-L64** at 35 ºC indicate possible contribution from cyclized residual impurities in the material. At 40 and 50 ºC, both linear and cyclic copolymer systems display a single peak profile around 10–20 nm, indicating well defined micellar aggregates. Temperature elevation for ***l*-L64(OH)** reveal a sudden size and distribution width increase between 60 ºC and 70 ºC, which did not change upon further elevation to 80 ºC. In contrast, a jump in size for the ***c*-L64** system was observed between 50 ºC and 60 ºC, producing aggregates of around 60–100 nm up until 70 ºC, with a second size increase observed at 80 ºC, producing macroscopic aggregates. The DLS results are in complete consistency with the temperature-dependent transparency measurements, where phase transition from transparent to opaque occur for ***l*-L64(OH)** between 60 and 70 ºC, while the ***c*-L64** system undergoes a two-step transition, producing a translucent phase composed of micellar aggregates with the diameter of around 60–100 nm, between 60 and 80 ºC.

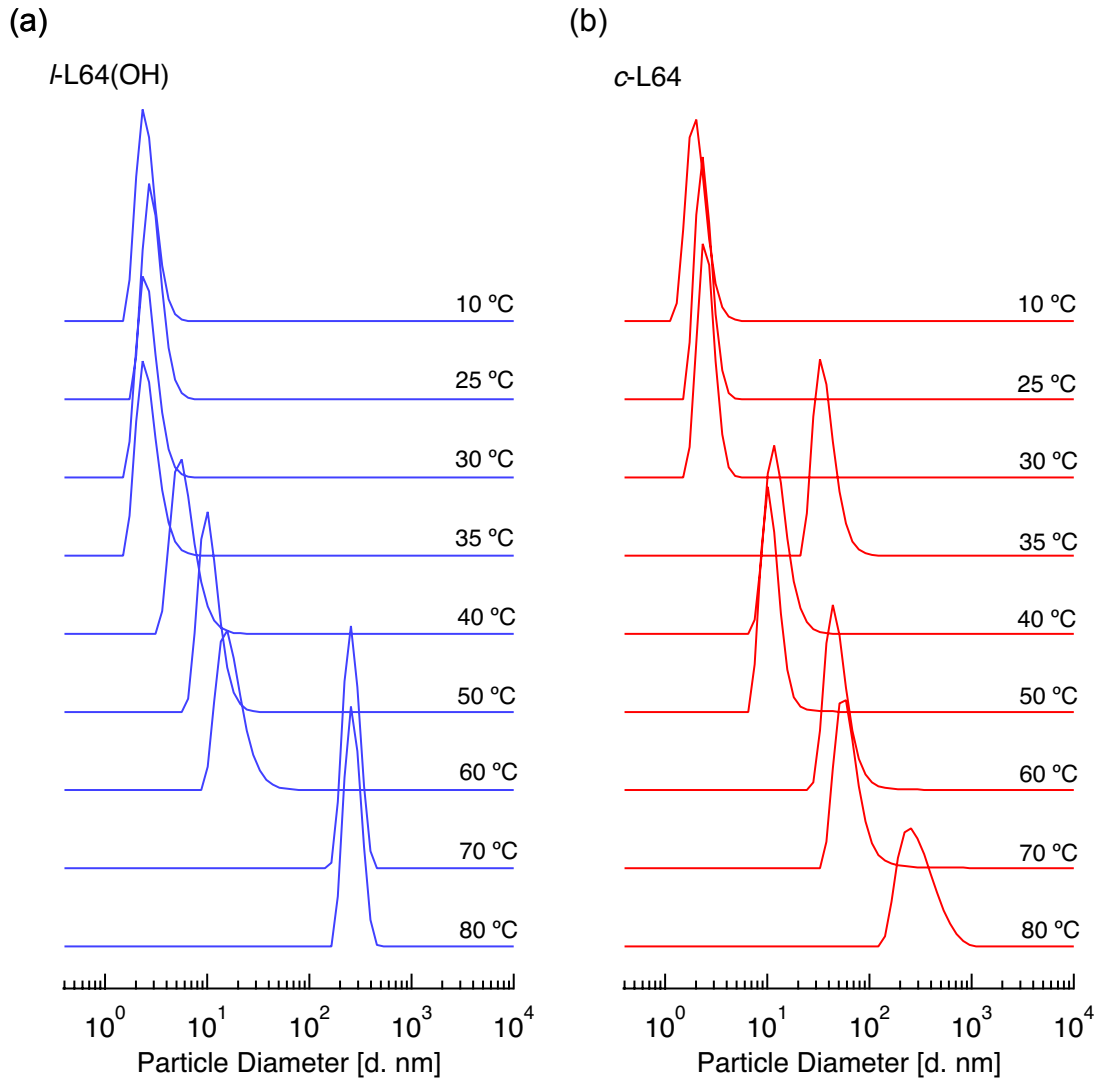


**Figure 3-8.** Number size distribution obtained from dynamic light scattering (DLS) at various temperatures for 1 wt% aqueous solutions of (a) ***l*-L64(OH)** and (b) ***c*-L64**. Contrasting aggregation behaviour at elevated temperatures between 60 ºC and 70 ºC were observed, along with clear micelle formation at 40 ºC.

## 3.4. CONCLUSIONS

The effect of cyclization was observed for Pluronic surfactants L35, L64, 10R5 and 17R4 in its their micellization and phase separation properties. Investigation into thermodynamic properties of micellization revealed decreased CMT, enthalpy and entropy for cyclized species with a more pronounced effect for BAB-type surfactants. This is believed to be due to a more effective shielding of the hydrophobic PPG segment by the hydrophilic PEG segments in cyclized surfactants in the unimer state, leading to a reduced enthalpic penalty and weaker entropic driving force. In addition, light transmittance and DLS measurements of polymer solutions revealed a contrasting effect on the thermal stability of Pluronic micelles. While a stabilizing effect on 17R4 micelles were observed due to inhibition of inter-micelle chain-bridging, cyclization of ABA-type Pluronics resulted in destabilization of the micelles, with a distinct phase formation at elevated temperatures. On the other hand, phase separation behaviour of cyclic PEG homopolymers, also revealed stabilizing effects of cyclices through an increase in clouding temperatures. The apparent contradiction is suggested to originate from the initial structures of the system near the critical point, where PEG homopolymers are molecularly dissolved, while Pluronics already have an aggregated micellar system. Thus, the molecularly crowded interface between micelle corona and the solvent likely resulted in amplified, and distinct effects of the cyclic topology.

## 3.5. REFERENCES

(1) *Topological Polymer Chemistry: Progress of Cyclic Polymers in Syntheses, Properties and Functions*; World Scientific, 2013.

(2) Haque, F. M.; Grayson, S. M. The synthesis, properties and potential applications of cyclic polymers. *Nat. Chem.* **2020**, 433-444. DOI: 10.1038/s41557-020-0440-5.

(3) Lienard, R.; De Winter, J.; Coulembier, O. Cyclic polymers: Advances in their synthesis, properties, and biomedical applications. *J. Polym. Sci.* **2020**, *58* (11), 1481-1502. DOI: 10.1002/pol.20200236.

(4) Morgese, G.; Trachsel, L.; Romio, M.; Divandari, M.; Ramakrishna, S. N.; Benetti, E. M. Topological Polymer Chemistry Enters Surface Science: Linear versus Cyclic Polymer Brushes. *Angew. Chem., Int. Ed.* **2016**, *55* (50), 15583-15588. DOI: 10.1002/anie.201607309.

(5) Wang, Y. B.; Quinsaat, J. E. Q.; Ono, T.; Maeki, M.; Tokeshi, M.; Isono, T.; Tajima, K.; Satoh, T.; Sato, S.; Miura, Y.; et al. Enhanced dispersion stability of gold nanoparticles by the physisorption of cyclic poly(ethylene glycol). *Nat. Commun.* **2020**, *11* (1). DOI: 10.1038/s41467-020-19947-8.

(6) Morgese, G.; Cavalli, E.; Rosenboom, J.-G.; Zenobi-Wong, M.; Benetti, E. M. Cyclic Polymer Grafts That Lubricate and Protect Damaged Cartilage. *Angew. Chem., Int. Ed.* **2018**, *57* (6), 1621-1626. DOI: 10.1002/anie.201712534.

(7) Zhang, K.; Lackey, M. A.; Cui, J.; Tew, G. N. Gels Based on Cyclic Polymers. *J. Am. Chem. Soc.* **2011**, *133* (11), 4140-4148. DOI: 10.1021/ja111391z.

(8) Oziri, O. J.; Wang, Y. B.; Watanabe, T.; Uno, S.; Maeki, M.; Tokeshi, M.; Isono, T.; Tajima, K.; Satoh, T.; Sato, S. I.; et al. PEGylation of silver nanoparticles by physisorption of cyclic poly(ethylene glycol) for enhanced dispersion stability, antimicrobial activity, and cytotoxicity. *Nanoscale Adv.* **2022**, *4* (2), 532-545. DOI: 10.1039/d1na00720c.

(9) Oziri, O. J.; Maeki, M.; Tokeshi, M.; Isono, T.; Tajima, K.; Satoh, T.; Sato, S.; Yamamoto,

T. Topology-Dependent Interaction of Cyclic Poly(ethylene glycol) Complexed with Gold Nanoparticles against Bovine Serum Albumin for a Colorimetric Change. *Langmuir* DOI: 10.1021/acs.langmuir.1c03027.

(10) Williams, R. J.; Dove, A. P.; O'Reilly, R. K. Self-assembly of cyclic polymers. *Polym. Chem.* **2015**, *6* (16), 2998-3008. DOI: 10.1039/c5py00081e.

(11) Heo, K.; Kim, Y. Y.; Kitazawa, Y.; Kim, M.; Jin, K. S.; Yamamoto, T.; Ree, M. Structural Characteristics of Amphiphilic Cyclic and Linear Block Copolymer Micelles in Aqueous Solutions. *ACS Macro Lett.* **2014**, *3* (3), 233-239. DOI: 10.1021/mz5000224.

(12) Ree, B. J.; Satoh, T.; Yamamoto, T. Micelle Structure Details and Stabilities of Cyclic Block Copolymer Amphiphile and Its Linear Analogues. *Polymers* **2019**, *11* (1). DOI: 10.3390/polym11010163.

(13) Zhang, B.; Zhang, H.; Li, Y.; Hoskins, J. N.; Grayson, S. M. Exploring the Effect of Amphiphilic Polymer Architecture: Synthesis, Characterization, and Self-Assembly of Both Cyclic and Linear Poly(ethylene gylcol)-b-polycaprolactone. *ACS Macro Lett.* **2013**, *2* (10), 845-848. DOI: 10.1021/mz4003936.

(14) Honda, S.; Yamamoto, T.; Tezuka, Y. Tuneable enhancement of the salt and thermal stability of polymeric micelles by cyclized amphiphiles. *Nat. Commun.* **2013**, *4*, 1574. DOI: 10.1038/ncomms2585.

(15) Honda, S.; Yamamoto, T.; Tezuka, Y. Topology-directed control on thermal stability: Micelles formed from linear and cyclized amphiphilic block copolymers. *J. Am. Chem. Soc.* **2010**, *132* (30), 10251-10253. DOI: 10.1021/ja104691j.

(16) Wada, H.; Kitazawa, Y.; Kuroki, S.; Tezuka, Y.; Yamamoto, T. NMR Relaxometry for the Thermal Stability and Phase Transition Mechanism of Flower-like Micelles from Linear and Cyclic Amphiphilic Block Copolymers. *Langmuir* **2015**, *31* (32), 8739-8744. DOI: 10.1021/acs.langmuir.5b01902.

(17) Yamamoto, T.; Masuda, Y.; Tezuka, Y.; Korchagina, E.; Winnik, F. M. Comparative Thermodynamic Studies of the Micellization of Amphiphilic Block Copolymers before and after Cyclization. *Langmuir* DOI: 10.1021/acs.langmuir.0c03358.

(18) Vaughn, T. H.; Suter, H. R.; Lundsted, L. G.; Kramer, M. G. Properties of Some Newly Developed Nonionic Detergents. *J. Amer. Oil Chem. Soc.* **1951**, *28* (7), 294-299. DOI: 10.1007/bf02648649.

(19) D'Errico, G.; Paduano, L.; Khan, A. Temperature and concentration effects on supramolecular aggregation and phase behavior for poly(propylene oxide)-b-poly(ethylene oxide)-b-poly(propylene oxide) copolymers of different composition in aqueous mixtures, *J. Colloid Interface Sci.* **2004**, *279* (2), 379-390. DOI: 10.1016/j.jcis.2004.06.063.

(20) Caragheorgheopol, A.; Schlick, S. Hydration in the various phases of the triblock copolymers EO13PO30EO13 (Pluronic L64) and EO6PO34EO6 (Pluronic L62), based on electron spin resonance spectra of cationic spin probes. *Macromolecules* **1998**, *31* (22), 7736-7745. DOI: 10.1021/ma980982g.

(21) Kozlov, M. Y.; Melik-Nubarov, N. S.; Batrakova, E. V.; Kabanov, A. V. Relationship between pluronic block copolymer structure, critical micellization concentration and partitioning coefficients of low molecular mass solutes. *Macromolecules* **2000**, *33* (9), 3305-3313. DOI: 10.1021/ma991634x.

(22) Landazuri, G.; Fernandez, V. V. A.; Soltero, J. F. A.; Rharbi, Y. Length of the Core Forming Block Effect on Fusion and Fission Dynamics at Equilibrium in PEO-PPO-PEO Triblock Copolymer Micelles in the Spherical Regime. *Macromolecules* **2021**, *54* (5), 2494-2505. DOI: 10.1021/acs.macromol.0c01520.

(23) Naskar, B.; Ghosh, S.; Moulik, S. P. Solution Behavior of Normal and Reverse Triblock Copolymers (Pluronic L44 and 10R5) Individually and in Binary Mixture. *Langmuir* **2012**, *28* (18), 7134-7146. DOI: 10.1021/la3000729.

(24) Zhou, Z.; Chu, B. Phase-behavior and Association Properties of Poly(oxypropylene)-poly(oxyethylene)-poly(oxypropylene) Triblock Copolymer in Aqueous Solution. *Macromolecules* **1994**, *27* (8), 2025-2033. DOI: 10.1021/ma00086a008.

(25) Jebari, M. M.; Ghaouar, N.; Aschi, A.; Gharbi, A. Aggregation behaviour of Pluronic((R)) L64 surfactant at various temperatures and concentrations examined by dynamic light scattering and viscosity measurements. *Polym. Int.* **2006**, *55* (2), 176-183. DOI: 10.1002/pi.1935.

(26) Yu, G.-E.; Garrett, C. A.; Mai, S. M.; Altinok, H.; Attwood, D.; Price, C.; Booth, C. Effect of cyclization on the association behavior of block copolymers in aqueous solution. Comparison of oxyethylene/oxypropylene block copolymers cyclo-P34E104 and E52P34E52. *Langmuir* **1998**, *14* (9), 2278-2285.

(27) Watanabe, T.; Chimura, S.; Wang, Y. B.; Ono, T.; Isono, T.; Tajima, K.; Satoh, T.; Sato, S.; Ida, D.; Yamamoto, T. Cyclization of PEG and Pluronic Surfactants and the Effects of the Topology on Their Interfacial Activity. *Langmuir* **2021**, *37* (23), 6974-6984. DOI: 10.1021/acs.langmuir.1c00513.

(28) Kositza, M. J.; Bohne, C.; Alexandridis, P.; Hatton, T. A.; Holzwarth, J. F. Micellization dynamics and impurity solubilization of the block-copolymer L64 in an aqueous solution. *Langmuir* **1999**, *15* (2), 322-325. DOI: 10.1021/la9812368.

(29) Alexandridis, P.; Holzwarth, J. F.; Hatton, T. A. Micellization of Poly(Ethylene Oxide)-poly(Propylene Oxide)-poly(Ethylene Oxide) Triblock Copolymers in Aqueous-solutions - Thermodynamics of Copolymer Association. *Macromolecules* **1994**, *27* (9), 2414-2425. DOI: 10.1021/ma00087a009.

(30) Cooke, J.; Viras, K.; Yu, G.-E.; Sun, T.; Yonemitsu, T.; Ryan, A. J.; Price, C.; Booth, C. Large cyclic poly(oxyethylene)s: Chain folding in the crystalline state studied by Raman spectroscopy, X-ray scattering, and differential scanning calorimetry. *Macromolecules* **1998**,

*31* (9), 3030-3039. DOI: 10.1021/ma9717909.

(31) Mata, J. P.; Majhi, P. R.; Guo, C.; Liu, H. Z.; Bahadur, P. Concentration, temperature, and salt-induced micellization of a triblock copolymer Pluronic L64 in aqueous media. *J. Colloid Interface Sci.* **2005**, *292* (2), 548-556. DOI: 10.1016/j.jcis.2005.06.013.

(32) Sharma, R. K.; Shah, U. Aggregation Behavior of PEO-PPO-PEO Tri-Block Copolymer (Pluronic (R) L64) in Nonionic Surfactant Additives Environment. *Tenside Surfact. Det.* **2014**, *51* (3), 274-281. DOI: 10.3139/113.110308.

(33) Ganguly, R.; Choudhury, N.; Aswal, V. K.; Hassan, P. A. Pluronic L64 Micelles near Cloud Point: Investigating the Role of Micellar Growth and Interaction in Critical Concentration Fluctuation and Percolation. *J. Phys. Chem. B* **2009**, *113* (3), 668-675. DOI: 10.1021/jp808304w.

(34) Liao, C. Y.; Choi, S. M.; Mallamace, F.; Chen, S. H. SANS study of the structure and interaction of L64 triblock copolymer micellar solution in the critical region. *J. Appl. Crystallogr.* **2000**, *33* (1), 677-681. DOI: 10.1107/s0021889899013205.

(35) Yang, L.; Alexandridis, P.; Steytler, D. C.; Kositza, M. J.; Holzwarth, J. F. Small-angle neutron scattering investigation of the temperature-dependent aggregation behavior of the block copolymer pluronic L64 in aqueous solution. *Langmuir* **2000**, *16* (23), 8555-8561. DOI: 10.1021/la000008m.

(36) Huff, A.; Patton, K.; Odhner, H.; Jacobs, D. T.; Clover, B. C.; Greer, S. C. Micellization and Phase Separation for Triblock Copolymer 17R4 in $H_2O$ and in $D_2O$. *Langmuir* **2011**, *27* (5), 1707-1712. DOI: 10.1021/la104350g.

(37) Kumi, B. C.; Hammouda, B.; Greer, S. C. Self-assembly of the triblock copolymer 17R4 poly(propylene oxide)(14)-poly(ethylene oxide)(24)-poly(propylene oxide)(14) in D2O. *J. Colloid Interface Sci.* **2014**, *434*, 201-207. DOI: 10.1016/j.jcis.2014.07.049.

(38) Yu, G.-E.; Yang, Z.; Attwood, D.; Price, C.; Booth, C. Association and surface properties

of a cyclic block copolymer of ethylene oxide and butylene oxide (Cyclo-B(8)E(42)) in water. *Macromolecules* **1996**, *29* (26), 8479-8486.

(39) Kelarakis, A.; Havredaki, V.; Rekatas, C. J.; Booth, C. Thermodynamics of micellisation of a diblock copolymer of ethylene oxide and styrene oxide in water. *Phys. Chem. Chem. Phys.* **2001**, *3* (24), 5550-5552. DOI: 10.1039/b107374e.

(40) Chandler, D. Interfaces and the driving force of hydrophobic assembly. *Nature* **2005**, *437* (7059), 640-647. DOI: 10.1038/nature04162.

(41) Kim, S. H.; Jo, W. H. A Monte Carlo simulation for the micellization of ABA- and BAB-type triblock copolymers in a selective solvent. *Macromolecules* **2001**, *34* (20), 7210-7218. DOI: 10.1021/ma0105136.

(42) Kim, S. H.; Jo, W. H. A Monte Carlo simulation for the micellization of ABA- and BAB-type triblock copolymers in a selective solvent. II. Effects of the block composition. *J. Chem. Phys.* **2002**, *117* (18), 8565-8572. DOI: 10.1063/1.1512646.

(43) Manet, S.; Lecchi, A.; Imperor-Clerc, M.; Zholobenko, V.; Durand, D.; Oliveira, C. L. P.; Pedersen, J. S.; Grillo, I.; Meneau, F.; Rochas, C. Structure of Micelles of a Nonionic Block Copolymer Determined by SANS and SAXS. *J. Phys. Chem. B* **2011**, *115* (39), 11318-11329. DOI: 10.1021/jp200212g.

(44) Pedersen, J. S.; Gerstenberg, M. C. The structure of P85 Pluronic block copolymer micelles determined by small-angle neutron scattering. *Coll. Surf. A Phys. Eng. Asp.* **2003**, *213* (2-3), 175-187. DOI: 10.1016/s0927-7757(02)00511-3.

(45) Almgren, M.; Brown, W.; Hvidt, S. Self-aggregation and Phase-behavior of Poly(Ethylene Oxide) Poly(Propylene Oxide) Poly(Ethylene Oxide) Block-Copolymers in Aqueous Solution. *Colloid Polym. Sci.* **1995**, *273* (1), 2-15. DOI: 10.1007/bf00655668.

(46) Qiu, X.-P.; Tanaka, F.; Winnik, F. M. Temperature-induced phase transition of well-defined cyclic poly(N-isopropylacrylamide)s in aqueous solution. *Macromolecules* **2007**, *40* (20),

7069-7071. DOI: 10.1021/ma071359b.

(47) Xu, J.; Ye, J.; Liu, S. Synthesis of well-defined cyclic poly(N-isopropylacrylamide) via click chemistry and its unique thermal phase transition behavior. *Macromolecules* **2007**, *40* (25), 9103-9110. DOI: 10.1021/ma0717183.

(48) Boucher, E. A.; Hines, P. M. Effects of inorganic salts on the properties of aqueous poly(ethylene oxide) solutions. *J. Polym. Sci., Polym. Phys. Ed.* **1976**, *14*, 2241-2251.

(49) Lundberg, R.; Bailey, F.; Callard, R. Interactions of Inorganic Salts With Poly(Ethylene Oxide). *J. Polym. Sci. A Polym. Chem.* **1966**, *4*, 1563-&.

(50) Dormidontova, E. Influence of end groups on phase behavior and properties of PEO in aqueous solutions. *Macromolecules* **2004**, *37* (20), 7747-7761. DOI: 10.1021/ma035609+.

(51) Saeki, S.; Kuwahara, N.; Nakata, M.; Kaneko, M. Phase Separation of Poly(Ethylene Glycol) Water Salt Systems. *Polym.* **1977**, *18*, 1027-1031.

(52) Grinberg, V.; Burova, T.; Grinberg, N.; Dubovik, A.; Papkov, V.; Khokhlov, A. Energetics of LCST transition of poly(ethylene oxide) in aqueous solutions. *Polym.* **2015**, *73*, 86-90. DOI: 10.1016/j.polymer.2015.07.032.

## 3.6. SUPPORTING FIGURES AND TABLES

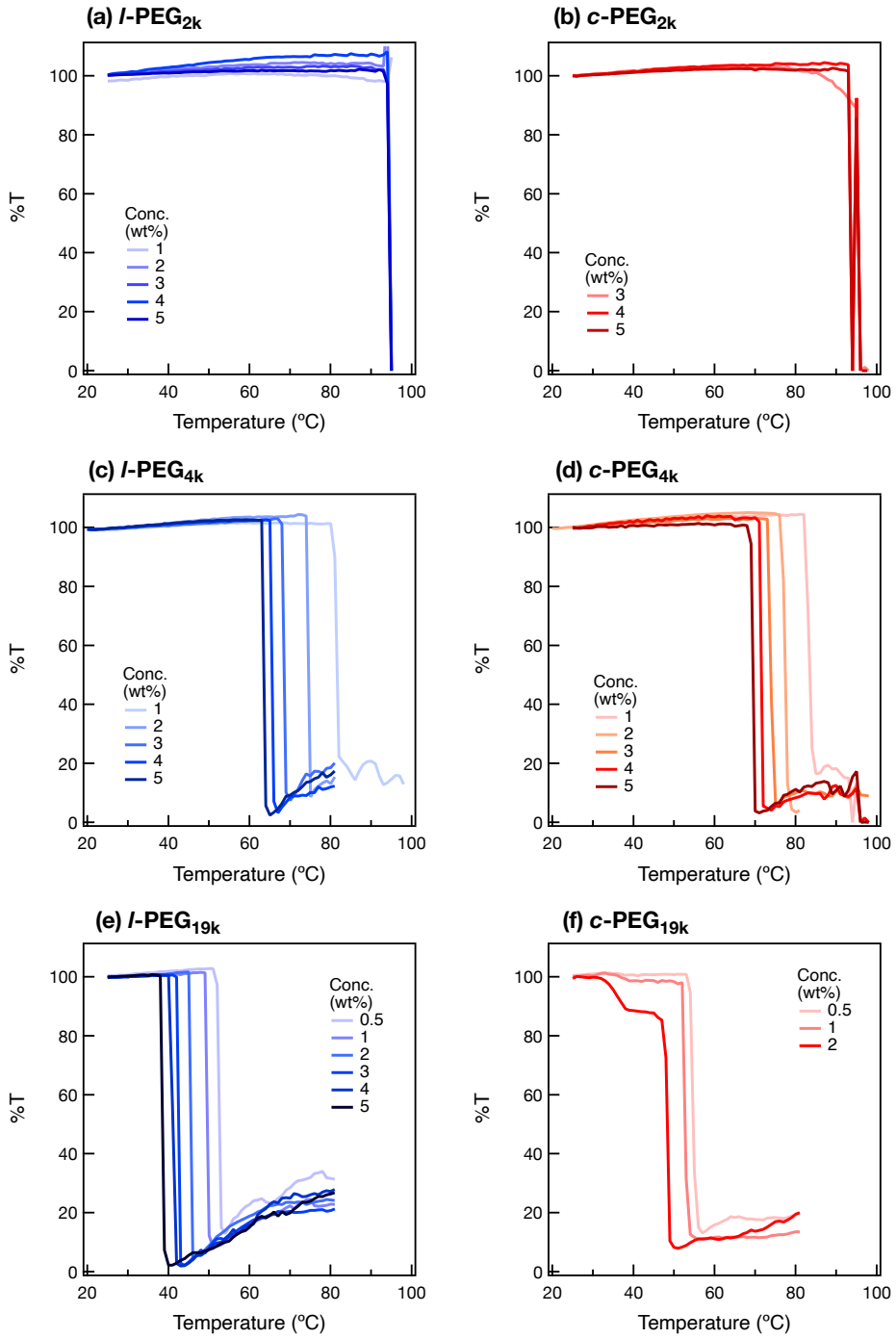


**Figure S3-1**. Temperature-dependent %T changes for *l*-PEG and *c*-PEGs at various molecular weights and concentrations in 0.5 M $K_2SO_4$ aqueous solution.

# *Chapter 4*

## Structural studies of cyclic PEG and their gold nanoparticle complexes through small-angle X-ray and neutron scattering

## 4.1. INTRODUCTION

The topological uniqueness of cyclic polymers, characterized by its ring-like architecture lacking chain-ends, result in a number of physical properties that are distinct from their linear counterparts.[1, 2] Fundamental understanding of the physical properties of cyclic polymers is not only limited to scientific interest, but also crucial in the recent surge of interest toward potential applications and incorporation into material design.[3, 4] Naturally, the physicochemical properties of cyclic polymers have been the subject of extensive studies.[5, 6] For instance, cyclic polymers have been shown to possess relatively smaller hydrodynamic volumes in solution to their linear counterparts,[7] and feature lower intrinsic viscosity[8] and higher glass-transition temperatures[9, 10] in their melt and bulk states.

Experimentally, the most well-studied polymeric system of cyclic polymers is polystyrenes (PS). Synthesis via the ring-closure approach,[11] in many cases combined with fractionation by liquid chromatographic techniques have yielded corresponding sets of linear and cyclic PS of extremely high purity,[12, 13] which enabled unambiguous identification of key properties originating from the ring topology.[14, 15] Amongst other well-studied systems, polyethylene glycol (PEG) is of interest due to its hydrophilic backbones and biocompatibility that makes it relevant in biomedical applications.[16] Despite early synthetic reports on cyclic analogous of PEG, i.e., *c*-PEG, investigations of their properties have mostly focused on their behavior in the bulk[17] and melt states,[18-20] with very limited reports in solution.[21, 22] In fact, to the best of my knowledge, there has been no previous experimental reports on the conformations of *c*-PEG in dilute solution, in direct comparison with their corresponding linear counterparts of identical molecular weight.

From an application point of view, I have previously reported several unique properties of *c*-PEG, such as enhanced interfacial activity at the air–water interface,[23] and superior physisorption onto nanoparticle surfaces which improved their dispersion stabilities.[24-26]

Exploration of the potential applications of *c*-PEG have also been reported by other groups, where *c*-PEGs were grafted onto nanoparticle surfaces to improve colloidal properties,[27] and conjugation with proteins[28] have been performed. However, most systems are only probed through differences in their macroscopic properties, and require a more detailed investigation to fully understand the impact of topology.

Small-angle scattering is a powerful and widely-used technique in the structural characterization of soft matter on the nanometer scale.[29, 30] It allows for an *in situ* structural analysis of matter due to its principal of measurement, where deflected signals from an collimated radiation are observed at small angles (0.1–10 º), upon interaction with a structure larger than the wavelength of the radiation.[31] The two major radiation sources are, X-rays and neutron beams, which corresponds to small-angle X-ray scattering (SAXS) and small-angle neutron scattering (SANS), respectively. While both SANS and SAXS allow detailed investigation of internal structures of scatterers, they interact with matter in different ways, where for instance, X-rays are scattered by the electron of the atoms, resulting in a mapping of the electron density distribution of the material. Thus, as a rule of thumb, atoms that have a large amount of electrons (heavier elements) scatter strongly, and will obscure scattering from lighter elements if both are present within the system. On the other hand, incident neutrons interact with the nuclei, which results in irregular scattering abilities of atoms in relation to the periodic table. Therefore, the lighter/heavier rule of elements observed for SAXS do not apply for SANS, and thus, they can be utilized to study composite matters that are made up of vastly differing elements.[32] Furthermore, due to the vastly differing scattering of H atoms and D atoms, scattering from the background can be controlled to eliminate/highlight certain components within the system, by simply mixing deuterated and non-deuterated samples to an appropriate ratio. This is called the contrast variation/matching method, and it has been found to be especially effective in the elucidation of multicomponent systems, such as block copolymer

micelles,[33, 34] polymer grafted nanoparticles of silica,[35, 36] polystyrene,[37, 38] and clay materials.[39] Naturally, SANS can be considered as a powerful method in elucidating the inorganic–organic hybrid structure of *c*-PEG and AuNPs (AuNPs/*c*-PEG) complexes. Available literature on other surface-functionalized AuNPs utilizing SANS, however, are mostly limited to small molecules,[40, 41] and only a single report has been made for PEGylated AuNPs using HS–PEG–OMe having a molecular weight of around 2 kDa.[42]

In this work, a detailed structural investigation using SAXS and SANS were carried out on both *c*-PEG and AuNPs/*c*-PEG complexes (Figure 4-0). Clear effects of chain confinement and topological excluded volume effect was observed from the molecular-weight dependency and solvent-dependency of the single chain dimensions and conformations of *c*-PEG. Meanwhile, a direct observation of the AuNPs/*c*-PEG complex structure was achieved for the first time through SANS measured in various $D_2O/H_2O$ solvent composition. Furthermore, model-independent and dependent analyses were conducted to quantitatively discuss the complex structure, where in comparison to terminally attached HS–PEG–OMe, *c*-PEGs were found to form a thinner adsorbed layer with smaller amount of molecules, indicating efficient coverage of the surface of AuNPs, realized through multiple interaction points of the mainchain with the nanoparticle surface.

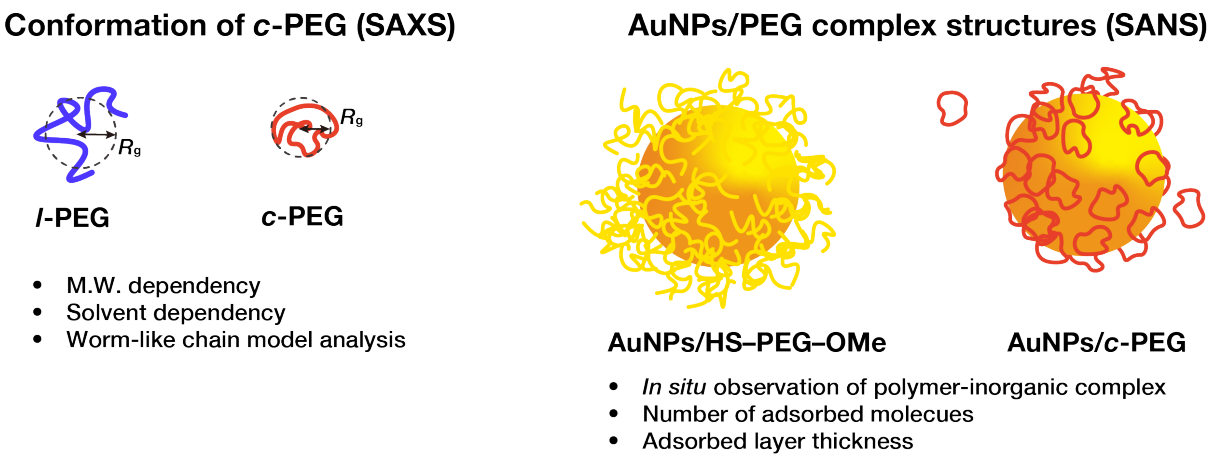


**Figure 4-0.** A schematic illustration of the targets and the scope of this work.

## 4.2. EXPERIMENTAL SECTION

### 4.2.1. Materials.

Gold nanoparticles (AuNPs) with a diameter of 30 nm (Gold Nanospheres, citrate, BioPure$^{TM}$, 1 mg/mL, nanoComposix), 4-toluenesulfonyl chloride (TsCl) (>98.0%, Junsei Chemical Co., Ltd.), sodium chloride (NaCl) (>99.0%, Kanto Chemical Co., Inc.), potassium hydroxide (KOH) (>85.5%, Kanto Chemical Co., Inc.), sodium sulfate ($Na_2SO_4$) (>99.0%, Kanto Chemical Co., Inc.), methanol (MeOH) (>99.5%, Kanto Chemical Co., Inc.), dichloromethane ($CH_2Cl_2$) (>99.0%, Kanto Chemical Co., Inc.) for the work up, chloroform ($CHCl_3$) (>99.0%, Kanto Chemical Co., Inc.), diethyl ether (>99.5%, Kanto Chemical Co., Inc.) for reprecipitation and benzene (>99.9%, Aldrich) for lyophilization were used as received. *n*-Hexane (>99.0%, Kanto Chemical Co., Inc.) was purified by distillation. Tetrahydrofuran (THF), dehydrated stabilizer free (>99.5%, Kanto Chemical Co., Inc.) and dehydrated dichloromethane ($CH_2Cl_2$) (>99.5%, Kanto Chemical Co., Inc.) for reactions were purified by a solvent purification system (MBRAUN MB-SPS-Compact). Deuterium oxide ($D_2O$) (>99.90%, Eurisotop), mPEG-SH (HS–PEG–OMe) (Biopharma PEG scientific Inc.) were used as received. Polyethylene glycol (HO–PEG–OH, further denoted as *l*-PEG) ($M_n$ ~2000, 4600, 10000, 20000 Aldrich) having terminal hydroxy groups were purified using preparative LCCC and reprecipitated in diethylether and lyophilized in benzene before use.

### 4.2.2. Size exclusion chromatography (SEC).

SEC was measured in DMF (containing 0.01 M LiCl) at 40 °C at the flow rate of 0.6 mL/min using a Jasco high performance liquid chromatography system (JASCO PU-980 Plus pump, JASCO RI-930 Intelligent RI detector, JASCO CO-965 Plus column oven and Shodex DEGAS KT-16) equipped with Shodex Asahipak GF-310 HQ column and a Shodex Asahipak GF-7 M HQ column.

### 4.2.3. Preparative SEC.

Preparative SEC was performed in $CHCl_3$ at the flow rate of 9 mL/min using a Japan Analytical Industry LC-7080 plus recycling preparative HPLC system (JAI RI-700LA detector) equipped with JAIGEL-2.5H and -3H columns and a pre-column connected in series.

### 4.2.4. Preparative liquid chromatography at the critical condition (LCCC).

Preparative scale LCCC was performed in a mixture of MeOH and MilliQ water (80/20 v/v) at the flow rate of 10 mL/min using a Japan Analytical Industry LC-5060 recycling preparative HPLC system (JAI RI-700LA detector) equipped with two reverse phase ODS columns (JAIGEL-ODS-AP SP-120-10) and a precolumn connected in series.

### 4.2.5. UV–Vis spectroscopy.

Ultraviolet–visible (UV–Vis) absorbance spectra were measured on a JASCO V-670 spectrophotometer at 25 °C using a micro quartz cell (M25-UV-2, GL Science Inc. Japan).

### 4.2.6. Synthesis of *c*-PEG.

Linear PEG having terminal hydroxy groups (*l*-PEG) was cyclized via etherification to form cyclic PEG (*c*-PEG) without inhomogeneity in the chemical structure by using the modified tosylation method according to previous reports.[17, 43] The molecular weight was 2, 4, and 10 and 19 kg/mol (namely, *c*-$PEG_{2k}$, *c*-$PEG_{4k}$, *c*-$PEG_{10k}$ and *c*-$PEG_{19k}$, respectively). Purification were conducted by fractionation using preparative scale SEC and LCCC, where the eluents were $CHCl_3$ and $MeOH/H_2O$ mixtures (80/20 vol/vol), respectively. Both *c*-PEG and *l*-PEG were reprecipitated in diethyl ether and lyophilized in benzene before use.

### 4.2.7. Preparation of polymer solutions for SAXS.

Stock solutions of *l*-PEG and *c*-PEG were prepared by dissolving required amounts of each polymer in their respective solvents (benzene, MilliQ water) and stirred at room temperature for over 24 h and filtered through a PTFE membrane filter unit (0.20 μm, Toyo Roshi Kaisha, Ltd.). Samples having various polymer concentrations were prepared by serial dilution of the stock solutions.

### 4.2.8. Preparation of AuNPs/PEG dispersions for SANS.

Typically, a PEG solution was prepared by dissolving 100 mg of *c*-$PEG_{10k}$ or HS–$PEG_{9k}$–OMe and 0.26 mg of sodium citrate in 5.0 mL of $H_2O$ or $D_2O$, and the solution was filtered through a 0.2 μm PTFE membrane. An AuNPs/PEG complex was prepared by mixing the PEG solution and 5 mL of 1 mg/mL aqueous dispersions of AuNPs having average particle diameters of 30 nm in a 0.2 mM sodium citrate solution. The mixture was vigorously mixed for 30 s using a vortex mixer and left standing at room temperature 12 h to attain adsorption equilibrium. The mixture was subjected to ultrafiltration at 2260 g for 15 min to an approximately 10-fold concentration, and a 0.2 mM sodium citrate $H_2O$ or $D_2O$ solution was added to re-dilute the mixture to its original concentration. The ultrafiltration and subsequent dilution were repeated three times to remove unadsorbed PEG, while at the same time, exchanging the solvent to attain the desired $D_2O/H_2O$ composition. The resulting dispersion was filtered using a 0.45 μm PTFE membrane filtration unit before undergoing the final ultrafiltration to obtain a concentrated dispersion of an AuNPs/PEG complex with an AuNPs concentration of approximately 7 mg/mL. The experimental concentration of AuNPs was determined from UV-vis absorption measurements by quantifying the absorbance intensity at the $\lambda_{max}$ of AuNPs (521 nm).

**4.2.9. Small-angle X-ray scattering (SAXS) measurements.**

SAXS measurements were performed at the beamline BL40B2 in SPring-8, Japan. The incident beam wavelength was set to 0.1 nm. A Pilatus3S 2M detector was placed 4.0 m from the sample, and ion chambers were placed in front and behind the sample to determine the X-ray transmittance. The measurement setup provided the $q$ range of 0.02–2.0 $nm^{-1}$, where $q$ is the magnitude of the scattering vector defined by $q = 4\pi/\lambda \sin(\theta)$, with the incident beam length denoted as $\lambda$, and the scattering angle of $2\theta$. The sample solutions were packed in a quartz capillary (2 mm Φ, Hilgenberg GmbH) and set in the sample chamber controlled by a INSTEC HCS-302 temperature control system to a temperature of 25.0 ºC. Sample solutions were measured at a beam exposure time of 6 min, and the resulting two-dimensional SAXS images was converted to one-dimensional $I(q)$ versus $q$ profiles via circular averaging. Here, $I(q)$ is the scattering intensity at $q$, and the background scattering from the solvent and the cell was subtracted to obtain the reduced excess scattering intensity ($\Delta I(q)$) of the sample using the following equation,

$$\Delta I(q) = \frac{I_{soln}(q)}{T_{soln} - T_{dark}} - \frac{I_{solv}(q)}{T_{solv} - T_{dark}} \qquad (1)$$

where $I_{soln}(q)$ and $I_{solv}(q)$ are the scattering intensity of the sample solution and the solvent, respectively, and the $T_{soln}$, $T_{solv}$ and $T_{dark}$ each represent the X-ray transmittance of the sample solution, solvent, and the background from the environment without any beam exposure, respectively. $\Delta I(q)$ was further corrected into absolute intensity values through the use of water (MilliQ water) as a secondary standard.[44]

**4.2.10. SANS measurement.**

SANS measurements were carried out at the BL15 beamline (TAIKAN) at J-PARC, Tokai, Japan and SANS-U (C1-2), JRR-3, Tokai, Japan.[45, 46] For TAIKAN, A time-of-flight method with a wavelength band from 1.0 to 7.5 Å was employed for the measurement, which resulted in a $q$-range of between 0.05 and 50 $nm^{-1}$, where $q$ is the magnitude of the scattering vector defined by $q = 4\pi/\lambda \sin(\theta)$, with the incident beam wavelength denoted as $\lambda$, and the scattering angle of $2\theta$. For SANS-U, a monochromatized neutron source with a wavelength of 7 Å and $^3$He position sensitive detector (PSD) (model 2660N, ORDELA) were used at sample-to-detector distances of 8 and 1 m, resulting in a $q$-range similar to that of TAIKAN. The measured two-dimensional SANS data were corrected for the instrumental background, empty cell and detector sensitivity, and converted to one-dimensional $I(q)$ versus $q$ profiles via circular averaging. Here, $I(q)$ was the total neutron scattering intensity at $q$, and the scattering from the background from the solvent and the quartz cell with a thickness of 1 mm was subtracted to obtain the reduced excess scattering intensity of the sample. The reduced excess scattering intensity was further corrected into absolute intensity values using glassy carbon (TAIKAN) or low-density polyethylene (SANS-U) as a secondary standard.[46, 47]

**4.2.11. SANS analysis.**

The total neutron scattering intensity, $I(q)$, from a dilute suspension of particle scatterers can be described using the below equation:

$$I(q) = c(\Delta b)^2 P(q) S(q) \qquad (2)$$

where $c$ is the number concentration of scatterers, $\Delta b$ is the excess neutron scattering length of a single scatterer, $P(q)$ is the form factor, $S(q)$ is the structure factor of the scatterers.[48] The excess neutron scattering length $\Delta b$ for a AuNPs/PEG complex is expressed as follows:

$$\Delta b = (\rho_{AuNPs} - \rho_{solvent}) V_{AuNP} + N(\rho_{PEG} - \rho_{solvent}) V_{PEG} \qquad (3)$$

where $\rho_{\text{AuNPs}}$, $\rho_{\text{solvent}}$ and $\rho_{\text{PEG}}$ are the scattering length densities (SLDs) of AuNPs, solvent and PEG, respectively. $V_{\text{AuNP}}$ and $V_{\text{PEG}}$ corresponds to the volume of a single AuNP and PEG molecule, and the number of adsorbed PEG molecules per a single AuNPs/PEG complex is denoted as $N$. For the case of AuNPs without PEG, only the first term of $\Delta b$ is considered. Scattering length densities (SLDs, $\rho$) of $H_2O$, $D_2O$, AuNPs, and PEG are summarized in Table S4-1. Scattering length data obtained from the NIST database was used for the calculation of SLDs.[49] Density values of the bulk materials were used to calculate $\rho_{\text{AuNPs}}$ and $\rho_{\text{solvent}}$, while the partial specific volume of linear PEG in aqueous solution[50] was used for the calculation of $\rho_{\text{PEG}}$. $V_{\text{AuNP}}$ and $V_{\text{PEG}}$ were calculated using the below equations:

$$V_{AuNP} = \pi r^2 \qquad (4)$$

$$V_{PEG} = \frac{\bar{\nu} M_{w,PEG}}{N_A} \qquad (5)$$

where $r$ is the radius of the sphere, $\bar{\nu}$ is the partial specific volume of PEG in aqueous solution, $M_{\text{w, PEG}}$ is the weight average molecular weight of PEG determined from SEC, and $N_{\text{A}}$ is the Avogadro's number. Since $M_{\text{w, }c\text{-PEG}}$ cannot be accurately determined using linear PEG standards, the molecular weight of the corresponding linear PEG ($M_{\text{w, }l\text{-PEG}}$) was used instead. $r$ was determined from a model fitting of SANS curve obtained for AuNPs without PEG in 0%

$D_2O$ using a spherical model, as described below.

In the model-independent Guinier analysis, the SANS curve in the low $q$ region can be approximated to the following equation:[48]

$$\lim_{q\to 0}\frac{I(q)}{c}=\frac{I(0)}{c}e^{\left(-\frac{1}{3}R_g q^2\right)} \qquad (6)$$

where $R_g$ is the radius of gyration. Thus, $R_g$ was calculated from a linear fitting of the Guinier plot ($\ln\{I(q)\}$ vs $q^2$).

For the model-dependent analysis of the SANS curves, a sphere model and a core–shell double sphere model were selected for the analysis of AuNPs and AuNPs/PEG complexes, respectively.[48] The form factor of a sphere having a radius of $r$ can be expressed by the following equation:

$$P(q)=[\Phi(qr)]^2 \qquad (7)$$

$$\Phi(x)=\frac{3[\sin x - x\cos x]}{x^3} \qquad (8)$$

while a core–shell type double sphere can be expressed as the following equation:

$$P(q)=\left[\frac{r_{\text{total}}^3\Phi(qr_{\text{total}})+f_{\text{r}}r_{\text{core}}^3\Phi(qr_{\text{core}})}{r_{\text{total}}^3+f_{\text{r}}r_{\text{core}}^3}\right]^2$$

$$f_{\text{r}}=(\rho_{\text{core}}-\rho_{\text{solv}})/(\rho_{\text{shell}}-\rho_{\text{solv}})-1 \qquad (9)$$

where, the radii of core and the whole double sphere are denoted as $r_{\text{core}}$ and $r_{\text{total}}$, while the SLDs of the core, shell and solvent are $\rho_{\text{core}}$, $\rho_{\text{shell}}$, and $\rho_{\text{solv}}$, respectively. The shell thickness ($d_{\text{shell}}$) can be calculated by the following equation:

$$d_{shell}=r_{total}-r_{core} \qquad (10)$$

using the two radii obtained from the fitting procedure. The sample concentrations in this study can be considered as a dilute system, where the structure factor $S(q)$ can be approximated as 1, and the model fitting analysis was conducted using a SASview program (ver 5.0.6). Finally, polydispersity (PD) in the radius was applied with a Schultz distribution[51] to account for the

size distributions of the scatterers, while instrument resolution is also taken into account in the fitting procedure.

## 4.3. RESULTS AND DISCUSSION

### 4.3.1. Synthesis and chromatographic separation of c-PEG.

Synthesis of cyclized PEG (*c*-PEG) having no chemical inhomogeneity in the polymer backbone was achieved through intramolecular cyclization of linear PEG (*l*-PEG) via the Williamson-ether synthesis of terminal hydroxy groups under high dilution, following previously reported methods (chapter 1).[17, 24] The "ring closure" strategy of linear polymers results in a mixture of intermolecularly reacted side products and unreacted material along with *c*-PEG. In order to observe the effect of cyclic topology onto the solution properties of PEG, it is of absolute necessity to remove all byproducts and unreacted linear materials in the system. For this goal, a two-step fractionation purification procedure was employed using (1) preparative scale size exclusion chromatography (SEC) to initially remove multimeric byproducts, followed by (2) liquid chromatography at the critical condition (LCCC) of PEG to completely isolate cyclized products from their linear precursors. SEC and LCCC traces of corresponding *l*-PEG and *c*-PEG after purification are shown in Figure 4-1 for the four molecular weight samples used in this study.

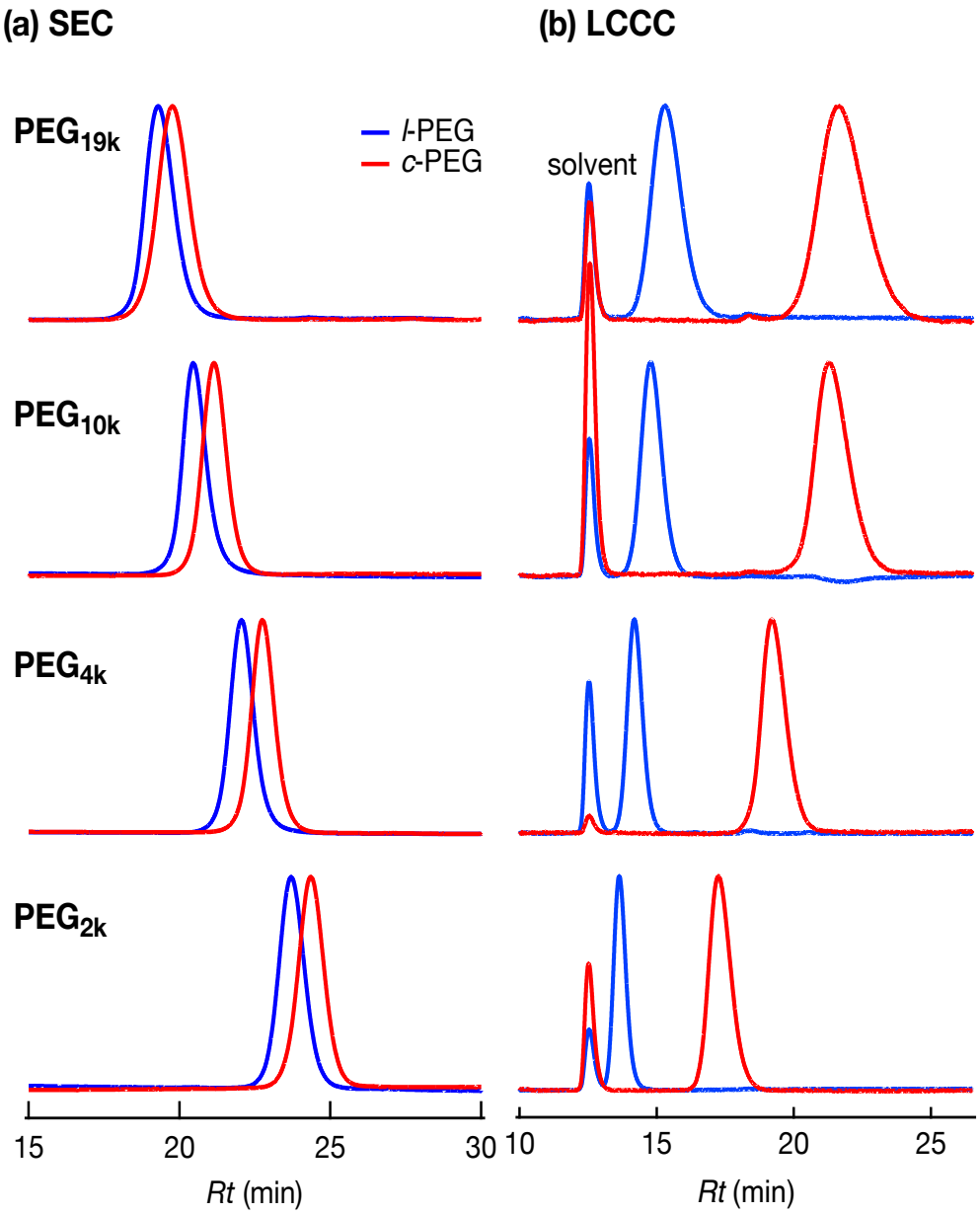


**Figure 4-1**. Normalized (a) SEC and (b) LCCC traces of purified *l*-PEG and *c*-PEG (Both from top; $PEG_{19k}$, $PEG_{10k}$, $PEG_{4k}$ and $PEG_{2k}$) . LCCC was measured in MeOH/$H_2O$ (80/20 v/v) mixtures using an ODS column.

As shown in the SEC traces of purified *l*-PEG and *c*-PEG (Figure 4-1 (a)), unimolecularly cyclized polymers displayed longer retention times compared to their corresponding linear counterparts due to their suppressed hydrodynamic volume, a property typically observed for cyclic/ring polymers.[1] However, a considerable overlap of SEC traces was observed between corresponding linear and cyclic species, indicating complete isolation of *c*-PEG purely via SEC fractionation to be challenging and inefficient.

The LCCC lies at a delicate transition point between the exclusion mode and the adsorption mode, where in principal, polymers of the same chemical structure coelute regardless of their molecular weights.[52] LCCC has been employed for the chromatographic separation of various polymers according to structural characteristics other than their molecular weight, such as terminal moieties,[53] block composition,[54] and polymer topology.[55] In this work, LCCC fractionation of *c*-PEG was conducted at a reported critical condition for *l*-PEG[54] on ODS columns, where the mobile phase was composed of MeOH/$H_2O$ mixture (80/20 v/v). Under this condition, *c*-PEG was found to elute significantly later than their linear counterparts and complete chromatographic separation was achieved for all four molecular weight samples used in this study (Figure 4-1 (b)). Furthermore, quantitative analysis of peak areas of LCCC traces of *c*-PEG measured by an RI detector revealed extremely high purities between 99.3–99.7%, thus confirming the efficacy of LCCC in the separation of PEG molecules based on their topology (Table 4-1).

**Table 4-1. SEC determined molecular weights of PEG[a] samples used in this study**

| Sample | $M_{n,\,SEC}$ (kg/mol) | $M_{w,\,SEC}$ (kg/mol) | $M_w/M_n$ | Purity (%)[b] |
|---|---|---|---|---|
| ***l*-PEG$_{2k}$** | 1.82 | 1.93 | 1.06 | - |
| ***c*-PEG$_{2k}$** | 1.29 | 1.36 | 1.06 | 99.5 |
| ***l*-PEG$_{4k}$** | 4.19 | 4.45 | 1.06 | - |
| ***c*-PEG$_{4k}$** | 2.96 | 3.11 | 1.05 | 99.3 |
| ***l*-PEG$_{10k}$** | 9.67 | 10.34 | 1.07 | - |
| ***c*-PEG$_{10k}$** | 6.89 | 7.28 | 1.06 | 99.7 |
| ***l*-PEG$_{19k}$** | 17.37 | 18.86 | 1.05 | - |
| ***c*-PEG$_{19k}$** | 14.01 | 15.17 | 1.08 | 99.7 |

[a] Molecular weights of *c*-PEG are only given as apparent values, due to the use of *l*-PEG standards for calculation.
[b] Purity of *c*-PEG was determined from the peak areas of the LCCC traces.

### 4.3.2. Small-angle X-ray scattering (SAXS) of PEG solutions.

The extremely high purity of the *c*-PEG samples (99.3–99.7%) enabled the rigorous investigation of the effect of polymer topology on the chain dimensions and conformations of PEG in dilute solution, through synchrotron SAXS measurements. Sample solutions were prepared in two known good solvents of PEG,[56, 57] benzene and water in order to investigate the impact of solvent quality on these properties.

The reduced excess scattering intensity $\Delta I(q)$, obtained after circular averaging of 2D SAXS images and appropriate data reduction was normalized to the concentration of PEG ($c_{PEG}$) and extrapolated to $c_{PEG} \rightarrow 0$ using the Berry square-root plots. The extrapolated values can be expressed by the following equation,

$$\left[\frac{\Delta I(q)}{K c_{PEG}}\right]^{-1/2}_{c_{PEG}\rightarrow 0} = \frac{1}{\sqrt{x_w}}\left[1 + \frac{1}{6}\langle S^2\rangle q^2 + \mathcal{O}(q^4)\right] = \frac{1}{\sqrt{x_w}} P(q)^{-1/2} \qquad (11)$$

where $K$ is the scattering constant, $x_w$ is the weight-average degree of polymerization, $\langle S^2\rangle$ is the mean-square radius of gyration, and $P(q)$ is the particle scattering function. Values of $x_w$ were calculated from the $M_w$ of *l*-PEG using SEC data (Table 4-1), while $x_w$ of *c*-PEGs were assumed to be identical to their linear precursor based on the ring-closure approach and lack of accurate method to independently determine the molecular weights of *c*-PEG using SEC. Representative Berry plots taken in benzene and water at finite concentrations and $c_{PEG} \rightarrow 0$ extrapolated conditions for *l*-PEG$_{10k}$ and *c*-PEG$_{10k}$ ($x_w$ = 235) are shown in Figure 4-1, while corresponding plots for the other molecular weights are shown in Figure S4-1 and S4-2.

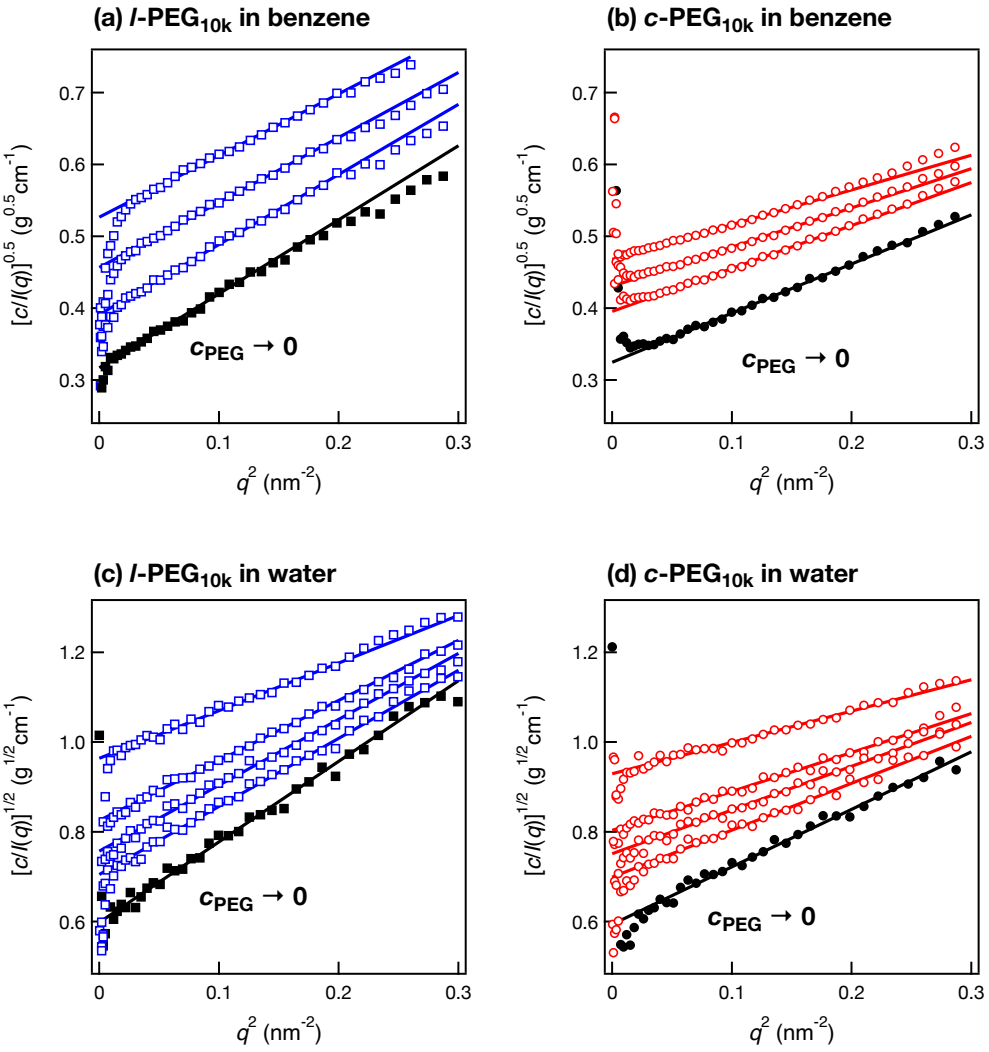


**Figure 4-2**. Berry plots of (a) *l*-PEG$_{10k}$ and (b) *c*-PEG$_{10k}$ in benzene, and (c) *l*-PEG$_{10k}$ and (d) *c*-PEG$_{10k}$ in water. Data points of finite concentrations are shown in color, while $c_{PEG} \rightarrow 0$ extrapolated values are shown in black. For samples measured in benzene, $c_{PEG}$ = 2, 0.15 and 0.1 wt% (from top), while for samples measured in water, $c_{PEG}$ = 3, 2, 0.15 and 0.1 wt% (from top), respectively.

Radius of gyration $\langle S^2 \rangle^{1/2}$ calculated from the initial slope of the Berry plots, alongside the geometric shrinking factor denoted as $g_s$ (= $\langle S^2 \rangle_{cyclic}/\langle S^2 \rangle_{linear}$) are summarized in Table 4-2.

**Table 4-2. $\langle S^2 \rangle^{1/2}$ and $g_s$ values of *l*-PEG and *c*-PEG in benzene and water determined from Berry plots**

| Sample | $x_w$[a] | Benzene | | Water | |
|---|---|---|---|---|---|
| | | $\langle S^2 \rangle^{1/2}$ (nm) | $g_s$ | $\langle S^2 \rangle^{1/2}$ (nm) | $g_s$ |
| ***l*-PEG$_{2k}$** | 44 | 1.68 ± 0.01 | 0.64 | 1.70 ± 0.02 | 0.60 |
| ***c*-PEG$_{2k}$** | | 1.34 ± 0.02 | | 1.31 ± 0.01 | |
| ***l*-PEG$_{4k}$** | 101 | 2.80 ± 0.02 | 0.62 | 2.65 ± 0.07 | 0.70 |
| ***c*-PEG$_{4k}$** | | 2.21 ± 0.02 | | 2.22 ± 0.03 | |
| ***l*-PEG$_{10k}$** | 235 | 4.42 ± 0.07 | 0.65 | 4.24 ± 0.05 | 0.72 |
| ***c*-PEG$_{10k}$** | | 3.56 ± 0.03 | | 3.60 ± 0.04 | |
| ***l*-PEG$_{19k}$** | 429 | 6.36 ± 0.04 | 0.65 | 6.23 ± 0.14 | 0.68 |
| ***c*-PEG$_{19k}$** | | 5.12 ± 0.04 | | 5.13 ± 0.05 | |

[a] Weight-average degree of polymerization ($x_w$) was calculated using $M_w$ of *l*-PEGs. The $x_w$ values of c-PEGs were assumed to be identical to their linear precursors based on the ring-closure approach of cyclization.

Furthermore, solvent quality of benzene and water can be estimated from the Flory exponent parameter ($v$), which describes the scaling of chain size ($<S^2>^{1/2}$) with degree of polymerization ($x_w$) through the following equation:

$$\log\langle S^2\rangle^{1/2} \propto v \log x_w \qquad (12)$$

Double logarithmic plots of $<S^2>^{1/2}$ and $x_w$ for benzene and water are shown in Figure 4-3, and the $v$ determined from the slope of the linear fit is annotated within each graph.

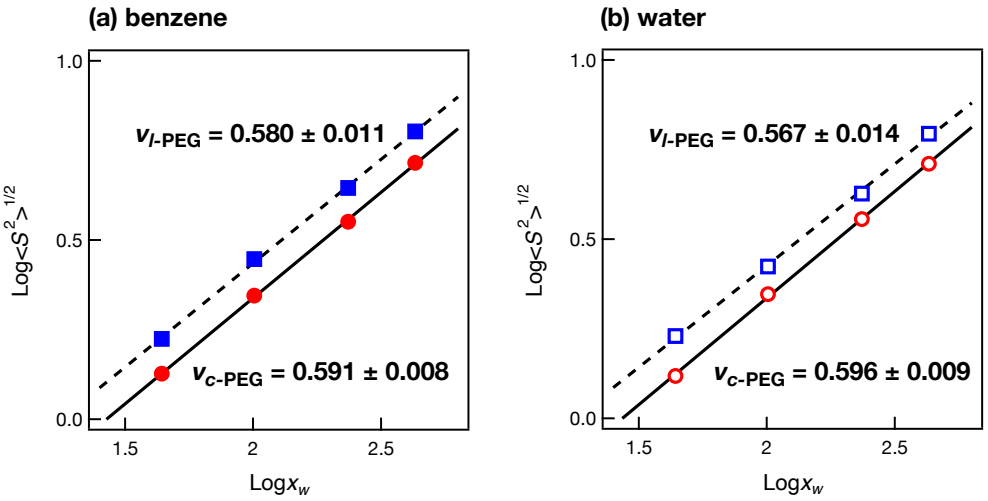


**Figure 4-3**. Double logarithmic plots of $x_w$ and $<S^2>^{1/2}$ for *l*-PEG and *c*-PEG in (a) benzene and (b) water. Flory exponents ($v$) calculated from the slopes of the linear fit curves are shown in the annotation. Errors of $<S^2>^{1/2}$ were smaller than the sizes of the symbols.

$<S^2>^{1/2}$ values of *c*-PEGs were evidently smaller to their corresponding values of HO–PEG–OH in both solvents. For example, $<S^2>^{1/2}$ of *l*-PEG$_{10k}$ and *c*-PEG$_{10k}$ were 4.42 and 3.56 nm in benzene, while for the same samples in water, $<S^2>^{1/2}$ were 4.24 and 3.60 nm, respectively. This led to $g_s$ values of 0.62–0.65 in benzene, and larger values in the range of 0.60–0.72 for samples in water. For ideal Gaussian chains, the theoretical $g_s$ of cyclic polymers are known to be 0.50.[58] However, computational and experimental studies have shown the $g_s$ of cyclic polymers to generally display values larger than 0.5, with largest reported values obtained from SANS experiments of cyclic polystyrene in the range of 0.557–0.730.[14] The large deviance of $g_s$ expected from ideal chains is attributed to the "topological expansion/swelling effect", where cyclic polymers experience strong intramolecular excluded-volume effect due to their topological constraint. Since the amount of linear contaminants that may contribute to an apparent increase in $g_s$ is minimal (less than 0.7%) in this work, the relatively large $g_s$ is expected to be of the same origin. It is noteworthy of mention that the experimentally determined values of $<S^2>^{1/2}$ for both *l*-PEG and *c*-PEG are significantly larger than those predicted from a recent computational study.[21]

Next, discrepancies between $g_s$ values obtained in benzene and water were considered from the assessment of solvent quality, using the Flory exponent ($\nu$). Theoretical values of $\nu$ for ideal Gaussian chains are 0.50, while in good solvents, expansion of the coils result in $\nu$ = 0.60.[59] In general, the experimental $\nu$ obtained in this work are all well above 0.50, confirming good solvent properties of both benzene and water. However, comparison of $\nu$ for *l*-PEG revealed clearly larger values in benzene (0.580 ± 0.011) compared to in water (0.567 ± 0.014), indicating the former to be a better solvent for *l*-PEG. Difference in solvent quality was also reflected in the chain dimensions of *l*-PEG, where generally, larger $<S^2>^{1/2}$ were obtained in benzene. On the other hand, relatively larger, and similar values of $\nu$ were calculated for *c*-PEG (in benzene; 0.591 ± 0.008 and in water; 0.596 ± 0.009, respectively). Along with the almost

identical values of $<S^2>^{1/2}$ of *c*-PEG in benzene and water, an apparent independency to solvent quality is indicated. This again can be attributed to a strong topological excluded-volume effect, which contributes to the swelling of the ring and consequently, resists chain collapse. Similar nonmonotonic trends in $\nu$ on solvent quality were reported by Gartner *et al* through computational simulations,[60] albeit near the theta condition. Thus, the significantly larger $g_s$ values obtained in water was attributed to the marked decrease in chain dimensions of *l*-PEG in response to a relatively worsened solvent quality, which was suppressed for *c*-PEG, due to their strong topological excluded-volume effect.

Finally, a quantitative analysis of the $P(q)$ of *l*-PEG and *c*-PEG was conducted using a theoretical scattering function of the Kratky–Porod worm-like chain model[61] and Kratky–Porod worm-like ring model,[62] respectively. Effect of chain thickness was taken into account by using the touched–bead model.[63, 64] Kratky plots ($q^2P(q)$ vs $q$) of *l*-PEG and *c*-PEG obtained in benzene and water, along with their calculated curves are shown in Figure 4-4. Best fit parameters of the theoretical curves and their calculated $<S^2>^{1/2}_{KP}$ are summarized in Table 4-3 and 4-4.

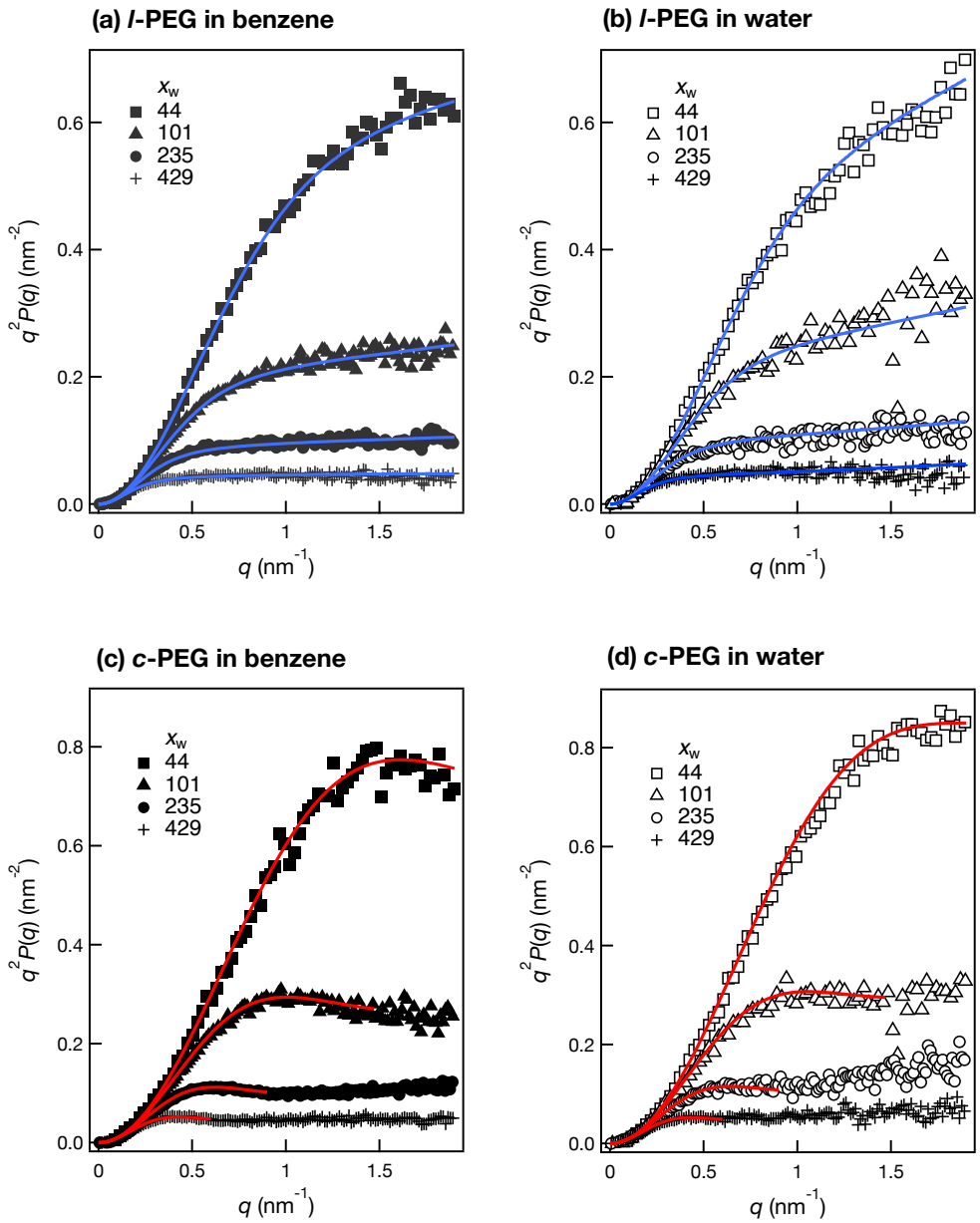


**Figure 4-4**. Kratky plots of *l*-PEG in (a) benzene and (b) water, and *c*-PEG in (c) benzene and (d) water. Theoretical curves using the KP worm-like chain model and worm-like ring model are shown as continuous lines.

**Table 4-3. Theoretical parameters of the KP worm-like chain (WLC) model used to describe *l*-PEG**

| Sample | $L_w$ (nm) | benzene | | | water | | |
|---|---|---|---|---|---|---|---|
| | | $\lambda^{-1}$ (nm) | $d_b$ (nm) | $<S^2>^{1/2}_{WLC}$ (nm) | $\lambda^{-1}$ (nm) | $d_b$ [a] (nm) | $<S^2>^{1/2}_{WLC}$ (nm) |
| ***l*-PEG$_{2k}$** | 12.3 | 1.6 | 0.7 | 1.65 | 1.7 | (0) | 1.69 |
| ***l*-PEG$_{4k}$** | 28.3 | 1.9 | 0.8 | 2.85 | 1.6 | (0) | 2.63 |
| ***l*-PEG$_{10k}$** | 65.8 | 1.9 | 0.9 | 4.47 | 1.7 | (0) | 4.24 |
| ***l*-PEG$_{19k}$** | 120 | 2.2 | 1.2 | 6.54 | 2.1 | (0) | 6.4 |

[a] Theoretical models of infinitely thin WLC were used to reflect upturns in the high-$q$ region of the Kratky plots obtained in water.

**Table 4-4. Theoretical parameters of the KP worm-like ring (WLR) model used to describe *c*-PEG**

| Sample | $L_w$ (nm) | benzene | | | water | | |
|---|---|---|---|---|---|---|---|
| | | $\lambda^{-1}$ (nm) | $d_b$ (nm) | $<S^2>^{1/2}_{WLR}$ (nm) | $\lambda^{-1}$ (nm) | $d_b$ [a] (nm) | $<S^2>^{1/2}_{WLR}$ (nm) |
| ***c*-PEG$_{2k}$** | 12.3 | 1.7 | 0.8 | 1.20 | 1.7 | (0) | 1.20 |
| ***c*-PEG$_{4k}$** | 28.3 | 1.9 | 0.9 | 2.03 | 1.9 | (0) | 2.03 |
| ***c*-PEG$_{10k}$** | 65.8 | 2.1 | 1.2 | 3.33 | 2.1 | (0) | 3.33 |
| ***c*-PEG$_{19k}$** | 120 | 2.5 | 1.2 | 4.94 | 2.5 | (0) | 4.94 |

[a] Theoretical models of infinitely thin WLR were used to reflect upturns in the high-$q$ region of the Kratky plots obtained in water.

If I apply the $x_w$ values determined from SEC and assume the length per repeating unit ($l_m$) to be the same as those reported by Kawaguchi *et al*. ($l_m$ = 0.28 nm),[65, 66] the weight-average contour length ($L_w$) is determined as 12.3, 28.3, 65.8, and 120 nm for PEG of $M_w$ = 2, 4, 10 and 19 kg mol$^{-1}$, respectively. Using these values, the Kuhn segment length ($\lambda^{-1}$) for HO–PEG–OH in benzene were determined to be $\lambda^{-1}$ = 1.6, 1.9, 1.9, and 2.2 nm for $M_w$ = 2, 4, 10 and 20 kg mol$^{-1}$, respectively. For HO–PEG–OH in water, slightly different $\lambda^{-1}$ values (1.7, 1.6, 1.7, and 2.1 nm for $M_w$ = 2, 4, 10 and 19 kg mol$^{-1}$) were used to represent experimental results, indicating influences of both molecular weight and solvent on these values. The $\lambda^{-1}$ values for HO–PEG–OH in water are in excellent agreement with a recent SANS and SAXS study on linear PEG ($M_w$ = 8.1 kg mol$^{-1}$), where the $\lambda^{-1}$ was determined to be 1.7 nm.[50] Moreover, it was shown that the excluded-volume effect could be fairly well represented by the use of an effective stiffness parameter $\lambda^{-1}_{eff}$ that was larger than the actual $\lambda^{-1}$, when using an theoretical KP worm-like chain model using the Yoshizaki–Yamakawa equation.[61, 67] Taking this into account, the relatively larger $\lambda^{-1}$ values obtained for longer HO–PEG–OH, and the generally larger $\lambda^{-1}$ values obtained in benzene compared to water could be interpreted as the manifestation of an increase in intramolecular excluded-volume effect.

For *c*-PEGs, theoretical values of $\lambda^{-1}$ = 1.7, 1.9, 2.1, and 2.5 nm for $M_w$ = 2, 4, 10 and 19 kg mol$^{-1}$ were determined to fit experimental data taken in both benzene and water. The relatively large $\lambda^{-1}$ of *c*-PEGs compared to those of corresponding HO–PEG–OHs, along with a significantly increased $\lambda^{-1}$ for larger $M_w$ indicate a more prominent effect of intramolecular excluded-volume to be experienced for *c*-PEG, which is further pronounced upon an increase in $x_w$. Meanwhile, the apparent independency of $\lambda^{-1}$ against solvent quality is in coincidence with the observations made from comparison of $<S^2>^{1/2}$, $g_s$ and $\nu$, which further supports indication of their topological origin.

The plateau in the high-$q$ region of the Kratky plots taken in benzene were represented

by introducing the bead diameter ($d_b$) of the touched bead model. Values of $d_b$ = 0.7–1.2 nm were found for both HO–PEG–OH and *c*-PEG, in fairly well coincidence with a previous report.[50] Kratky plots of HO–PEG–OH and *c*-PEG obtained in water, however, showed an upturn in the high-$q$ region, where experimental plots were most well represented by using infinitely thin ($d_b$ = 0) worm-like chains and rings. This can be explained by the influence of heterogeneity of the excess-electron-density in the chain on the $P(q)$, when the electron density of the polymer is close to that of the solvent.[50, 68] However, within the experimental $q$-range of this study, the effect of chain thickness was deemed to be negligible on the determination of $\lambda^{-1}$. Incidentally, the calculated values of $<S^2>^{1/2}_{KP}$ were in good agreement (within ± 10% error) with $<S^2>^{1/2}$ obtained from Berry plots for all samples measured in this study.

### 4.3.3. SANS measurements of AuNPs/*c*-PEG and AuNPs/HS–PEG–OMe complexes

For SANS measurements, a concentrated $AuNPs_{30}$ dispersion (1.0 mg/mL) was mixed with an equal volume of a PEG solution (20 mg/mL) and subjected to four sets of ultrafiltration and dilution through a similar preparation procedure to that employed for the NMR measurements. Structural differences of $AuNPs_{30}$ without PEG, $AuNPs_{30}$/*l*-$PEG_{10k}$, $AuNPs_{30}$/HS–$PEG_{9k}$–OMe, and $AuNPs_{30}$/*c*-$PEG_{10k}$ were compared through analysis of SANS curves obtained in mixtures of $D_2O$ and $H_2O$ with various compositions. SANS curves obtained for $AuNPs_{30}$, $AuNPs_{30}$/HS–$PEG_{9k}$–OMe, and $AuNPs_{30}$/*c*-$PEG_{10k}$ in $D_2O/H_2O$ mixtures are shown in Figure 4-5, with $D_2O$ volume compositions of 0%, 100%, and 70%, where 70% $D_2O$ is the contrast matching condition for gold. Each data converted to an absolute scale was normalized based on the number concentration of AuNPs (*c*) determined from UV–vis absorption measurements, thereby enabling direct comparison of scattering contribution from the PEG shell.

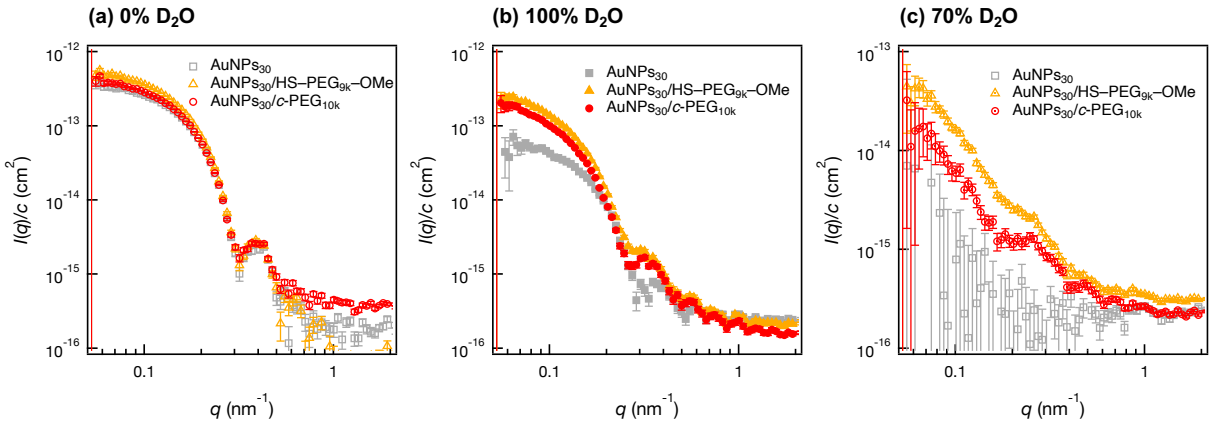


**Figure 4-5**. SANS curves for $AuNPs_{30}$, $AuNPs_{30}$/HS–$PEG_{9k}$–OMe and $AuNPs_{30}$/*c*-$PEG_{10k}$ in (a) 0% $D_2O$, (b) 100% $D_2O$, and (c) 70% $D_2O$. The curves are normalized by the number concentration of AuNPs. 70% $D_2O$ is the contrast matching condition for gold.

SANS measurement in 0% $D_2O$ resulted in similar curve shapes and intensities for all three $AuNPs_{30}$, $AuNPs_{30}$/HS–$PEG_{9k}$–OMe, and $AuNPs_{30}$/*c*-$PEG_{10k}$ (Figure 4-5 (a)). This was due to minimal scattering contributions from the PEG layer, arising from the similar scattering length density (SLD) values of PEG ($0.69 \times 10^{10}$ $cm^{-2}$) and $H_2O$ ($-0.56 \times 10^{10}$ $cm^{-2}$) compared with SLD for gold ($4.66 \times 10^{10}$ $cm^{-2}$). Thus, the SANS curve shapes in this condition were governed almost exclusively by the AuNPs core. All three samples displayed SANS curves typically observed for noninteracting spherical particles, which indicated no aggregation of AuNPs to occur during sample preparation. On the other hand, a clear distinction can be made upon a comparison of the three scattering curves of $AuNPs_{30}$, $AuNPs_{30}$/HS–$PEG_{9k}$–OMe, and $AuNPs_{30}$/*c*-$PEG_{10k}$ in 100% $D_2O$ (Figure 4-5 (b)), where scattering from both of the gold core and PEG shell contributed to the total SANS curves. A prominent increase in scattering intensity was observed in the low $q$ region (0.06–0.2 $nm^{-1}$) for both $AuNPs_{30}$/HS–$PEG_{9k}$–OMe and $AuNPs_{30}$/*c*-$PEG_{10k}$, compared to that of $AuNPs_{30}$. In addition, the position of the first oscillation maximum for each SANS curve was shifted from around 0.35 $nm^{-1}$ for $AuNPs_{30}$ to 0.30 $nm^{-1}$ for $AuNPs_{30}$/HS–$PEG_{9k}$–OMe and to 0.32 $nm^{-1}$ for $AuNPs_{30}$/*c*-$PEG_{10k}$. Since the

SANS intensity was normalized by the number concentrations of AuNPs, the shift of the oscillation position towards lower $q$ values for the AuNPs/PEG complexes indicated a larger scatterer size, while the increased scattering intensity in the low $q$ region reflected the amount of adsorbed PEG molecules as a consequence of complex formation. For $AuNPs_{30}$/*l*-$PEG_{10k}$ after the same ultrafiltration procedure, on the other hand, the obtained SANS curve in 100% $D_2O$ was found to be almost identical to that of $AuNPs_{30}$ (Figure S4-3), indicating no presence of an adsorbed shell of *l*-$PEG_{10k}$ after ultrafiltration, further corroborating the distinct surface adsorbing property of *c*-PEG.

Furthermore, a solvent contrast-matching technique for the gold core was used to extract structural information from the PEG shell.[30] The vastly different SLD values of $D_2O$ ($6.39 \times 10^{10}$ $cm^{-2}$) and $H_2O$ ($-0.56 \times 10^{10}$ $cm^{-2}$) conveniently allow for the elimination of scattering contribution from materials that have SLD values between the two by mixing $D_2O$ and $H_2O$ at an appropriate composition. In the case of AuNPs, the SLD matching condition was experimentally achieved at 70% $D_2O$ composition, where the SANS curve of $AuNPs_{30}$ completely matched that of the solvent (Figure S4-4). Thus, the relatively weak but clear SANS curves obtained for $AuNPs_{30}$/HS–$PEG_{9k}$–OMe and $AuNPs_{30}$/*c*-$PEG_{10k}$ in 70% $D_2O$ solely reflect structural information from the adsorbed PEG layer (Figure 4-5 (c)). Scattering contribution from unadsorbed HS–$PEG_{9k}$–OMe or *c*-$PEG_{10k}$ was also considered to be negligible due to the preparation method, where extensive solvent exchange via ultrafiltration was conducted to remove excess the PEG molecules. Dissimilarity of the SANS curves of *c*-PEG and HS–PEG–OMe dissolved in 100% and 70% $D_2O$ (10 mg/mL) to those of the complexes also support this assumption (Figure S4-5). The obtained results unambiguously confirmed the direct observation of the adsorbed PEG layer onto the AuNPs surface for both HS–$PEG_{9k}$–OMe and *c*-$PEG_{10k}$.

In order to extract quantitative structural characteristics of the AuNPs/PEG complexes from the SANS scattering data obtained in various $D_2O$ compositions, a combined structural analysis using model-independent and dependent methods were carried out. First, a model-independent Guinier analysis was performed through linear fitting of $\ln\{I(q)/c\}$ vs. $q^2$ curves to obtain the radius of gyration ($R_{g,Guinier}$) of the scatterers (Figure 4-6). $R_{g,Guinier}$ of each scatterer in 0%, 100% and 70% $D_2O$ is summarized in Table 4-5.

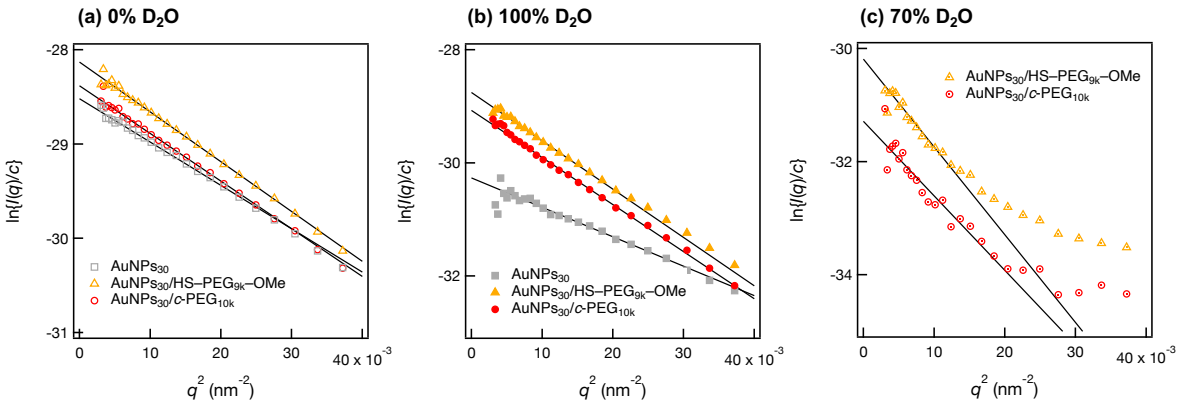


**Figure 4-6**. Guinier analysis results for $AuNPs_{30}$, $AuNPs_{30}$/HS–$PEG_{9k}$–OMe and $AuNPs_{30}$/*c*-$PEG_{10k}$ in (a) 0% $D_2O$ and (b) 100% $D_2O$ and (c) 70% $D_2O$. Linear fits of the low $q$ region are shown as continuous lines.

**Table 4-5. $R_g$ determined from Guinier analysis of $AuNPs_{30}$, $AuNPs_{30}$/*c*-$PEG_{10k}$, and AuNPs/HS–$PEG_{9k}$–OMe in 0%, 100% and 70% $D_2O$**

| | $R_{g,\,Guinier}$ (nm) | | | $N_{Guinier}$ (PEG molecules /AuNP) |
|---|---|---|---|---|
| $D_2O$ content (%) | 0 | 100 | 70 | 70 |
| $AuNPs_{30}$ | 11.7 ± 0.1 | 12.5 ± 0.2 | - | - |
| AuNPs/HS–$PEG_{9k}$–OMe | 12.6 ± 0.1 | 16.0 ± 0.2 | 21.6 ± 0.5 | 540 ± 20 |
| $AuNPs_{30}$/*c*-$PEG_{10k}$ | 12.3 ± 0.1 | 15.8 ± 0.1 | 19.9 ± 0.6 | 290 ± 10 |

In accordance with the initial qualitative analysis, similar $R_{g,Guinier}$ values of around 12 nm were obtained in 0% $D_2O$ for all $AuNPs_{30}$, $AuNPs_{30}$/HS–$PEG_{9k}$–OMe and $AuNPs_{30}$/*c*-$PEG_{10k}$ due to the minimal scattering contrast of PEG in this solvent composition. On the other hand, in 100% $D_2O$, an evident increase in $R_{g,Guinier}$ was observed for $AuNPs_{30}$/HS–$PEG_{9k}$–OMe (16.0 ± 0.2 nm) and $AuNPs_{30}$/*c*-$PEG_{10k}$ (15.8 ± 0.1 nm) from that of $AuNPs_{30}$ (12.5 ± 0.2 nm). Given that the $R_{g,Berry}$ of molecularly dissolved *l*-$PEG_{10k}$ (which has a similar molecular weight to HS–$PEG_{9k}$–OMe) and *c*-$PEG_{10k}$ in water from SAXS measurements were calculated to be 4.24 ± 0.05 and 3.60 ± 0.04 nm (Table 4-2), respectively, the increase in size for the AuNPs/PEG complexes in $D_2O$ 100% suggested the PEG shells to be likely comprised of a single adsorption layer. Interestingly, Guinier analysis for AuNPs/PEG complexes in 70% $D_2O$ resulted in the largest values of $R_g$: 21.6 ± 0.5 and 19.9 ± 0.6 nm for $AuNPs_{30}$/HS–$PEG_{9k}$–OMe and $AuNPs_{30}$/*c*-$PEG_{10k}$, respectively. This was probably due to the elimination of the scattering contributions from the AuNPs core in the gold contrast-matched condition, thereby depicting a more accurate representation of the PEG shell. Furthermore, the total neutron scattering $I(q)$ can be expressed as a product of the number concentration of the scatterer ($c$), form factor ($P(q)$) and the excess neutron scattering length ($\Delta b$). In this solvent composition, $\Delta b$ can be expressed as the sum of excess scattering length from adsorbed PEG chains as shown below:

$$\Delta b = N(\rho_{PEG} - \rho_{solvent})V_{PEG} \qquad (13)$$

where $\rho_{PEG}$ and $\rho_{solvent}$ are SLD of PEG and solvent, respectively, $V_{PEG}$ is the volume of a single PEG molecule, and $N$ is the number of adsorbed PEG molecules per a single AuNPs/PEG complex. Thus, $N$ can be obtained by the $q \rightarrow 0$ extrapolation of the $I(q)/c$ using the following equation:

$$\lim_{q\to 0} \frac{I(q)}{c} = N^2(\rho_{PEG} - \rho_{solvent})^2 {V_{PEG}}^2 \qquad (14)$$

$V_{PEG}$ for HS–$PEG_{9k}$–OMe ($1.30 \times 10^{-20}$ $cm^3$) and *c*-$PEG_{10k}$ ($1.41 \times 10^{-20}$ $cm^3$) were calculated from a literature value of the partial specific volume of PEG in aqueous solution (0.824 $cm^3$ $g^{-1}$)[50] and their weight-average molecular weights (Table 4-1). Finally, an approximated $N$ (denoted as $N_{Guinier}$) was determined through the Guinier analysis for $AuNPs_{30}$/HS–$PEG_{9k}$–OMe and $AuNPs_{30}$/*c*-$PEG_{10k}$ in 70% $D_2O$ to give $N_{Guinier} = 540 \pm 20$ and $290 \pm 10$, respectively (Table 4-5). $N_{Guinier} = 290 \pm 10$ obtained from SANS of $AuNPs_{30}$/*c*-$PEG_{10k}$ was further used to calculate the adsorption density of $\sigma_{Guinier}$ to be 0.10 molecules/$nm^2$ and the occupied area per single PEG molecule $S_{Guinier}$ to be 9.9 $nm^2$. Similarly, $N_{Guinier} = 540 \pm 20$ for $AuNPs_{30}$/HS–$PEG_{9k}$–OMe corresponds to $\sigma_{Guinier} = 0.19$ molecules/$nm^2$ and $S_{Guinier} = 5.2$ $nm^2$, all of which points to a denser PEG adsorbed layer to be formed upon the adsorption of HS–$PEG_{9k}$–OMe molecules.

A model-fitting of the scattering curves was further conducted in an attempt to describe the AuNPs/PEG structure over the whole experimental $q$-range of the SANS curves. A theoretical model for a solid sphere was selected for $AuNPs_{30}$ while a core-shell sphere model was used to fit the SANS curves of AuNPs/HS–$PEG_{9k}$–OMe and $AuNPs_{30}$/*c*-$PEG_{10k}$. In order to reduce the number of fitting parameters of the AuNPs/PEG complexes, the radius of the core ($r_{core}$) and their size distribution were expressed in terms of a polydispersity parameter ($PD_{AuNPs}$) were constrained to the average values obtained from the fitting of $AuNPs_{30}$ in 0% and 100% $D_2O$. SLDs of the AuNP core ($\rho_{core}$) and solvent ($\rho_{solv}$) were set to calculated values (Table S4-1),[49, 69] while those for the PEG shells ($\rho_{shell}$) were calculated using pre-determined values of $\rho_{PEG}$ and $V_{PEG}$ by the following equation:

$$\frac{4\pi}{3}(r_{total}^3 - r_{core}{}^3)(\rho_{\text{shell}} - \rho_{\text{solv}}) = N_{model}(\rho_{PEG} - \rho_{solvent})V_{PEG} \qquad (15)$$

where $r_{total}$ is the radius of the whole core-shell sphere and $N_{model}$ is the number of adsorbed PEG molecules, obtained from the fitting procedure. Furthermore, the amount of solvent

contained within the shell ($x$) is calculated from the SLD values of the shell, PEG and solvent as follows:

$$x\ (\%) = \frac{\rho_{shell} - \rho_{PEG}}{\rho_{solvent} - \rho_{PEG}} \times 100 \qquad (16)$$

Fitting curves are shown in Figure 4-7 and their calculated parameters are summarized in Table 4-6.

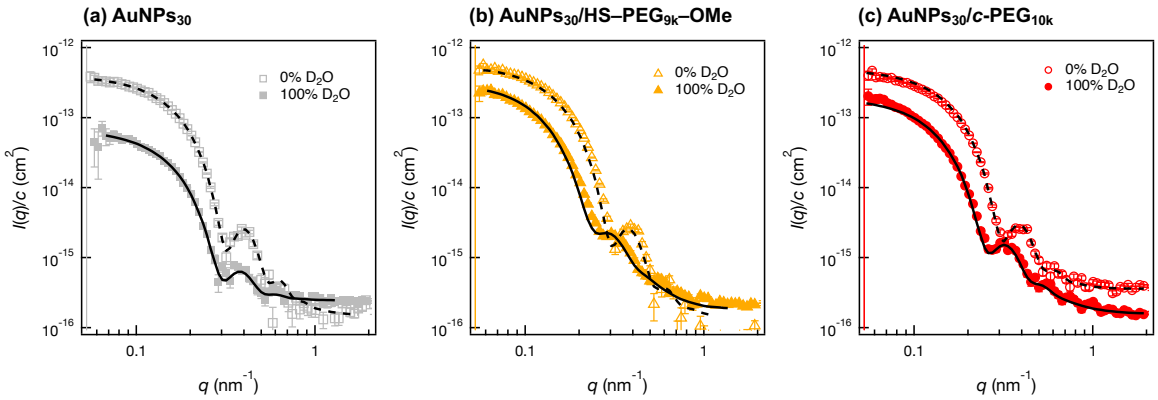


**Figure 4-7.** Model-dependent fitting for (a) $AuNPs_{30}$, (b) $AuNPs_{30}$/HS–$PEG_{9k}$–OMe and (c) $AuNPs_{30}$/*c*-$PEG_{10k}$ in 0% $D_2O$ and 100% $D_2O$. Theoretical curves in 0% and 100% $D_2O$ are shown as continuous and broken lines, respectively.

**Table 4-6. Fitting parameters of model-dependent SANS analysis of $AuNPs_{30}$, $AuNPs_{30}$/*c*-$PEG_{10k}$ and AuNPs/HS–$PEG_{9k}$–OMe in 0% and 100% $D_2O$.**

| | $AuNPs_{30}$ | | $AuNPs_{30}$/*c*-$PEG_{10k}$ | | AuNPs/HS–$PEG_{9k}$–OMe | |
|---|---|---|---|---|---|---|
| $D_2O$ composition (%) | 0 | 100 | 0 | 100 | 0 | 100 |
| $c$ ( $\times 10^{13}$ $cm^{-3}$) | 2.37 | 2.86 | 2.79 | 2.83 | 2.39 | 2.67 |
| $r$ (= $r_{core}$) (nm)[a] | 14.1 | 14.6 | (14.4) | (14.4) | (14.4) | (14.4) |
| $PD_{AuNPs}$[a] | 0.07 | 0.09 | (0.08) | (0.08) | (0.08) | (0.08) |
| $\rho_{shell}$ ( $\times 10^{10}$ $cm^{-2}$) | - | - | 0.04 | 3.65 | -0.08 | 4.18 |
| $d_{shell}$ (nm)[b] | - | | 2.5 | | 4.5 | |
| $N_{model}$ (/AuNP)[b] | - | | 260 | | 470 | |
| $x$ (%) | - | | 52 | | 61 | |

[a] $r_{core}$ and $PD_{AuNPs}$ for AuNPs/PEG complexes (shown in brackets) were constrained to the average values determined from model fitting of AuNPs in 0% and 100% $D_2O$.
[b] A common set of parameters for $d_{shell}$ and $N_{model}$ were used in the model fitting of SANS curves obtained in 0% and 100% $D_2O$ for the same combination of AuNPs/PEG complexes.

First, SANS curves for $AuNPs_{30}$ in 0% $D_2O$ and 100% $D_2O$ were well-fitted over the whole experimental $q$-range using a solid sphere model with $r$ = 14.1 and 14.6 nm and $PD_{AuNPs}$ = 0.07 and 0.09, respectively. For an ideal solid sphere, the ratio of its $R_g$ and $r$ ($R_g/r$) is equal to $(3/5)^{0.5}$ = 0.77.[70] The experimental value for $R_g/r$ was relatively close to this value, being 0.83 and 0.86 for 0% $D_2O$ and 100% $D_2O$, respectively. This justifies the theoretical description of AuNPs using a solid sphere model. Thus, the average value of $r$ (14.4 nm) and PD (0.08) was used describe the core of the $AuNPs_{30}$/HS–$PEG_{9k}$–OMe and $AuNPs_{30}$/$c$-$PEG_{10k}$ complexes. Next, an analysis of the AuNPs/PEG complexes was conducted using a core–shell double sphere model. Since the solvent isotope composition was assumed to have no influence on the complex structure, the shell thickness ($d_{thickness}$) and number of adsorbed PEG molecules ($N_{model}$) were constrained between data sets obtained in 0% and 100% $D_2O$, for the same combination of AuNPs/PEG. Despite the use of a relatively simple model, the experimental curves were adequately fitted over the whole experimental $q$-range, apart from the SANS curves obtained in 70% $D_2O$, where fitting was omitted due to ambiguous results arising from the significantly smeared data. When the $d_{thickness}$ were compared, $AuNPs_{30}$/HS–$PEG_{9k}$–OMe (4.5 nm) was found to display a significantly larger value compared to that of $AuNPs_{30}$/$c$-$PEG_{10k}$ (2.5 nm). Furthermore, $N_{model}$ were 470 and 260 for HS–$PEG_{9k}$–OMe and $c$-$PEG_{10k}$, respectively. These values were in close coincidence with $N_{Guinier}$ obtained independently from Guinier analysis of SANS curves in 70% $D_2O$ (HS–$PEG_{9k}$–OMe, 540; $c$-$PEG_{10k}$, 290), supporting their validity. Interestingly, the solvent content of shell ($x$), which can be expected to relate with the hydration state of PEG molecules, was found to differ between HS–$PEG_{9k}$–OMe (61%) and $c$-$PEG_{10k}$ (52%). The lower $x$ of $c$-PEG may reflect the reduced hydration states of the adsorbed $c$-PEG molecules, arising from its enhanced interaction with the nanoparticle surface.

## 4.4. CONCLUSIONS

SAXS and SANS were employed to conduct a structural investigation of *c*-PEG and AuNPs/PEG complexes in solution. The ring-closure approach with the modified Williamson-ether synthesis allowed for the synthesis of *c*-PEG without any chemical inhomogeneity in the backbone, and the direct comparison of linear and cyclic topology of corresponding molecular weight. A combined SEC and LCCC fractionation purification procedure produced *c*-PEGs of various molecular weights, all with over 99.3% purity. Solution SAXS measurements and subsequent analysis revealed for the first time, structural information ($<S^2>^{1/2}$, $g_s$, and $\nu$) for a set of corresponding linear and cyclic PEGs in two types of solvents, benzene and water. Whilst qualitatively having a smaller $<S^2>^{1/2}$ compared to *l*-PEGs, *c*-PEGs were found to have suppressed changes in $<S^2>^{1/2}$ and $\nu$ in relation to changes in the solvent quality, leading to differing $g_s$ between benzene and water. The indication of a topological excluded-volume effect, which was suggested to be the cause of this discrepancy, was further supported by a quantitative analysis of the $P(q)$ using a KP worm-like chain and worm-like ring model. The significantly increased $\lambda^{-1}$ of *c*-PEG compared to *l*-PEG along with its apparent solvent independency, indicated a prominent contribution from an excluded-volume effect originating from its cyclic topology.

Based on the understanding of chain dimensions of isolated *c*-PEG chains in solution, physisorbed complex of AuNPs/*c*-PEG, along with chemisorbed AuNPs/HS–PEG–OMe was subsequently characterized by SANS. Upon model-fitting analyses of the SANS curves, it was revealed that $AuNPs_{30}$/*c*-$PEG_{10k}$ and $AuNPs_{30}$/HS–$PEG_{9k}$–OMe possess PEG shell thicknesses ($d_{shell}$) of 2.5 and 4.5 nm, respectively. The adsorbed number of molecules determined from SANS of around 260 molecules depicted a relatively thin, sparsely adsorbed *c*-PEG layer on the surface of AuNPs. Surprisingly, the strong colloidal stabilization of AuNPs was found to be achieved via a highly efficient shielding of the nanoparticle surface with a relatively small

number of *c*-PEG molecules, compared to terminally chemisorbed HS–PEG–OMe. This is highly advantageous in applications where nanoparticle surface plays an imperative role in their functions, such as catalytic nanoparticles.[53] Along with its non-chemical specific mode of adsorption, the present results suggests the implementation of *c*-PEG as a versatile PEGylation agent for the surface functionalization of nanoparticles of diverse chemical compositions.

## 4.5. REFERENCES

(1) *Topological Polymer Chemistry: Progress of Cyclic Polymers in Syntheses, Properties and Functions*; World Scientific, 2013.

(2) Haque, F. M.; Grayson, S. M. The synthesis, properties and potential applications of cyclic polymers. *Nat. Chem.* **2020**, 433-444. DOI: 10.1038/s41557-020-0440-5.

(3) Romio, M.; Trachsel, L.; Morgese, G.; Ramakrishna, S.; Spencer, N.; Benetti, E. Topological Polymer Chemistry Enters Materials Science: Expanding the Applicability of Cyclic Polymers. *ACS Macro Lett.* **2020**, *9* (7), 1024-1033. DOI: 10.1021/acsmacrolett.0c00358.

(4) Chen, C.; Weil, T. Cyclic polymers: synthesis, characteristics, and emerging applications. *Nanoscale Horizons* **2022**, *7* (10), 1121-1135. DOI: 10.1039/d2nh00242f.

(5) Kruteva, M.; Allgaier, J.; Richter, D. Topology Matters: Conformation and Microscopic Dynamics of Ring Polymers. *Macromolecules* **2023**, *56* (18), 7203-7229. DOI: 10.1021/acs.macromol.3c00560.

(6) Arrighi, V.; Higgins, J. Local Effects of Ring Topology Observed in Polymer Conformation and Dynamics by Neutron Scattering-A Review. *Polymers* **2020**, *12* (9). DOI: 10.3390/polym12091884.

(7) Hadziioannou, G.; Cotts, P.; Tenbrinke, G.; Han, C.; Lutz, P.; Strazielle, C.; Rempp, P.; Kovacs, A. Thermodynamic and Hydrodynamic Properties of Dilute-solutions of Cyclic and Linear Polystyrenes. *Macromolecules* **1987**, *20* (3), 493-497.

(8) Dodgson, K.; Bannister, D.; Semlyen, J. Studies of Cyclic and Linear Poly(Dimethyl Siloxanes) .4. Bulk Viscosities. *Polym.* **1980**, *21* (6), 663-667.

(9) Gao, L. F.; Oh, J.; Tu, Y. F.; Chang, T.; Li, C. Y. Glass transition temperature of cyclic polystyrene and the linear counterpart contamination effect. *Polym.* **2019**, *170*, 198-203. DOI: 10.1016/j.polymer.2019.03.018.

(10) Dimarzio, E.; Guttman, C. The Glass Temperature of Polymer Rings. *Macromolecules* **1987**, *20* (6), 1403-1407.

(11) Laurent, B. A.; Grayson, S. M. An efficient route to well-defined macrocyclic polymers via "Click" cyclization. *J. Am. Chem. Soc.* **2006**, *128* (13), 4238-4239. DOI: 10.1021/ja0585836.

(12) Gao, L.; Oh, J.; Tu, Y.; Chang, T. Preparation of low molecular weight cyclic polystyrenes with high purity via liquid chromatography at the critical condition. *Polym.* **2018**, *135*, 279-284. DOI: 10.1016/j.polymer.2017.12.020.

(13) Takano, A.; Kushida, Y.; Aoki, K.; Masuoka, K.; Hayashida, K.; Cho, D.; Kawaguchi, D.; Matsushita, Y. HPLC Characterization of Cyclization Reaction Product Obtained by End-to-End Ring Closure Reaction of a Telechelic Polystyrene. *Macromolecules* **2007**, *40*, 679-681.

(14) Takano, A.; Ohta, Y.; Masuoka, K.; Matsubara, K.; Nakano, T.; Hieno, A.; Itakura, M.; Takahashi, K.; Kinugasa, S.; Kawaguchi, D.; et al. Radii of Gyration of Ring-Shaped Polystyrenes with High Purity in Dilute Solutions. *Macromolecules* **2012**, *45* (1), 369-373. DOI: 10.1021/ma202031w.

(15) Doi, Y.; Matsubara, K.; Ohta, Y.; Nakano, T.; Kawaguchi, D.; Takahashi, Y.; Takano, A.; Matsushita, Y. Melt Rheology of Ring Polystyrenes with Ultrahigh Purity. *Macromolecules* **2015**, *48* (9), 3140-3147. DOI: 10.1021/acs.macromol.5b00076.

(16) D'Souza, A. A.; Shegokar, R. Polyethylene glycol (PEG): a versatile polymer for pharmaceutical applications. *Expert Opin. Drug Deliv.* **2016**, *13* (9), 1257-1275. DOI: 10.1080/17425247.2016.1182485.

(17) Cooke, J.; Viras, K.; Yu, G.-E.; Sun, T.; Yonemitsu, T.; Ryan, A. J.; Price, C.; Booth, C. Large cyclic poly(oxyethylene)s: Chain folding in the crystalline state studied by Raman spectroscopy, X-ray scattering, and differential scanning calorimetry. *Macromolecules* **1998**, *31* (9), 3030-3039. DOI: 10.1021/ma9717909.

(18) Nam, S.; Leisen, J.; Breedveld, V.; Beckham, H. W. Melt Dynamics of Blended Poly(oxyethylene) Chains and Rings. *Macromolecules* **2009**, *42* (8), 3121-3128. DOI: 10.1021/ma802294j.

(19) Brás, A.; Pasquino, R.; Koukoulas, T.; Tsolou, G.; Holderer, O.; Radulescu, A.; Allgaier, J.; Mavrantzas, V.; Pyckhout-Hintzen, W.; Wischnewski, A.; et al. Structure and dynamics of polymer rings by neutron scattering: breakdown of the Rouse model. *Soft Matt.* **2011**, *7* (23), 11169-11176. DOI: 10.1039/c1sm06257c.

(20) Nam, S.; Leisen, J.; Breedveld, V.; Beckham, H. Dynamics of unentangled cyclic and linear poly(oxyethylene) melts. *Polym.* **2008**, *49* (25), 5467-5473. DOI: 10.1016/j.polymer.2008.10.007.

(21) Tsalikis, D.; Alexiou, T.; Alatas, P.; Mavrantzas, V. Conformation and Diffusivity of Ring and Linear Polyethylene Oxide in Aqueous Solution: Molecular Topology Dependent Concentration Effects and Comparison with Experimental Data. *Macromol. Theory Simul.* **2020**, *29* (4). DOI: 10.1002/mats.202000016.

(22) Griffiths, P. C.; Stilbs, P.; Yu, G. E.; Booth, C. Role of Molecular Architecture in Polymer Diffusion - A PGSE-NMR Study of Linear and Cyclic Poly(Ethylene Oxide). *J. Phys. Chem.* **1995**, *99* (45), 16752-16756, DOI: 10.1021/j100045a041.

(23) Watanabe, T.; Chimura, S.; Wang, Y. B.; Ono, T.; Isono, T.; Tajima, K.; Satoh, T.; Sato, S.; Ida, D.; Yamamoto, T. Cyclization of PEG and Pluronic Surfactants and the Effects of the Topology on Their Interfacial Activity. *Langmuir* **2021**, *37* (23), 6974-6984. DOI: 10.1021/acs.langmuir.1c00513.

(24) Wang, Y.; Quinsaat, J. E. Q.; Ono, T.; Maeki, M.; Tokeshi, M.; Isono, T.; Tajima, K.; Satoh, T.; Sato, S.; Miura, Y.; et al. Enhanced dispersion stability of gold nanoparticles by the physisorption of cyclic poly(ethylene glycol). *Nat. Commun.* **2020**, *11*, 6089.

(25) Oziri, O. J.; Wang, Y. B.; Watanabe, T.; Uno, S.; Maeki, M.; Tokeshi, M.; Isono, T.; Tajima,

K.; Satoh, T.; Sato, S. I.; et al. PEGylation of silver nanoparticles by physisorption of cyclic poly(ethylene glycol) for enhanced dispersion stability, antimicrobial activity, and cytotoxicity. *Nanoscale Adv.* **2022**, *4* (2), 532-545. DOI: 10.1039/d1na00720c.

(26) Wang, Y.; Quinsaat, J. E. Q.; Li, F.; Isono, T.; Tajima, K.; Satoh, T.; Sato, S.; Yamamoto, T. Size Control and Enhanced Stability of Silver Nanoparticles by Cyclic Poly(ethylene glycol). *Polymers* **2022**, *14* (21). DOI: 10.3390/polym14214535.

(27) Aboudzadeh, M.; Iturrospe, A.; Arbe, A.; Grzelczak, M.; Barroso-Bujans, F. Cyclic Polyethylene Glycol as Nanoparticle Surface Ligand. *ACS Macro Lett.* **2020**, *9* (11), 1604-1610. DOI: 10.1021/acsmacrolett.0c00730.

(28) Kunkel, G.; Zhou, Q.; Treacy, J.; Montgomery, H.; Salas-Ambrosio, P.; Ready, A.; Spokoyny, A.; Houk, K.; Maynard, H. Comparison of Cyclic and Linear PEG Conjugates. *Bioconjug. Chem.* **2024**, *35* (6), 744-749. DOI: 10.1021/acs.bioconjchem.4c00202.

(29) Hollamby, M. J. Practical applications of small-angle neutron scattering. *Phys. Chem. Chem. Phys.* **2013**, *15*, 10566-10579, Article. DOI: 10.1039/c3cp50293g.

(30) Liu, D.; Song, K.; Chen, W.; Chen, J.; Sun, G.; Li, L. Review: Current progresses of small-angle neutron scattering on soft-matters investigation. *Nucl. Anal.* **2002**, *1*, 100011.

(31) Zucchetti, E.; Zangoli, M.; Bargigia, I.; Bossio, C.; Di Maria, F.; Barbarella, G.; D'Andrea, C.; Lanzani, G.; Antognazza, M. R. Poly(3-hexylthiophene) nanoparticles for biophotonics: study of the mutual interaction with living cells. *J. Mater. Chem. B* **2017**, *5* (3), 565-574. DOI: 10.1039/c6tb02047j.

(32) Cotton, J. Small-angle neutron scattering: Introduction and variations on contrast. *J. Phys. IV* **1999**, *9* (P1), 21-49.

(33) Manet, S.; Lecchi, A.; Impéror-Clerc, M.; Zholobenko, V.; Durand, D.; Oliveira, C. L. P.; Pedersen, J. S.; Grillo, I.; Meneau, F.; Rochas, C. Structure of Micelles of a Nonionic Block Copolymer Determined by SANS and SAXS. *J. Phys. Chem. B* **2011**, *115*, 11318-11329,

Article. DOI: 10.1021/jp200212g.

(34) Grillo, I.; Morfin, I.; Prévost, S. Structural Characterization of Pluronic Micelles Swollen with Perfume Molecules. *Langmuir* **2018**, *34*, 13395-13408, Article. DOI: 10.1021/acs.langmuir.8b03050.

(35) Cosgrove, T.; Heath, T. G.; Ryan, K. Terminally Attached Polystyrene Chains on Modified Silicas. *Langmuir* **1994**, *10*, 3500-3506, Article.

(36) Oberdisse, J. Adsorption and grafting on colloidal interfaces studied by scattering techniques. *Curr. Opin. Colloid Interface Sci.* **2007**, *12*, 3-8, Review. DOI: 10.1016/j.cocis.2006.11.001.

(37) Cosgrove, T.; Ryan, K. NMR and Neutron-scattering Studies on Poly(Ethylene Oxide) Terminally Attached at the Polystyrene Water Interface. *Langmuir* **1990**, *6*, 136-142. DOI: 10.1021/la00091a021

(38) Hone, J. H. E.; Cosgrove, T.; Saphiannikova, M.; Obey, T. M.; Marshall, J. C.; Crowley, T. L. Structure of physically adsorbed polymer layers measured by small-angle neutron scattering using contrast variation methods. *Langmuir* **2002**, *18*, 855-864, Article. DOI: 10.1021/la010709z.

(39) Nelson, A.; Cosgrove, T. Small-angle neutron scattering study of adsorbed pluronic tri-block copolymers on laponite. *Langmuir* **2005**, *21*, 9176-9182, Article. DOI: 10.1021/la050680p.

(40) Hore, M. J. A.; Ye, X.; Ford, J.; Gao, Y.; Fei, J.; Wu, Q.; Rowan, S. J.; Composto, R. J.; Murray, C. B.; Hammouda, B. Probing the Structure, Composition, and Spatial Distribution of Ligands on Gold Nanorods. *Nano Lett.* **2015**, *15*, 5730-5738, Article. DOI: 10.1021/acs.nanolett.5b03088.

(41) Diroll, B. T.; Weigandt, K. M.; Jishkariani, D.; Cargnello, M.; Murphy, R. J.; Hough, L. A.; Murray, C. B.; Donnio, B. Quantifying "Softness" of Organic Coatings on Gold

Nanoparticles Using Correlated Small-Angle X-ray and Neutron Scattering. *Nano Lett.* **2015**, *15*, 8008-8012, DOI: 10.1021/acs.nanolett.5b04011.

(42) Maccarini, M.; Briganti, G.; Rucareanu, S.; Lui, X.-D.; Sinibaldi, R.; Sztucki, M.; Lennox, R. B. Characterization of Poly(ethylene oxide)-Capped Gold Nanoparticles in Water by Means of Transmission Electron Microscopy, Thermogravimetric Analysis, Mass Density, and Small Angle Scattering. *J. Phys. Chem. C* **2010**, *114*, 6937-6943, DOI: 10.1021/jp9118088.

(43) Tang, Q.; Wu, Y.; Sun, P.; Chen, Y.; Zhang, K. Powerful Ring-Closure Method for Preparing Varied Cyclic Polymers. *Macromolecules* **2014**, *47* (12), 3775-3781. DOI: 10.1021/ma500799w.

(44) Xie, F.; Li, Z.; Li, Z.; Li, D.; Gao, Y.; Wang, B. Absolute intensity calibration and application at BSRF SAXS station. *Nucl. Instrum. Methods Phys. Res.* **2018**, *900*, 64-68. DOI: 10.1016/j.nima.2018.05.026.

(45) Takata, S.-i.; Suzuki, J.-i.; Shinohara, T.; Oku, T.; Tominaga, T.; Ohishi, K.; Iwase, H.; Nakatani, T.; Inamura, Y.; Ito, T.; et al. The Design and q Resolution of the Small and Wide Angle Neutron Scattering Instrument (TAIKAN) in J-PARC. *JPS Conf. Proc.* **2015**, *8* (036020). DOI: 10.7566/JPSCP.8.036020.

(46) Okabe, S.; Karino, T.; Nagao, M.; Watanabe, S.; Shibayama, M. Current status of the 32m small-angle neutron scattering instrument, SANS-U. *Nucl. Instrum. Methods Phys. Res. A* **2007**, *572*, 853-858. DOI: 10.1016/j.nima.2006.12.002.

(47) Zhang, F.; Ilavsky, J.; Long, G. G.; Quintana, J. P. G.; Allen, A. J.; Jemian, P. R. Glassy Carbon as an Absolute Intensity Calibration Standard for Small-Angle Scattering. *Metall. Mater. Trans. A* **2010**, *41A*, 1151-1158. DOI: 10.1007/s11661-009-9950-x.

(48) Guinier, A.; Fournet, G. *Small-Angle Scattering of X-Rays*; John Wiley and Sons, 1955.

(49) NIST. *NIST database*. 2009. http://www.ncnr.nist.gov/resources/n-lengths/ (accessed.2024 October 14th)

(50) Ryoki, A.; Watanabe, F.; Okudaira, T.; Takahashi, S.; Oku, T.; Hiroi, K.; Motokawa, R.; Nakamura, Y. Contrast dependence of scattering profiles for poly(ethylene glycol) in water: Investigation by small-angle neutron scattering with <SUP>3</SUP>He spin filter and small-angle x-ray scattering. *J. Chem. Phys.* **2024**, *160*. DOI: 10.1063/5.0192680.

(51) Kotlarchyk, M.; Stephens, R.; Huang, J. Study of Schultz Distribution to Model Polydispersity of Microemulsion Droplets. *J. Phys. Chem.* **1988**, *92*, 1533-1538.

(52) Baumgaertel, A.; Altuntas, E.; Schubert, U. Recent developments in the detailed characterization of polymers by multidimensional chromatography. *J. Chromatogr. A* **2012**, *1240*, 1-20. DOI: 10.1016/j.chroma.2012.03.038.

(53) Malik, M.; Ahmed, H.; Trathnigg, B. Liquid chromatography under critical conditions: Practical applications in the analysis of amphiphilic polymers. *Anal. Bioanal. Chem.* **2009**, *393* (6-7), 1797-1804. DOI: 10.1007/s00216-008-2590-y.

(54) Malik, M. Critical parameters of liquid chromatography at critical conditions in context of poloxamers: Pore diameter, mobile phase composition, temperature and gradients. *J.Chromatogr. A* **2020**, *1609*. DOI: 10.1016/j.chroma.2019.460440.

(55) Lee, H.; Lee, H.; Lee, W.; Chang, T.; Roovers, J. Fractionation of cyclic polystyrene from linear precursor by HPLC at the chromatographic critical condition. *Macromolecules* **2000**, *33* (22), 8119-8121. DOI: 10.1021/ma000807b.

(56) Dinç, C.; Kibarer, G.; Güner, A. Solubility Profiles of Poly(ethylene glycol)/Solvent Systems. II. Comparison of Thermodynamic Parameters from Viscosity Measurements. *J. Appl. Polym. Sci.* **2010**, *117* (2), 1100-1119. DOI: 10.1002/app.31829.

(57) *Polymer Handbook*; Wiley-Interscience, 2003.

(58) Zimm, B.; Stockmayer, W. The Dimensions of Chain Molecules Containing Branches and Rings. *J. Chem. Phys.* **1949**, *17* (12), 1301-1314.

(59) Yamakawa, H. *Modern Theory of Polymer Solutions*; Harper and Row, 1971.

(60) Gartner, T.; Haque, F.; Gomi, A.; Grayson, S.; Hore, M.; Jayaraman, A. Scaling Exponent and Effective Interactions in Linear and Cyclic Polymer Solutions: Theory, Simulations, and Experiments. *Macromolecules* **2019**, *52* (12), 4579-4589. DOI: 10.1021/acs.macromol.9b00600.

(61) Yoshizaki, T.; Yamakawa, H. Scattering Functions of Wormlike and Helical Wormlike Chains. *Macromolecules* **1980**, *13* (6), 1518-1525.

(62) Tsubouchi, R.; Ida, D.; Yoshizaki, T.; Yamakawa, H. Scattering Function of Wormlike Rings. *Macromolecules* **2014**, *47* (4), 1449-1454. DOI: 10.1021/ma402572k.

(63) Burchard, W.; Kajiwara, K. Statistics of Stiff Chain Molecules .1. Particle Scattering Factor. *Proc. R. Soc. Lond. A* **1970**, *316* (1525), 185-.

(64) Nagasaka, K.; Yoshizaki, T.; Shimada, J.; Yamakawa, H. More on the Scattering Function of Helical Wormlike Chains. *Macromolecules* **1991**, *24* (4), 924-931.

(65) Kawaguchi, S.; Imai, G.; Suzuki, J.; Miyahara, A.; Kitano, T. Aqueous solution properties of oligo- and poly(ethylene oxide) by static light scattering and intrinsic viscosity. *Polym.* **1997**, *38*, 2885-2891.

(66) Kawaguchi, S. 痛くない高分子：その優しさはどこから？水中における PEG のコンフォメーション. *Kobunshi* **2016**, *65*, 292.

(67) Hiromi, Y. *Helical Wormlike Chains in Polymer Solutions, 2nd edition*; Springer Berlin, Heidelberg, 2016. DOI: 10.1007/978-3-642-60817-9.

(68) Hickl, P.; Ballauff, M.; Scherf, U.; Mullen, K.; Linder, P. Characterization of a ladder polymer by small-angle X-ray and neutron scattering. *Macromolecules* **1997**, *30* (2), 273-279.

(69) The Merck Index - An Encyclopedia of Chemicals, Drugs, and Biologicals. O'Neil, M. J. Ed.; Royal Society of Chemistry, 2013; p 532.

(70) Jeffries, C.; Ilavsky, J.; Martel, A.; Hinrichs, S.; Meyer, A.; Pedersen, J.; Sokolova, A.; Svergun, D. Small-angle X-ray and neutron scattering. *Nat. Rev. Methods Primers* **2021**, *1*.

DOI: 10.1038/s43586-021-00064-9.

## 4.6. SUPPORTING FIGURES AND TABLES

**Table S4-1**. Density and SLD of $H_2O$, $D_2O$, gold, and PEG

| Material | Density (g $cm^{-3}$) | SLD ($\rho$) (× $10^{10}$ $cm^{-2}$) |
|---|---|---|
| **$H_2O$** | 0.997 | –0.56 |
| **$D_2O$** | 1.10 | 6.39 |
| **gold (AuNPs)** | 19.3 | 4.66 |
| **PEG, $(CH_2CH_2O)_n$** | -[a] | 0.69[c] |

[a] Partial specific volume of PEG in aqueous solution was used for the calculation of $\rho_{PEG}$.

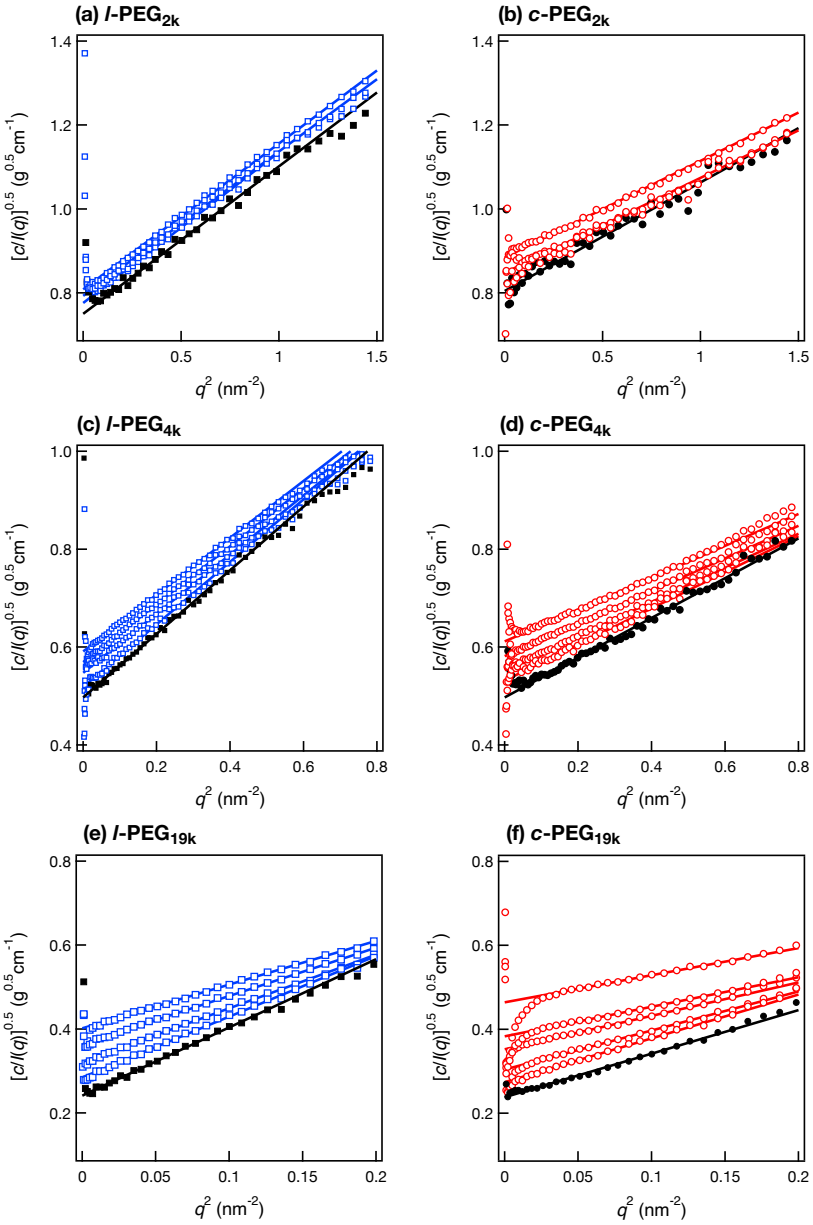


**Figure S4-1**. Berry plots of various *l*-PEG and *c*-PEG taken in benzene at finite concentrations and extrapolated values. Data points of finite concentrations are shown in color, while $c_{PEG} \rightarrow 0$ extrapolated values are shown in black. The concentrations used from top are, for $PEG_{2k}$: $c_{PEG}$ = 5, 2 and 1 wt%, for $PEG_{4k}$: $c_{PEG}$ = 3, 2, 1.5 and 1 wt%, for $PEG_{19k}$: $c_{PEG}$ = 3, 2, 1.5, 1 and 0.5 wt%, respectively.

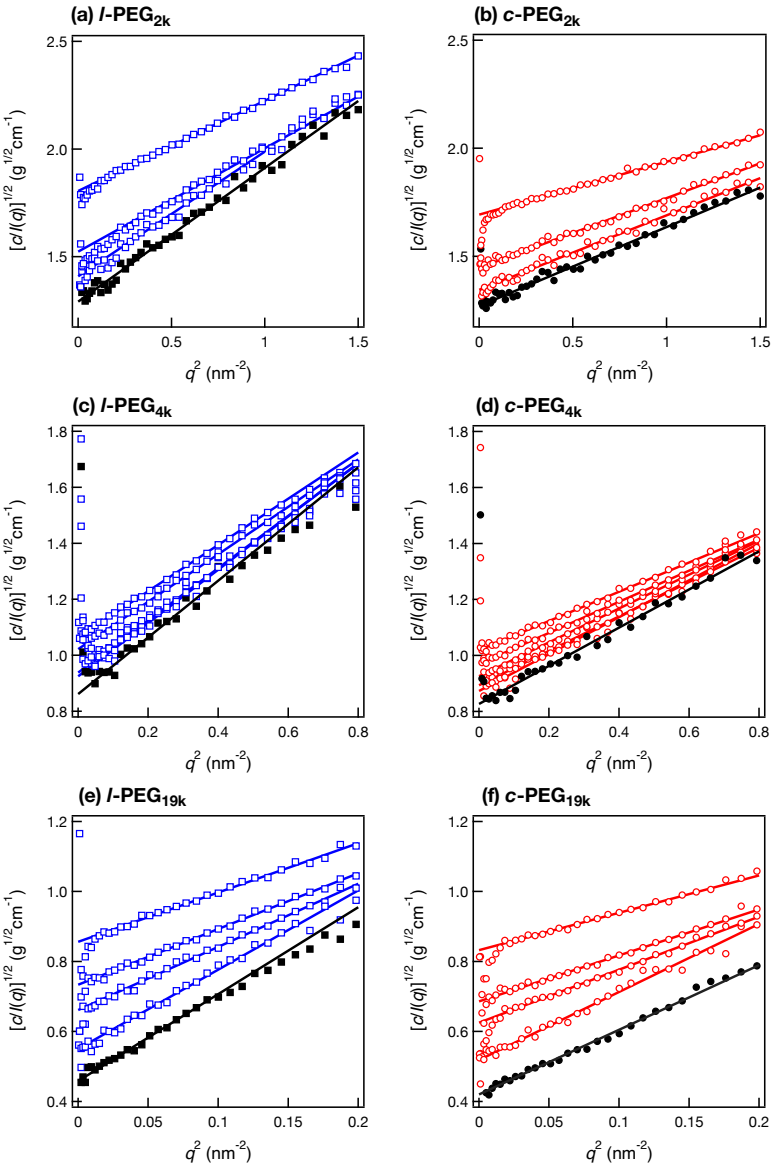


**Figure S4-2**. Berry plots of various *l*-PEG and *c*-PEG taken in water at finite concentrations and extrapolated values. Data points of finite concentrations are shown in color, while $c_{PEG} \rightarrow 0$ extrapolated values are shown in black. The concentrations used from top are, for $PEG_{2k}$: $c_{PEG}$ = 5, 2 and 1 wt%, for $PEG_{4k}$: $c_{PEG}$ = 3, 2, 1.5 and 1 wt%, for $PEG_{19k}$: $c_{PEG}$ = 3, 2, 1.5 and 0.5 wt%, respectively.

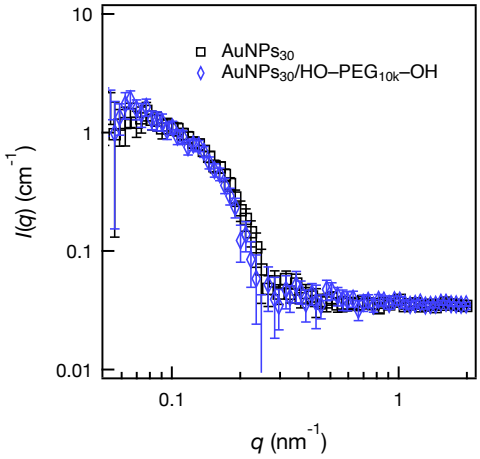


**Figure S4-3**. SANS curves of $AuNPs_{30}$ and $AuNPs_{30}$/*l*-$PEG_{10k}$ in 100% $D_2O$ after the ultrafiltration procedure. Almost identical curves between the two samples indicate no adsorbed PEG layer to be present on AuNPs after ultrafiltration.

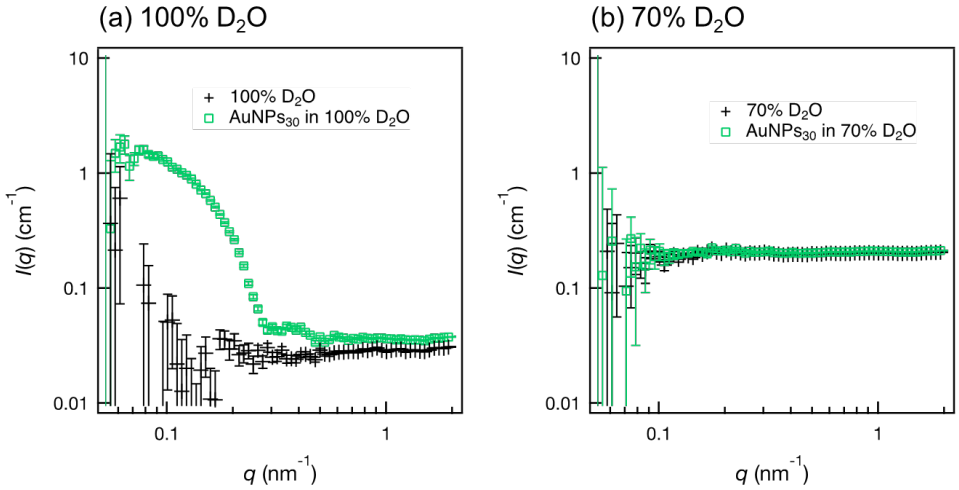


**Figure S4-4**. (a) SANS curves of 100% $D_2O$ as a background and $AuNPs_{30}$ in 100% $D_2O$. (b) SANS curves of 70% $D_2O$, contrast matched to gold, as a background and bare $AuNPs_{30}$ in 70% $D_2O$. Scattering in the low $q$ region observed for $AuNPs_{30}$ in 100% $D_2O$ is nearly completely eliminated in 70% $D_2O$.

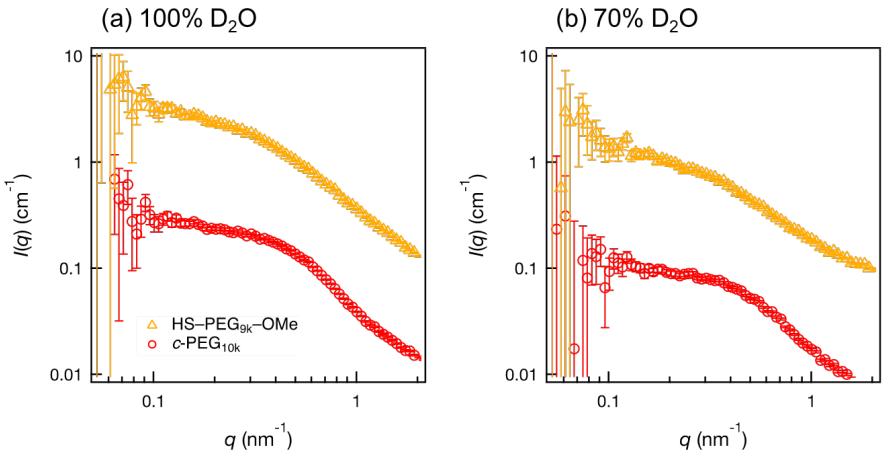


**Figure S4-5.** SANS curves of 10 mg/mL *c*-PEG and HS–PEG–OMe solutions in (a) 100% $D_2O$ and (b) 70% $D_2O$. A plateau is observed in the $q$-range of $q \leq 0.1$–$0.3$ $nm^{-1}$. Scattering for HS–$PEG_{9k}$–OMe is shifted upwards by a factor of ten for clarity.

# *Chapter 5*

## General conclusions

In this thesis, several novel effects of cyclic topology were found at various interfaces for a series of cyclic PEG and Pluronic surfactants, with implications of their potential applications in the design of novel functional materials. The main findings of this thesis are summarized below.

In chapter two, cyclized polymers exhibited enhanced surface activity compared to its corresponding linear species, due to reduced occupational area at the air–water interface. The effect of cyclization was found to be influenced by the PEG ratio and block architecture of the linear polymer, with pronounced effect for surfactants with large PEG ratio and BAB-type block architecture. The topological effect of cyclization was found to differ from the effect of chain-end methylation, indicating the origin of surface activity enhancement to be distinct from simple chemical modification of hydrophilic moieties.

In chapter three, cyclized Pluronic surfactants were found to have lower critical micelle temperatures, with reduced micellization enthalpy and entropy, attributed to the better shielding of hydrophobic PPG blocks by hydrophilic PEG blocks from the surrounding water environment in the unimer state. Difference between linear and cyclic species on their micellization parameters were more pronounced for a surfactant of BAB-type block architecture. Micelle dimensions and its thermal stability was found to be affected from the cyclic topology, with contrasting stabilizing/destabilizing effect depending on block architecture.

In chapter four, small-angle scattering investigation was carried out on the unique structure of cyclic PEG adsorbed gold nanoparticles. First, chain dimensions and conformation of molecularly dissolved cyclic PEG was elucidated through small-angle X-ray scattering, revealing their compact structure. Systematic investigation of molecular-weight and solvent dependency confirmed a strong excluded-volume effect originating from the cyclic topology to be present. Next, small-angle neutron scattering experiments and structural analyses using

model-fitting methods were conducted to quantitatively discuss the adsorbed complex structure. Compared to chemisorbed linear thiol PEGs, cyclic PEGs were found to stabilize the surface of gold nanoparticles with fewer molecules contributing to a relatively thin adsorbed layer, indicating an efficient stabilizing effect to be achieved through non-terminal adsorption.

In conclusion, the findings of this thesis holds implications for a variety of novel properties of cyclic polymers that are yet to be explored. As in the case of cyclic PEG and their potential application towards novel PEGylation agents, the investigation of fundamental properties of cyclic polymers is crucial in their future implementation in the design of novel functional materials.